

國立交通大學

材料科學與工程研究所

博士論文

氧化鈀奈米薄片之成長機制與光電特性之研究

Growth and Photoelectrical Properties of
Reactive Sputtered PdO Nanoflakes

研究生：黃建融

指導教授：潘扶民 教授

中華民國 九十九年 十月

氧化鈮奈米薄片之成長機制與光電特性之研究
**Growth and Photoelectrical Properties of Reactive
Sputtered PdO Nanoflakes**

研究生：黃建融

Student: Chien-Jung Huang

指導教授：潘扶民教授

Advisor: Prof. Fu-Ming Pan

國立交通大學

材料科學與工程學系



Submitted to Department of Materials Science and Engineering

College of Engineering

National Chiao Tung University

in Partial Fulfillment of the Requirements

for the Degree of Doctor of Philosophy

in

Materials Science and Engineering

October 2010

Hsinchu, Taiwan, Republic of China

中華民國九十九年十月

氧化鈮奈米薄片之成長機制與光電特性之研究

學生：黃建融

指導教授：潘扶民

國立交通大學
材料科學與工程學系

摘要

於本論文中，我們利用反應性濺鍍法成長氧化鈮薄膜並且研究期成長機制與光電特性，包含場發射、光感應與光催化反應。當氧化鈮成長於白金基板上時，此氧化鈮具有片狀之形貌。此奈米薄片具有核殼結構，其結構為一層氧化鈮包圍一顆單晶鈮。我們將此被氧化鈮層包圍之奈米薄片的成因歸咎於氧化鈮與白金基材之間晶格不匹配產生之介面壓應力所形成。測試此奈米薄片之場發射特性並發現其場強因子約為791。氧化鈮薄片亦成長於二氧化矽基板上並研究其光感應特性。於室溫下所成長之氧化鈮薄膜亦具有奈米薄片結構並垂直站立於二氧化矽基板上。於400 °C下退火後，此奈米薄片具有單晶結構。於400 °C下退火後之氧化鈮薄膜之能隙坐落於紅光區(約2.06 eV)，並且於紫外光(365 nm)照射下展現極佳之光敏感度。造成此高之光敏感度乃由於此薄膜具有極佳之結晶性，因此減少電子電洞對覆合中心。此外，此薄膜亦具有較低電阻，因此具有較高之載子傳輸效率。於紫外光起始照射時，電流密度有些許下降之趨勢，此為O₂⁻離子吸附於此400 °C退火後之氧化鈮薄片上所造成。

我們亦製備了 PdO/TiO₂ 異質結構以探討其光催化分解亞甲基藍特性。於紫外光-可見光照射下，相較於純 TiO₂ 奈米球，PdO/TiO₂ 異質結構對於亞甲基藍具有兩倍之光觸媒活性。此提高之光觸媒活性乃歸功於此兩半導體氧化物異質接合所形成之位能障。此對於亞甲基藍分解之光觸媒反應機制亦於本文中探討。於可見光照射下，雖然 PdO 仍可被激發，但此 PdO/TiO₂ 異質結構對於亞甲基藍僅有微弱之觸媒活性。我們將其歸因於此異質結構中非平衡之光激發載子的次費米能階不匹配所造成。而表面分解亞甲基藍反應的氧化還原電位不匹配亦是其因素之一。



Growth and Photoelectrical Properties of Reactive Sputtered PdO Nanoflakes

Student: Chien-Jung Huang

Advisors: Prof. Fu-Ming Pan

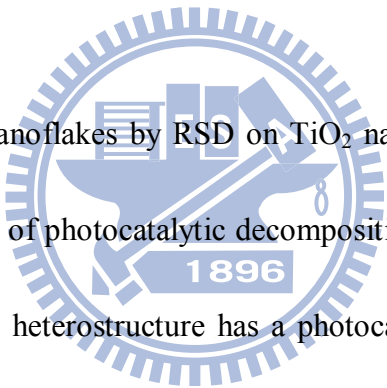
Department of Materials Science and Engineering
National Chiao Tung University

Abstract

In the thesis, we deposited palladium oxide nanoflake thin films by reactive sputter deposition (RSD) and various properties were studied including electron field emission, photoconduction and photocatalysis. The PdO thin film RSD-deposited on the Pt substrate had a flake-like morphology. The nanosized flake had a core-shell structure with a single Pd grain encapsulated by a crystalline PdO surface layer. The formation of the PdO capped nanoflakes was a result of a large interfacial stress built up between PdO and Pt due to lattice mismatch. Field emission characteristics of the nanoflakes were studied and a field enhancement factor of 791 was obtained.

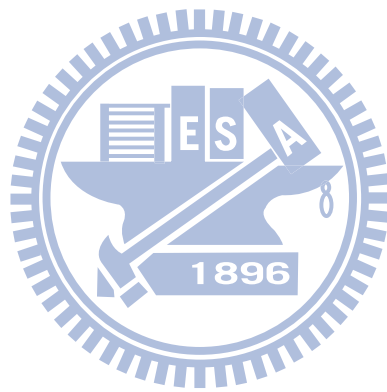
PdO nanoflakes were also deposited on a SiO₂ substrate by reactive sputter deposition and photoconduction characteristics of the thin films were examined. PdO thin films deposited at 25 °C is composed of bowed nanoflakes standing on the SiO₂ substrate, which have a single-crystalline structure after thermal anneal at 400 °C.

The 400 °C-annealed nanoflake thin film has a bandgap energy in the red-light range (~2.06 eV), and exhibits a very sensitive photoresponse upon UV (365 nm) illumination. The high photoresponse sensitivity of the 400 °C-annealed nanoflake thin film is ascribed to a lower density of recombination centers and traps due to an excellent crystallinity and a high carrier extraction efficiency due to a low electrical resistivity. A slight decrease in the photocurrent density during the initial stage of the UV illumination is attributed to adsorption of O₂⁻ anions on the 400°C-annealed nanoflakes.



We deposited PdO nanoflakes by RSD on TiO₂ nanoparticles dispersed on the SiO₂ substrate for the study of photocatalytic decomposition of methylene blue (MB) molecules. The PdO/TiO₂ heterostructure has a photocatalytic activity toward MB decomposition under UV-vis light illumination as large as twice that of bare TiO₂ nanoparticles. The enhancement of the photocatalytic activity is ascribed to the fast photogenerated carrier separation resulting from the potential barrier formed at the heterojunction between the two semiconductor oxides. A photocatalytic reaction mechanism for the MB decomposition is proposed. The PdO/TiO₂ heterostructure exhibits little photocatalytic activity toward the MB decomposition under visible light illumination even though PdO can be photoexcited by visible light. We ascribe the photocatalytic inactivity to the mismatch between quasi-Fermi levels of

nonequilibrium photogenerated carriers in the heterostructure and the redox potential of primary surface reactions leading to the MB decomposition.



Acknowledgements

首先，本文將獻予曾經在我的博士生涯中幫助我、鼓勵我的恩人。而最值得感激的人則是我的指導老師，潘扶民教授。這些年來老師循序漸進與不辭辛苦的指導學生，從專業知識、實驗方法、論文寫作以及口頭報告，無一不細心的教導與鼓勵。現在回想起老師的諄諄教誨，當時老師的教誨的確是使得學生不斷的進步與成長的原動力。此外，很感謝老師給予學生出國參加研討會的機會。藉此機會，練習英文會話能力也了解到英文的重要性，未來學生會更加充實英文能力。

這五年我在實驗室認識了許多好夥伴，掐指一算，應該有 20 位以上吧。志豪、泰銓、冠榮、子中、秀瑛、逸群、心怡、振洋、重守、博翔、東原、昱儒、世昌等等，與你們處在一塊兒，實驗室變得很歡樂，似乎做實驗的辛苦也一一的被你們歡樂的氣氛給中和了，一點都不覺得累。畢業的學長及學弟妹們，謝謝你們以往的陪伴，而還在實驗室奮鬥的夥伴們，也祝福你們能夠一一順利畢業。另外，我還認識了幾個好朋友，尉霖、韋達這兩個 TEM 高手，從他們身上我獲得了很多知識，也很感謝你們在我需要的時候大力相挺、幫助我，使我的數據順利產出。也很感謝你們陪我上山下海騎鐵馬四處跑，藉此調劑身心。而修誠亦在我的生活中添加了不少色彩，憨憨呆呆的樣子，成為了大家的笑果，希望你也能快快順利畢業。還有我的大學朋友們，也很謝謝你們的陪伴與鼓勵，希望你們一切都順心如意。這些年來，還有一位可愛的小天使，總在我沮喪、失志的時候聽

我傾訴苦水。活潑開朗的妳，總是能使我恢復元氣，帶給我歡樂。謝謝妳一路的鼓勵與扶持，認識妳真好。

最後我要感謝我的家人，爺爺、奶奶、爸媽、老妹、老弟，謝謝你們給我一個很溫暖的家。感謝你們這段日子一直支持我、鼓勵我。這段路有你們陪伴，讓我不害怕，勇往直前的奔向終點。離開11年了，總是聚少離多，現在總算可以回家了。還有姑丈、姑媽、表弟們，謝謝你們常打電話來關心。

謝謝大家的支持使我順利完成學位，在此祝福每一個人都能順心、快樂。



Contents

摘要	I
Abstract.....	III
Acknowledgements	VI
Contents.....	VIII
Figure Caption.....	XI
Chapter 1 Introduction.....	1
1.1 Introduction to nanomaterials.....	1
1.2 Motivation	3
Chapter 2 Literature Review.....	5
2.1 Material properties of palladium oxide.....	5
2.2 Growth methods of Palladium Oxide.....	7
2.2.1 Deposition of PdO thin films by sputtering.....	7
2.2.2 Formation of PdO nanoparticles by thermal oxidation	8
2.2.3 Formation of PdO tips array by thermal oxidation	10
2.2.4 Synthesis of PdO nanofibers by electrospinning	12
2.3 Field Emission Theory	13
2.3.1 Field emission of PdO nanostructures.....	17
2.4 Photocurrent generation in metal oxide	18
2.5 Photoresponse of PdO	23
2.6 Photoexcitation and photocatalytic reaction process of semiconductors.....	25
2.7 Enhanced Photoactivity of TiO ₂ by Heterostructure	27
2.8 Enhanced Photoactivity of TiO ₂ by PdO.....	31
2.9 Enhanced Photoactivity of SnO ₂ by PdO	32
Chapter 3 Experimental methods.....	35

3.1 Experimental flowchart.....	35
3.1.1 Preparation of PdO nanoflakes.....	36
3.1.2 Preparation of PdO/TiO ₂ heterostructures.....	37
3.1.3 Characterizations of PdO nanoflakes and PdO/TiO ₂ heterostructures.....	38
3.2 Radio frequency magnetron sputter deposition system.....	38
3.3 Materials Characterizations.....	40
3.3.1 Scanning Electron Microscope (SEM).....	40
3.3.2 Transmission Electron Microscopy (TEM).....	41
3.3.3 X-ray Photoelectron Spectroscopy (XPS).....	41
3.3.4 Auger Electron Spectroscopy (AES).....	42
3.3.5 X-ray diffractometry (XRD).....	42
3.3.6 UV-Vis Absorption Spectroscopy.....	43
3.4 Measurement of PdO nanoflakes photoelectric properties.....	44
3.4.1 Field Emission Measurement.....	44
3.4.2 Photoresponse Measurement.....	44
3.4.3 Photocatalytic Activity Measurement.....	45
Chapter 4 Growth and Field Emission of Reactive Sputtered Pd-PdO Core-shell	
Nanoflakes on Platinum.....	47
4.1 Growth of Pd-PdO core-shell Nanoflakes on Pt substrate.....	47
4.2 Growth and core-shell mechanism of PdO Nanoflakes.....	53
4.3 Field Emission Characteristics of PdO Nanoflakes.....	58
4.4 Summary.....	61
Chapter 5 Growth and Photoresponse Study of PdO Nanoflakes Reactive-sputter	
Deposited on SiO ₂	62
5.1 Growth of PdO Nanoflakes on SiO ₂ substrate.....	62
5.2 Bandgap Energy of PdO nanoflakes.....	70

5.3 Photoresponse of PdO nanoflakes	73
5.4 Effect of oxygen adsorption in photoresponse	76
5.5 Summary	79
Chapter 6 Heterostructure of PdO Nanoflakes and TiO ₂ Nanoparticles in	
Photocatalytic Application.....	80
6.1 Characterization of PdO/TiO ₂ heterostructures.....	80
6.2 Photocatalytic Degradation of Methylene Blue by PdO/TiO ₂ heterostructures..	88
6.3 Charge Transfer Mechanisms in PdO/TiO ₂ heterostructures.....	92
6.4 Photodegradation of MB in PdO/TiO ₂ heterostructures	95
6.5 Summary	102
Chapter 7 Conclusions and Future Works	
7.1 Conclusions	104
7.2 Future works.....	107
Appendix.....	109
References.....	112

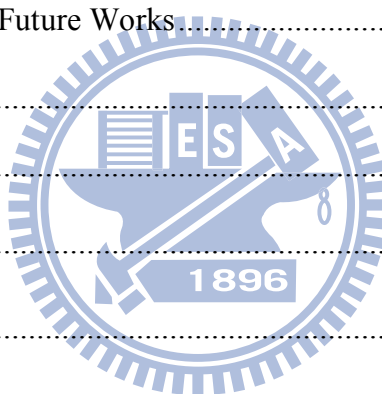


Figure Caption

Figure 2-1 The tetragonal bulk unit cell of PdO. Small dark spheres indicate oxygen atoms, large light ones Pd atoms..... 6

Figure 2-2 SEM images of the sputtered PdOx thin films annealed at (a) 700 °C and (b) 1000 °C for 1 min under N₂ gas flow. (c) Normalized transmitted light intensity at wavelengths of 405 and 635 nm for PdOx thin film with a thickness of 15 nm fabricated on SiO₂ substrate..... 8

Figure 2-3 The Pd/SiO₂ catalysts after oxidation at 350 °C in 1 bar O₂ for 1 h (a), (b) corresponding SAED pattern. 10

Figure 2-4 The Pd/SiO₂ catalyst after oxidation in 1 bar O₂ at 400 °C for 1 h (a), (b) corresponding SAED pattern. 10

Figure 2-5 AFM image of a Pd film annealed in oxygen at 900 °C..... 12

Figure 2-6 SEM images of (a) Pdac/PC fibers with 30 wt.% of palladium acetate; (b) Pdac/PC fibers with 70 wt.% of palladium acetate; (c, d) Pdac/PC calcined fibers at 550 °C; (e, f) Pdac/PC calcined fibers at 800 °C (Pdac/PC fibers with 70 wt.% of palladium acetate is used for the calcinations under air) 13

Figure 2-7 Potential-energy diagram illustrating the effect of an external electric field on the energy barrier for electrons at a metal surface 15

Figure 2-8 (a) AFM of PdO nanoemitters thermal oxidized at 800 °C. (b) I-V characteristic for different cathodes. The lime with (■) and (▲) are for PdO nanoparticles oxidized at 400 °C and at 800 °C, respectively. The line with marks (*) is the reference curve for a Si cathode. 18

Figure 2-9 schematic of the photoconduction mechanism. (a) Schematic of a NW photoconductor. Upon illumination with a photon energy above E_g. (b) The

schematic of the energy band diagrams of a NW in dark. (c) NW Under UV illumination.....	20
Figure 2-10 I-V curves show dark current (●) and photocurrent (▲) of a single ZnO nanowire under 365 nm, 0.3 mWcm ⁻² UV-light illumination. The inset reveals an FE-SEM image of a 60 nm ZnO nanowire bridging four Au electrodes.	22
Figure 2-11 Reversible switching of a ZnO nanowire between low and high conductivity states when the handheld UV-lamp was turned on and off. The bias on the nanowire is 1 V.....	22
Figure 2-12 FSEM image of the PdO/TiO ₂ film calcined at 350 °C.....	24
Figure 2-13 Photoconductivity of the PdO/TiO ₂ film calcined at various temperatures under visible light in flowing pure N ₂	24
Figure 2-14 Schematic photoexcitation in a solid followed by deexcitation events...	26
Figure 2-15 SEM micrographs of the TiO ₂ film/Cu ₂ O microgrid heterojunction.	29
Figure 2-16 (a) Transmittance spectra of the TiO ₂ film, Cu ₂ O film, and TiO ₂ film/Cu ₂ O microgrid heterojunction. (b) Schematic energy diagram of Cu ₂ O and TiO ₂	30
Figure 2-17 Photocatalytic decomposition of MB by the Cu ₂ O film, TiO ₂ film, and TiO ₂ film/Cu ₂ O microgrid heterojunction under irradiation of UV-vis light.....	30
Figure 2-18 Effect of NO conversion efficiency with initial NO concentration after 1200 min irradiation using P25 and 0.05 wt.% Pd/TiO ₂ . <i>Conditions</i> : 125W Hg-arc, 80 °C, 75% RH, 10 s space time and 21% O ₂ concentration.....	32
Figure 2-19 UV–vis spectra of bare SnO ₂ and PdO/SnO ₂ samples	34
Figure 2-20 Effect of irradiation time (10 mW/cm ²) on the survival ratio of <i>E. coli</i> over SnO ₂ and PdO/SnO ₂ films.	34

Figure 3-1 Experimental flowchart for the fabrications and analyses of the Pd-PdO
coreshell nanoflakes, single-crystalline PdO nanoflakes and PdO/TiO₂
heterostructures. 36

Figure 3-2 Plasma sputtering System..... 40

Figure 3-3 Schematic diagram of the field emission measurement..... 44

Figure 3-4 Schematic diagram of the Photoresponse measurement. 45

Figure 3-5 images of instruments for photocatalytic activity measurement..... 46

Figure 4-1. SEM images of Pd-PdO nanoflakes deposited on the Pt substrate at (a) 25
°C and (b) 200 °C. (c) 60°-tilted SEM image for nanoflakes deposited at 200 °C..... 48

Figure 4-2. XRD spectra of Pd-PdO nanoflakes deposited on the Pt substrate at (a) 25
°C and (b) 200 °C. The inset shows the Pd(3d) XPS spectra of nanoflakes deposited
at (a) 25 °C and (b) 200 °C..... 50

Figure 4-3. (a) TEM image of a Pd-PdO nanoflake separated from the nanoflake thin
film deposited at 200 °C for 15 min. The inset is the SAED pattern of the nanoflake.
Two diffraction sets are identified to correspond to the Pd fcc structure (solid line)
and the PdO tetragonal structure (dashed line). (b) The HRTEM image of the edge
area marked by circle in (a). The inset shows the FFTD pattern of the area marked
by square in (b). 52

Figure 4-4 SEM images of Pd-PdO nanoflakes deposited on the Pt substrate at 25 °C
for (a) 2 min, (b) 3 min, (c) 4 min and (d) 5 min. 54

Figure 4-5 XPS survey spectra for 2 min deposition at a substrate temperature of 25
°C..... 54

Figure 4-6. Field emission J-E curves of Pd-PdO nanoflakes deposited on the Pt substrate at (a) 25 °C and (b) 200 °C. The corresponding F-N plots of the J-E curves (a) and (b) are shown in the inset. 60

Figure 5-1 (a) Plane-view and (b) 60°-tilted SEM images of the as-deposited PdO nanoflake thin film, respectively; (c) Plane-view and (d) 60°-tilted SEM images of the 400°C-annealed nanoflake thin film, respectively. The insets in (b) and (d) are the corresponding enlarged SEM images. 63

Figure 5-2 (a) XPS survey spectra for the as-deposited PdO nanoflake thin film; the peaks denoted by asterisk symbols are due to the ultrathin Pt film for energy calibration; (b) Pd (3d) XPS spectra of the 25°C-deposited, the 200°C-annealed and the 400°C-annealed nanoflake thin films. 64

Figure 5-3 XRD spectra of the PdO thin films: (a) 25°C-deposited nanoflake thin film, (b) 200°C-annealed nanoflake thin film and (c) 400°C-annealed nanoflake thin film. 66

Figure 5-4 (a) BFTEM image of a PdO nanoflake separated from the 400°C-annealed nanoflake thin film and the corresponding SAED pattern (inset); (b) HRTEM image of a top-edge area marked by the circle in (a). 69

Figure 5-5(a) HRTEM image of a selected area on the nanoflake shown in the inset; (b) inverse fast Fourier transform image of a nanograin in the (010) plane. 70

Figure 5-6 (a) Diffusion reflectance spectra of the reactive-sputtered PdO thin films, and (b) Tauc plots constructed from (a); curves a, b and c represent the UV-vis spectra and the Tauc plots of the as-deposited, the 200°C-annealed and the 400°C-annealed nanoflake thin films, respectively. 72

Figure 5-7 Photocurrent density of the PdO thin films under the periodic UV exposure at 365 nm as a function of the photoresponse measurement time: (a) the

200°C-annealed nanoflake thin film and (b) the 400°C-annealed nanoflake thin film. Photoresponse profiles a and b were obtained at a bias of 3 V with the photocurrent measurement configuration shown in the inset..... 74

Figure 5-8 Photocurrent density-time profiles : (a) the 200°C-annealed nanoflake thin film and (b) the 400°C-annealed nanoflake thin film..... 76

Figure 5-9 O 1s XPS spectra of the PdO nanoflake thin film: (a) the as-deposited, (b) the 200°C-annealed and (c) the 400°C-annealed nanoflake thin films. The labeled binding energies of the O 1s electron of various oxygen containing species and the Pd 3p_{3/2} electron are summarized from refs. [9, 73-75]. The XPS spectra were calibrated with the binding energy of the Pt(4f_{7/2}) electron..... 78

Figure 6-1 (a) SEM images of P-25 TiO₂ nanoparticles spun on the SiO₂ substrate; SEM images the PdO/TiO₂ heterostructures prepared with different PdO deposition times: (b) 1 min, (c) 3 min, (d) 4 min, (e) 8 min, and (f) 12 min..... 82

Figure 6-2 XRD spectra of (a) the P-25 sample, and the PdO/TiO₂ heterostructures prepared with different PdO deposition times: (b) 1 min, (c) 3 min, (d) 4 min, (e) 8 min, and (f) 12 min..... 83

Figure 6-3 BFTEM images of the P-25 sample (a), and the PdO/TiO₂ heterostructures prepared with different PdO deposition times: (b) 1 min, (c) 3 min, (d) 4 min, (e) 8 min, and (f) 12 min. The insets in (a)-(f) are the corresponding HRTEM images. . 85

Figure 6-4 HRTEM images of (a) the TiO₂-PdO-1 and (b) the TiO₂-PdO-12 heterostructures..... 86

Figure 6-5 UV–vis diffuse reflection absorption spectra of the as-prepared photocatalysts: (a) the P-25 sample, and the PdO/TiO₂ heterostructures prepared with

different PdO deposition times: (b) 1 min, (c) 3 min, (d) 4 min, (e) 8 min, and (f) 12 min.....	87
Figure 6-6 (a) Absorption spectra of MB solutions as a function of the UV light illumination time in the presence of TiO ₂ -PdO-4; The illumination time dependent normalized concentration of the MB aqueous solution photocatalyzed by the P-25 sample and the PdO/TiO ₂ heterostructures prepared with different PdO deposition times (b) under UV-vis light illumination and (c) under visible light illumination....	91
Figure 6-7 Schematic energy band diagram of the PdO/TiO ₂ heterostructure. Possible reaction paths leading to the photocatalytic MB decomposition are also illustrated. The numbers labeled in the diagram represent accordingly the reaction steps (eqs. 1-9) discussed in the text.....	94
Figure 6-8 C/C ₀ versus irradiation time plots of recycling test on PdO/TiO ₂ heterostructure for MB photodegradation. RSD time of PdO = 4 min.	101
Figure 6-9 (A) C(1s), (B) Pd(3d) and (C) Ti(2p) XPS spectra of the PdO/TiO ₂ photocatalyst: (a) before and (b) after MB photocatalytic degradation.	101
Figure A Cyclic voltammogram of the PdO nanoflake thin film in 0.1 M n-Bu ₄ NClO ₄ with scan rate of 20 mv/s.....	111
Figure B Energy for various semiconductor in aqueous electrolyte at pH= 1.....	111

Chapter 1

Introduction

1.1 Introduction to nanomaterials

In the twenty first century, miniaturizations of devices into micrometer, even nanometer sizes are required while their ultimate performance is significantly improved. This raises many issues regarding nanomaterials (one dimension < 100 nm) for achieving specific demand. Nanomaterials have received steadily growing interests as a result of their particular and exciting properties, and their applications are superior to bulks due to a large surface-to-volume ratio and the quantum-confined electronic structure [1-3]. For example, the electronic states for a nanoscale semiconductor become partially or completely discrete as in atoms and molecules, and the band gap are also widened. When the band gap was widened, it enables a higher concentration of carriers to contribute to the band-edge light emission and leads to a reduced emission threshold, improved temperature stability, and a narrower emission line [4].

Nanoscaled metal oxides represent an assorted and exciting class of materials which properties across the entire range from metals to semiconductors and insulators. Metal oxides such as RuO_2 , ZnO , and TiO_2 present a semiconductor property and their

nanostuctures have been employed to many applications duo to a broad range of electronic, chemical, and physical properties. For example, RuO₂ nanorods exhibiting a high electrical conductivity (~40 μΩ cm) were used as the electron field emission emitters and showed a very stable emission current [5]. ZnO nanowires are good materials for gas sensors due to its large surface to volume ratio. The sensors exhibit high sensitivity and fast response to ethanol [6]. ZnO nanowires also have generated lots of interest for selective UV (λ=375 nm) photodetector applications with a fast response time [7-8]. TiO₂ nanotubes with a single-crystalline structure can provide a fast path for the transportation of phoroexcited carriers and further enhance the external quantum efficiency in solar cells [9].

PdO is a kind of metal oxides and possesses a p-type semiconductor property. Because PdO has various special chemical, optical and electrical properties, it is of great importance in many technological applications, such as catalysis [10-11], photoelectrolysis [12] and electron field emission [13]. It is thermally stable up to ~800 °C, at which the oxide decomposes into the metallic Pd state [14]. Because of the high thermal stability, PdO thin films, of which optical properties change upon laser heating, are proposed to be implemented in a super-resolution near-field structure for the data storage technology [14]. Because conversion from PdO to Pd during the high temperature methane oxidation reaction reveals a high catalyst

activity, PdO is an excellent catalyst for methane and CO oxidation under oxygen-rich conditions [15-17]. Furthermore, PdO has a narrow band gap of 0.8-2.2 eV [14, 18-19], it can assist the wide bandgap materials in visible-light absorption. The PdO-assisted visible-light absorption enhancement is particularly desirable for those applications demanding a large active surface area, such as photocatalysis, gas sensing and microbial inactivation, hence PdO nanostructures have recently been prepared and investigated for their intriguing properties. For instance, PdO nanofibers have been synthesized by electrospinning using palladium acetate/polycarbonate solutions [20], and nanotips were produced by relaxing large compressive stresses during thermal oxidation of Pd films [21]. PdO nanoparticles formed in TiO₂ thermally impregnated with Pd was found to be important for photocatalytic oxidation of NO in gas phase [22]. PdO can also enhance the photoactivity of TiO₂ and SnO₂ toward microbiogenic reactions under visible light irradiation [23-24].

1.2 Motivation

In our lab, we have deposited a PdO thin film by RSD to develop nanogap electrodes for surface-conduction electron-emitter display (SED) [25] due to its low electrical resistivity and high chemical stability. In the development process, we

found the sputtered PdO thin films on Pt substrate have a flake-like nanostructure. The nanosized flakes have a core-shell structure, in which a Pd grain was encapsulated by a crystalline PdO layer, were produced. Unlike the former, PdO nanoflakes have a different crystal structure, which is a single-crystalline nanoflake as grown on the SiO₂ substrate. The interesting phenomenon is worthy to study and discuss in depth. Because the PdO thin films have a nanostructure and a high aspect ratio, its particular photoelectrical properties have been examined in the study, including electron field emission and photoconduction.

PdO was reported as a p-type semiconductor with a small bandgap energy of ~0.8-2.2 eV [14, 18-19]. In the photoconduction experiment, we found that the PdO nanoflakes have a strong absorption maximum at ~620 nm and exhibit a very sensitive photoresponse behavior under UV and visible (UV-vis) light illumination. The formation of the p-n junction between the PdO nanoflake and the TiO₂ nanoparticle is expected to enhance the photocatalytic activity of TiO₂ because the built-in field at the heterojunction can effectively separate photogenerated electrons and holes, and thus increase the lifetime of e-h pairs. In the thesis, we prepared PdO nanoflakes by RSD to form a heterostructure with TiO₂ nanoparticle and study the photocatalytic activity of the PdO/TiO₂ heterostructure toward organic decomposition.

Chapter 2

Literature Review

2.1 Material properties of palladium oxide

PdO crystal has a tetragonal lattice structure with the lattice constants $a = b = 3.0434 \text{ \AA}$ and $c = 5.3363 \text{ \AA}$, in which each Pd atom is coordinated with four oxygen atoms with a distance of 2.02 \AA in a planar arrangement as shown in figure 2-1 [26]. PdO is known as a p-type semiconductor and its bandgap has a wide reported range from 0.8 to 2.2 eV, depending on crystallinity and purity [14, 19, 27]. Okamoto and Aso [28] have reported the electrical properties of PdO thin films, in which they indicated that PdO has a band gap of $\sim 1.5 \text{ eV}$ and behaves as a p-type semiconductor with a hole mobility of $\sim 17 \text{ cm}^2\text{V}^{-1}\text{sec}^{-1}$. The first optical properties of PdO films were studied by Rey et al. [29] and Nilsson [30] et al.. In both of these studies the samples were prepared by oxidizing the sputtered Pd films at $700 \text{ }^\circ\text{C}$ in air or in O_2 . Nilsson obtained transmittance data in the range 0.5-5.4 eV, from which they used Kramers-Kronig analysis to determine the optical constants. Rogers et al. grew crystals of PdO by vapour transport techniques and determined activation energies from the temperature dependence of their resistivity. The activation energies were determined in the range between 0.04 and 0.1 eV, which was attributed to a high

density of acceptor levels that induced extrinsic p-type conductivity [31]. The nature of the charge carriers was determined from measurements of the Seebeck coefficients referred to copper as a standard. Arai et al. investigated the PdO optical property by light transmission measurements and in situ Raman spectroscopy [14]. They found that the PdO optical property changes dramatically during the phase transformation by heating at $\sim 810\text{-}830\text{ }^{\circ}\text{C}$. However, the feature of optical property of PdO have been employed in super-resolution near-field structure disk by Kim et al. and shown a great carrier-to-noise ratio [32].

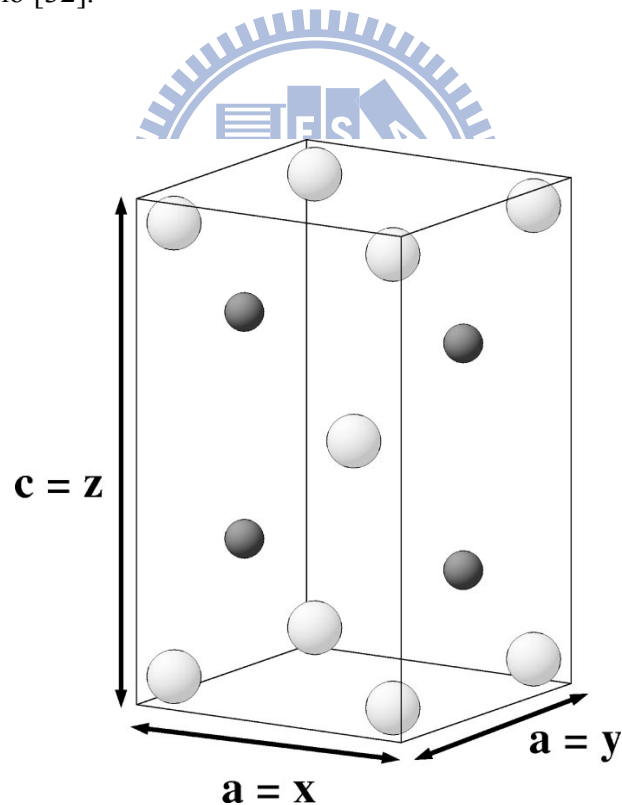


Figure 2-1 The tetragonal bulk unit cell of PdO. Small dark spheres indicate oxygen atoms, large light ones Pd atoms [26].

2.2 Growth methods of Palladium Oxide

2.2.1 Deposition of PdO thin films by sputtering

Aria et al. prepared PdOx thin films by radio-frequency magnetron sputtering and studied their thermal stability [14]. Figure 2-1(a) and (b) shows the SEM images of the PdOx thin films which are sputtered on Si substrates after annealing at 700 °C and 1000 °C for 1 min under N₂ gas flow, respectively. The film thickness is ~100 nm for the as deposited PdO thin films. When the PdOx thin films were annealed at 700 °C, a grain structure with a grain size of 20-30 nm was observed, and the dispersed particles of ~1 μm in diameter are observed for the PdOx thin films annealed at 1000 °C. This significant morphology change of the PdOx film to a particle structure resulted from the thermal decomposition of PdO will give rise to the sharp leap in the transmission intensity as shown in figure 2-1(c). To investigate the thermal decomposition process, the transmitted light intensity of PdOx thin film with 15 nm in thickness was measured during heating up to 1000 °C at an increase rate of 10 °C /min in air. Figure 2-1(c) shows the normalized transmitted light intensity changes using the common wavelengths for optical disk storage systems at $\lambda = 405$ and 635 nm. Both the intensity curves exhibit a sharp drop at 832 °C due to the thermal decomposition of PdO. The high decomposition temperature of PdO indicates that PdO have a high thermal stability. The thermally-induced optical property changes of the reactive sputtered PdOx thin films are expected to provide

useful information for the further development of Super-RENS disks.

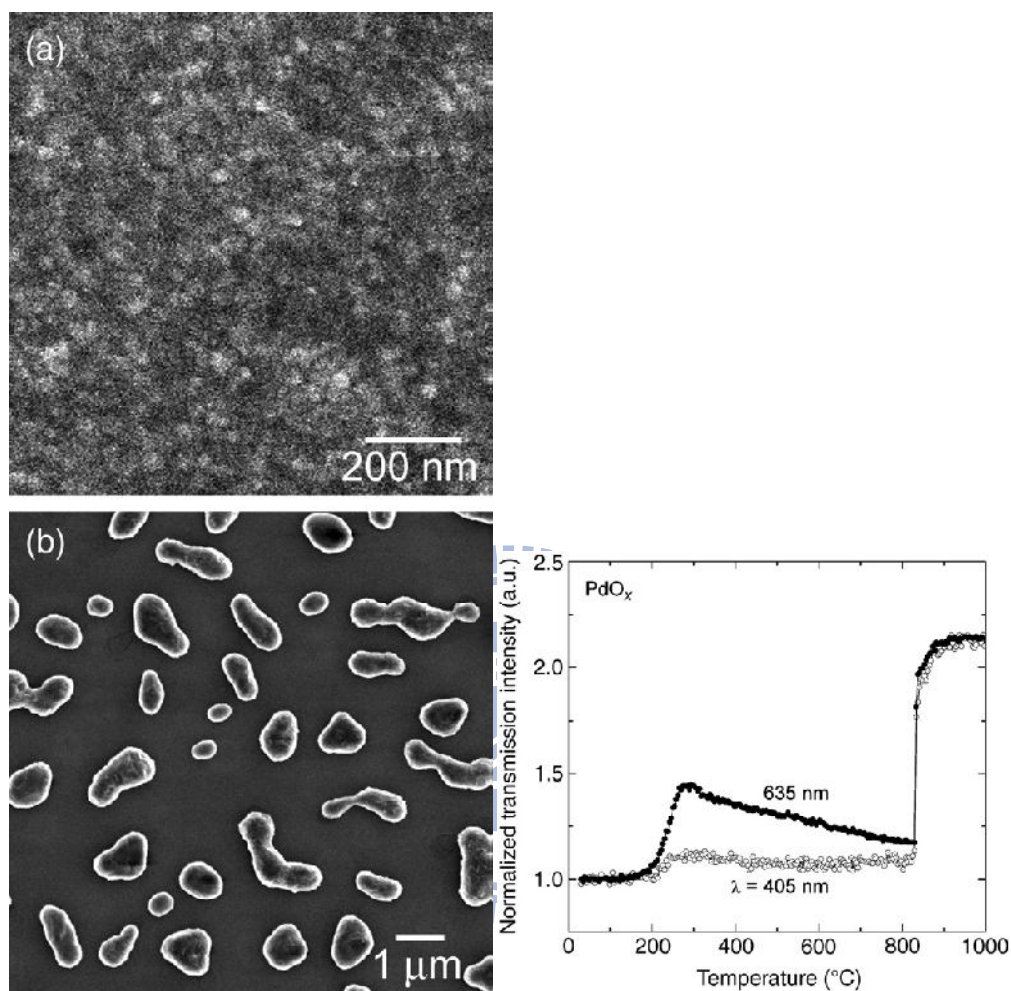


Figure 2-2 SEM images of the sputtered PdO_x thin films annealed at (a) 700 °C and (b) 1000 °C for 1 min under N₂ gas flow. (c) Normalized transmitted light intensity at wavelengths of 405 and 635 nm for PdO_x thin film with a thickness of 15 nm [14].

2.2.2 Formation of PdO nanoparticles by thermal oxidation

Penner et al. prepared the aligned and ordered PdO nanoparticles by thermal oxidation of Pd particles under oxygen for 1 h at 100-400 °C [33]. The

well-defined Pd particles (~5-7 nm) were pre-grown epitaxially on a NaCl (001) substrate by electron-beam deposition at 350 °C and subsequently covered by a layer of amorphous SiO₂ (~25 nm), which was prepared by reactive deposition at a pressure of 10⁻² Pa. The formation of the PdO phase appears at 350 °C and is almost completed at 400 °C. Figure 2-3(a) shows the Pd/SiO₂ nanoparticles after oxidation at 350 °C in 1 bar O₂ for 1 h. A large particle portion still maintains the circular shapes for the as-deposited particles, but a remarkable number of particles have started to crack. The onset transformation does also affect the selected area electron diffraction (SAED) patterns. Although many Pd diffraction rings are still present in figure 2-2(b), the diffraction pattern shows a number of new diffraction rings corresponding to PdO tetragonal lattice structure. Further increasing the oxidation temperature to 400 °C leads to more pronounced crack and almost all particles were well dispersed as shown in figure 2-4. These new small particles exhibit a very narrow size distribution and are typically ~2-3 nm in size as shown in the inset which contains a four-particle line profile. At this oxidation temperature of 400 °C, the SAED patterns exhibiting tetragonal PdO without any Pd single indicates the formation of the PdO phase is almost completed at 400 °C.

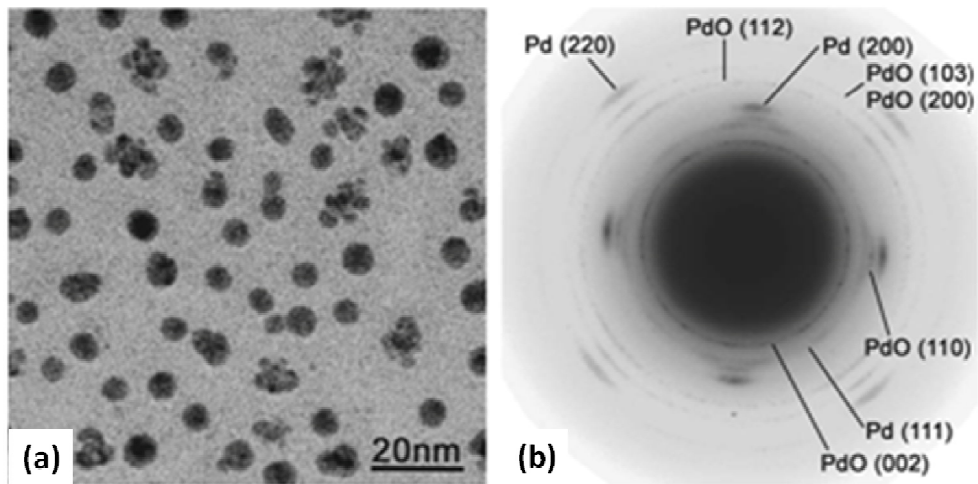


Figure 2-3 The Pd/SiO₂ catalysts after oxidation at 350 °C in 1 bar O₂ for 1 h (a), (b) corresponding SAED pattern [33].

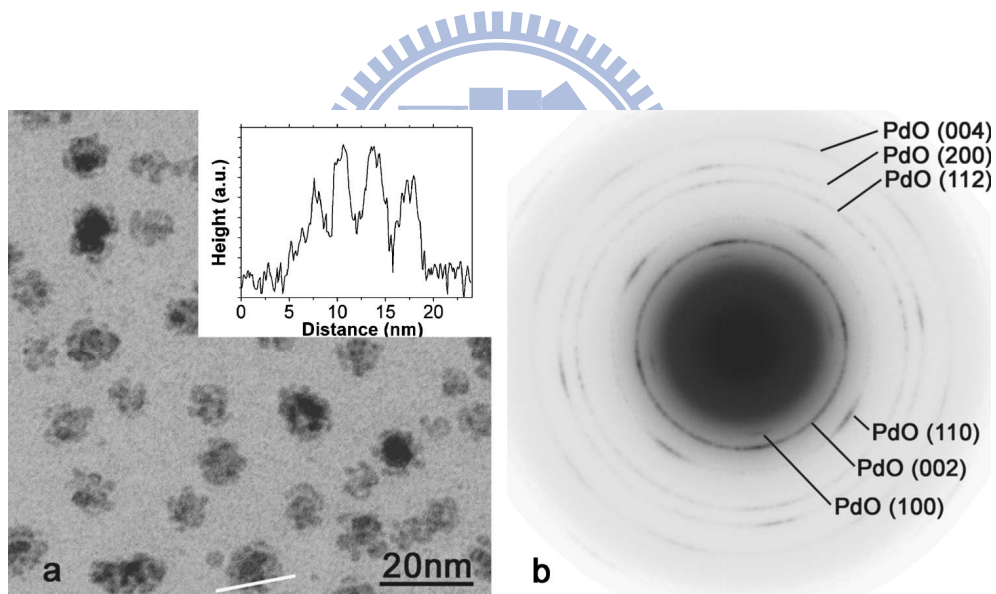


Figure 2-4 The Pd/SiO₂ catalyst after oxidation in 1 bar O₂ at 400 °C for 1 h (a), (b) corresponding SAED pattern [33].

2.2.3 Formation of PdO tips array by thermal oxidation

Aggarwal et al. reported the self-assembly of micrometer-scale hillocks of conducting palladium oxide. Palladium oxide films with a nanotip-like morphology

were produced by relaxing large compressive stresses during thermal oxidation of Pd films [21]. Formation of hillocks in metal films is generally attributed to the relaxation of thermal expansion mismatch stresses between the substrate and Pd. The compressive stresses developed during the heating process will lead to the metal atoms diffusion either through the lattice or along grain boundaries, and then lead to form hillocks. Figure 2-5 shows the AFM image of a polycrystalline Pd film (~120 nm) deposited on a LaAlO₃ substrate after annealed in O₂ at 900 °C for 1 h. It reveals that oxidation accompanies the formation of a uniform array of tips. These arrays with a high surface-to-volume ratio are expected to have many applications in chemical and optical properties. One potential application of these surface-to-volume ratio arrays is as field emitter arrays for vacuum microelectronic devices. The possibility that the large arrays can be self-assembled using an easy fabrication process without any complex lithography makes them applicable for the field emission display in the future.

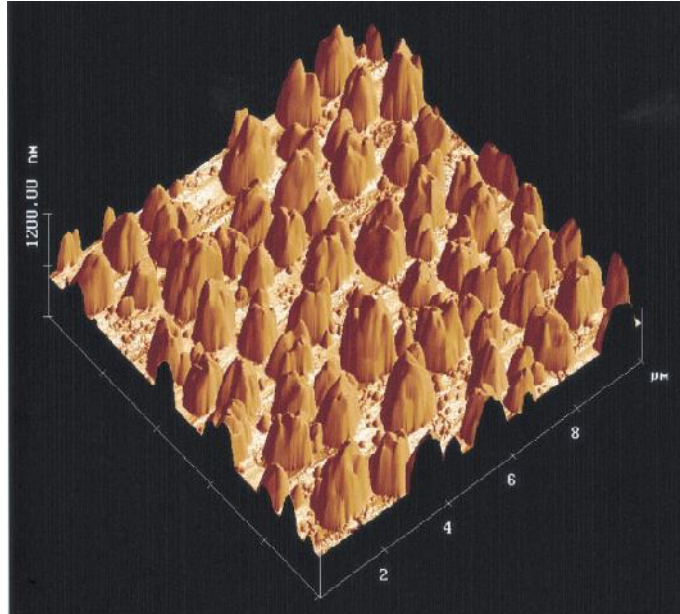


Figure 2-5 AFM image of a Pd film annealed in oxygen at 900 °C [21].

2.2.4 Synthesis of PdO nanofibers by electrospinning

PdO nanofibers using palladium acetate/polycarbonate (Pdac/PC) as the precursor have been synthesized by electrospinning [20]. Figure 2-6 shows the SEM images of Pdac/PC fibers calcined at various temperatures. The surface of the Pdac/PC fibers is smooth due to the amorphous nature of PC as shown in figure 2-6(a) and (b). The surface of fiber became very rough after calcined at 550 °C as shown in figure 2-6(c) and (d). This is due to the decomposition of PC and the formation of metal oxide grain boundaries. When the fibers are calcined at 800 °C, the grains disappeared and the surface became smooth due to the formation of homogenous crystalline phase of palladium metal oxide as shown in figure 2-5(e) and (f).

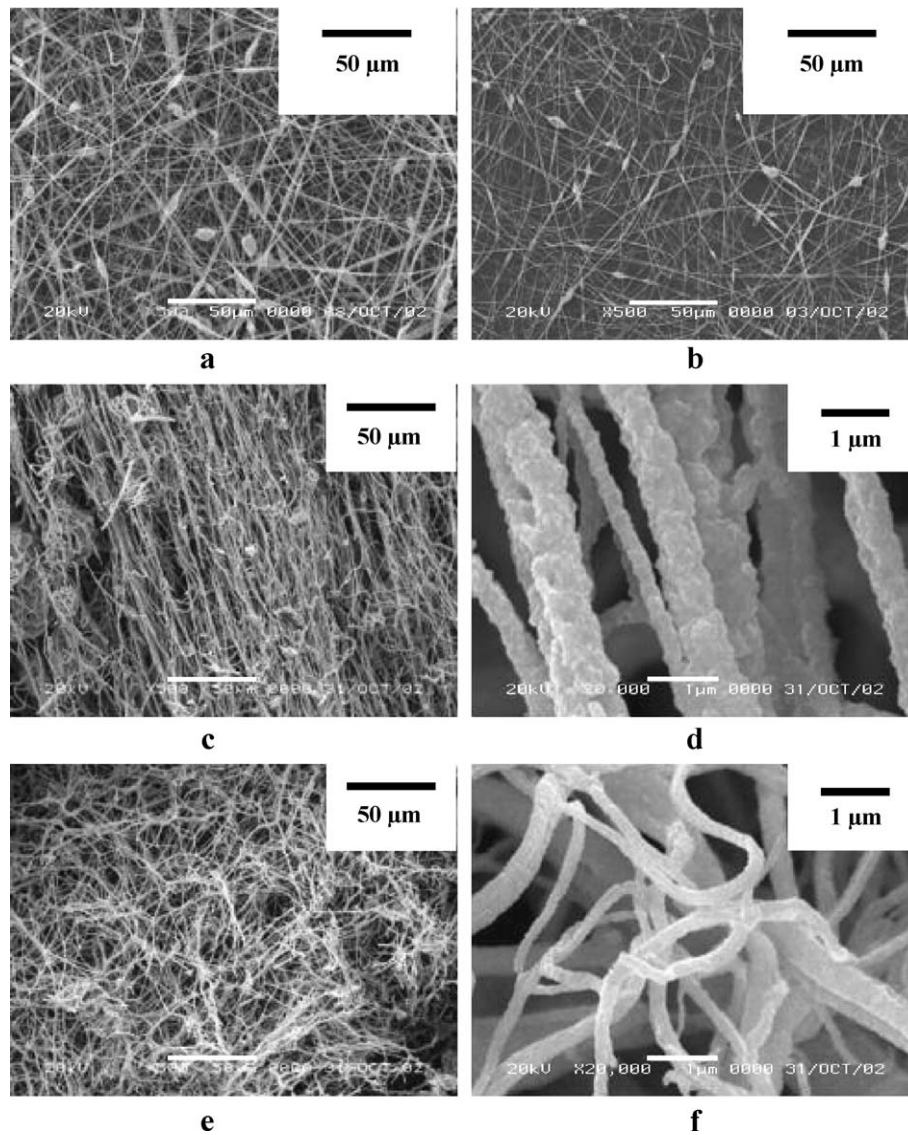


Figure 2-6 SEM images of (a) Pdac/PC fibers with 30 wt.% of palladium acetate; (b) Pdac/PC fibers with 70 wt.% of palladium acetate; (c, d) Pdac/PC calcined fibers at 550 °C; (e, f) Pdac/PC calcined fibers at 800 °C [20].

2.3 Field Emission Theory

The mechanism of field emission is a quantum tunneling effect, in which electrons are extracted from a solid metal or semiconductor surface into vacuum

under an extremely high electric field. Compared with thermionic emission, field emission has many advantages. First, emitters do not need to be heated. Second, the energy of the emitted electrons is also far smaller than thermionic emission, and the emitted current can be readily controlled by the applied voltage [34]. If a sufficient electric field is applied on the emitter surface, electrons will tunnel through the surface-potential barrier across the metal-vacuum interface and escape from the emitter surface, even under a very low temperature. This potential barrier is called work function, which corresponds to the potential difference between Fermi level (E_F) of the emitter and the field-free vacuum. Work function is a surface property of material and its value is related with the electronic structure and orientation of the crystal plane. For a single crystalline palladium, the work function is 5.20 eV for the (110) plane and 5.95 eV for the (111) plane [35]. In order to obtain high emission currents at low voltages, an important desire is to reduce the work function as low as possible.

If an external electric field is applied, the potential barrier at the surface becomes thinner and the vacuum energy level is reduced as shown schematically in figure 2-7 [36]. Then, an electron having energy E_f has a finite probability of passing through the surface barrier. For a material is applied at a field of $\sim 10^7$ Vcm⁻¹, the barrier is sufficiently narrow so that electrons can tunnel through it, even at $T = 0$ K.

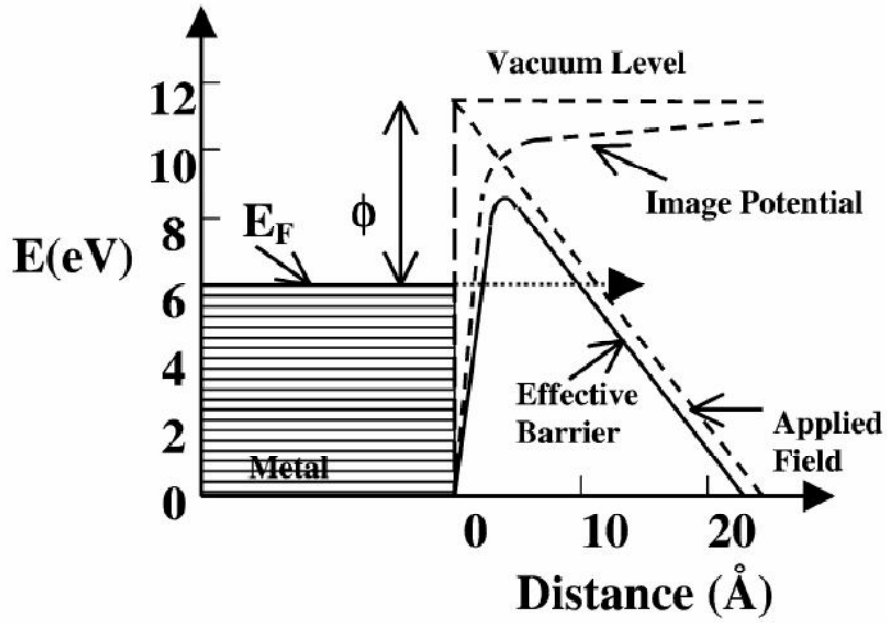


Figure 2-7 Potential-energy diagram illustrating the effect of an external electric field on the energy barrier for electrons at a metal surface [36].

Fowler and Nordheim [37] in 1928 derived a relationship between the field-emission current density (J) from a pure metal and the applied electric field. The widely quoted Fowler-Nordheim (F-N) equation can be expressed as

$$J = \frac{AE^2}{\phi t^2(y)} \exp \left[-\frac{B\phi^{3/2}v(y)}{E} \right] \quad (2.1)$$

where $A = 1.54 \times 10^{-10}$ (A V⁻² eV), $B = 6.83 \times 10^9$ (V eV^{3/2} m⁻¹), $y = 3.7947 \times 10^{-4} E^{1/2} / \phi$,

$t^2(y) \sim 1.1$, and $v(y)$ can be approximated as

$$v(y) = \cos(0.5\pi y) \text{ or } v(y) = 0.95 - y^2 \quad (2.2)$$

Typically, the field emission current (I) is measured as a function of the applied voltage (V). Substituting relationships of $J = I/\alpha$ and $E = \beta V/d$ into Equation (2.1), where α is the emitting area, β is the local field enhancement factor at the emitting surface, and d is the distance between cathode and anode, following equation can be obtained

$$I = \frac{A\alpha\beta^2V^2}{d^2\phi t^2(y)} \exp\left[-\frac{Bd\phi^{3/2}v(y)}{\beta V}\right] \quad (2.3)$$

Therefore, the Napierian logarithm form of Equation (2.3) can be expressed as

$$\ln\left(\frac{I}{V^2}\right) = \ln\left[\frac{A\alpha\beta^2}{d^2\phi t^2(y)}\right] - \frac{Bd\phi^{3/2}}{\beta V} \quad (2.4)$$

Here, a plot of $\ln(I/V^2)$ versus $1/V$ yields a linear curve. This plot is the well known F-N plot, and the slope (S) of the F-N plot is given by

$$S = -\frac{Bd\phi^{3/2}}{\beta} \quad (2.5)$$

The value of field enhancement factor can be estimated from the slope of the measured F-N curve if the work function of the emitter is known. All the field emission sources rely on the field enhancement due to sharp tips or high aspect ratio

of protrusions, so emitters tend to have smaller virtual source sizes because of the primary role of the β factor. The larger the β , the higher is the field concentration, and therefore the lower the effective threshold voltage for emission.

2.3.1 Field emission of PdO nanostructures

PdO nanostructures were grown on Si (111) substrate by electron beam deposition and subsequently oxidized at 1 atm [38]. Figure 2-8(a) shows the AFM image of the PdO film which has nanoparticles with an average height of 9.17 nm, and the rms average roughness of the film was 1.8 nm. The particle density of PdO is 6×10^3 particles/ μm^2 . The pyramidal aspect of the PdO nanoparticles resulted from the strain formed by the lattice mismatch between the Si and PdO lattices. The field emission property was also studied by a diode structure. A typical current-voltage (I-V) measurement on the structures is illustrated in the figure 2-8(b). The I-V characteristic for the structure with a cathode of PdO nanoparticles oxidized at 800 °C shows a maximum current of ~100 nA.

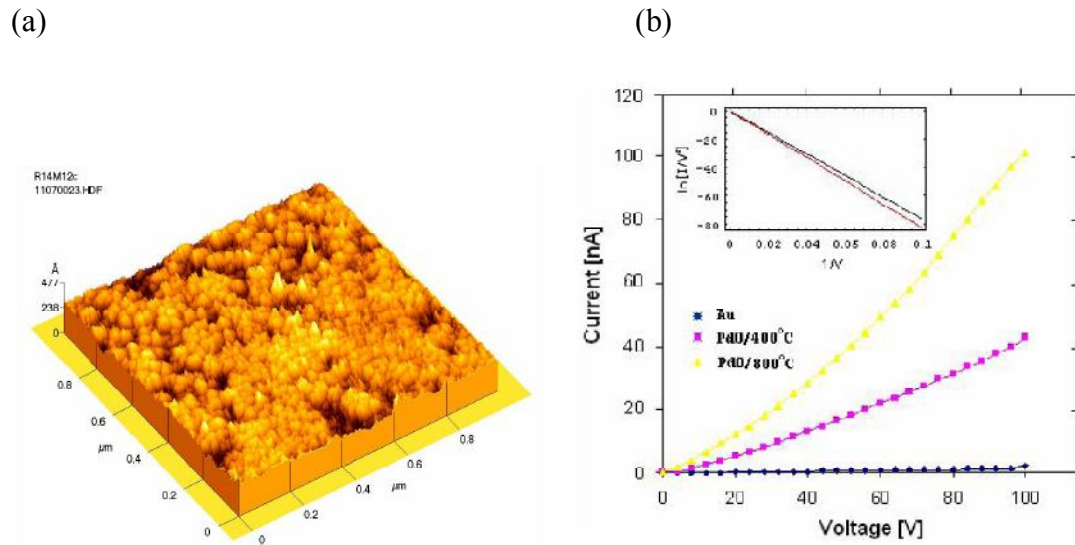


Figure 2-8 (a) AFM of PdO nanoemitters thermal oxidized at 800 °C. (b) I-V characteristic for different cathodes. The line with (■) and (▲) are for PdO nanoparticles oxidized at 400 °C and at 800 °C, respectively. The line with marks (*) is the reference curve for a Si cathode [38].

2.4 Photocurrent generation in metal oxide

Recent photoconduction studies of semiconductor oxides mainly focus on TiO₂ and ZnO, which are n-type semiconductors with wide bandgap energies in UV range. Electron-hole can be generated upon illumination with photon energies larger than the bandgap energy of a semiconductor and forms photocurrent. It is known that oxygen chemisorption plays a central role in regulating the photosensitivity of bulk or thin film, where a UV-sensitivity of similar magnitude has been observed [39-41]. Kind et al. suggested that the similar mechanism can be applied to ZnO nanowire system

[42]. Figure 2-9 shows a schematic of the photoconduction mechanism in the presence of a high density of hole-trap states at the NW surface. In the dark, oxygen molecules adsorb on the nanowire surface as negatively charged ions by capturing free electrons from the n-type ZnO, thereby creating a depletion layer with low conductivity near the nanowire surface as shown in figure 2-9(b):



Upon exposure to UV-light, photo-generated holes migrate to the surface and discharge the adsorbed oxygen ions through surface electron-hole recombination as shown in figure 2-9(c):



At the same time, the photo-generated electrons significantly increase the conductivity of the nanowire. This photoelectric generation suggests that an optical gating (analogous to the conventional electrical gating) is operating within these nanowires rather than a simple light harvesting process. It is expected that thinner nanowires may further enhance the sensitivity of the devices due to its high surface to volume ratio, which may lead to the realization of single photon detection. In addition, the photoresponse is strongly dependent on the ambient gas conditions as well. The photoresponse is slow in vacuum and inert gases (up to several minutes), and fast in air (<1 s).

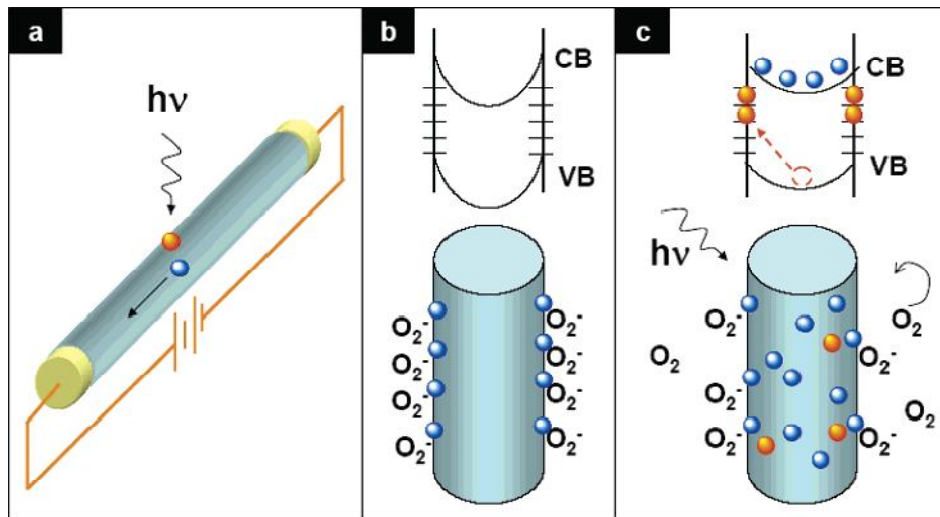
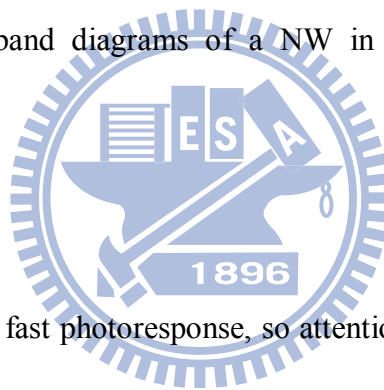


Figure 2-9 schematic of the photoconduction mechanism. (a) Schematic of a NW photoconductor. Upon illumination with a photon energy above E_g . (b) The schematic of the energy band diagrams of a NW in dark. (c) NW Under UV illumination [42].



ZnO materials show a fast photoresponse, so attention has been attracted to such kinds of materials. The materials reported greatly are ZnO single crystals [43], polycrystalline ZnO films [44-45], and ZnO nanostructures [46-47]. It was found that rate of oxygen adsorption and desorption controlled the photoresponse process. Compared with polycrystalline ZnO films, electrons travel through ZnO nanowire films more effectively due to relatively long transport path between boundaries. Therefore, ZnO nanowire films are expected to have a high photoresponse.

The self-organized,[0001] oriented zinc oxide nanowires synthesized with a simple vapor transport and condensation process on sapphire substrates are extremely

sensitive to UV light [47]. Figure 2-10 shows the current-voltage (I-V) curves measured on a 60 nm nanowire in the dark and upon UV-light exposure. A larger photoresponse was detected at higher bias and the I-V curve for the UV-exposed nanowire exhibits nonlinear behavior. The same nonlinear I-V has been observed for both the wire-on-electrode and electrode-on-wire configurations. The four-terminal and two-terminal measurements show identical resistivity values, which suggests that the Au/ZnO contacts may not contribute the nonlinear I-V curves. Figure 2-11 shows the plots of the photoresponse as a function of time. In the measurement process, the UV-lamp was switched on and off. It reveals that the nanowires can be reversibly switched between the low and the high conductivity state. The rise and decay times of the fastest nanowire switches are below 1 s. These photoconducting nanowires could serve as highly sensitive UV-light detectors, chemical and biological sensors, and switching devices for nanoscale optoelectronic applications.

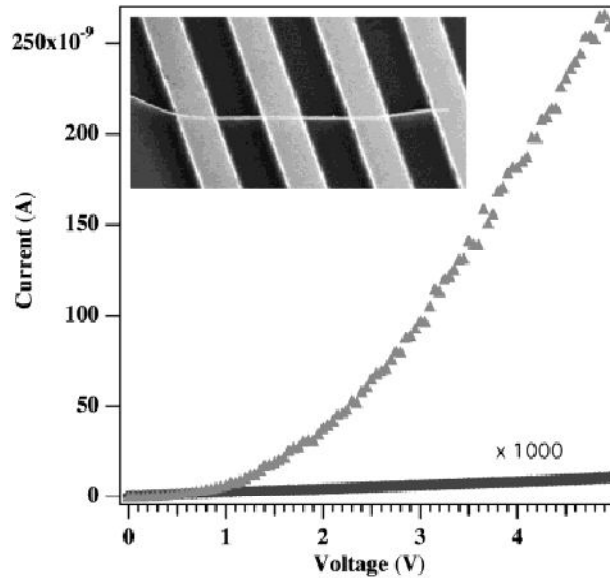


Figure 2-10 I-V curves show dark current (●) and photocurrent (▲) of a single ZnO nanowire under 365 nm, 0.3 mWcm⁻² UV-light illumination. The inset reveals an FE-SEM image of a 60 nm ZnO nanowire bridging four Au electrodes [47].

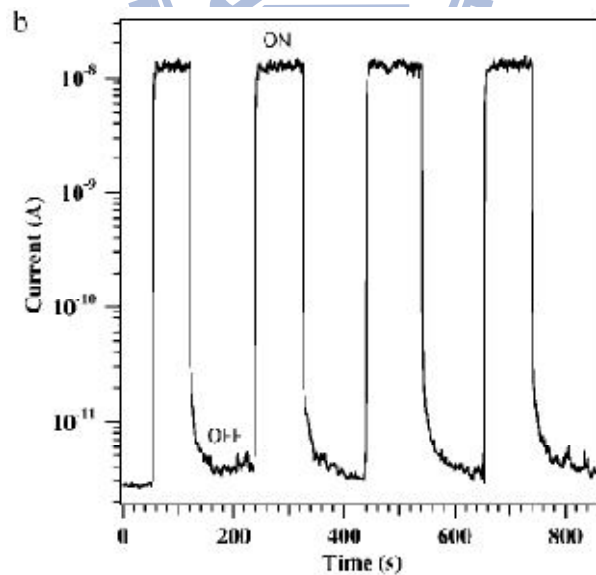


Figure 2-11 Reversible switching of a ZnO nanowire between low and high conductivity states when the handheld UV-lamp was turned on and off. The bias on the nanowire is 1 V [47].

2.5 Photoresponse of PdO

Because PdO has narrow bandgap energy in visible light region, it can be used to enhance the photoresponse of TiO₂ under visible light. Gao et al. prepared PdO/TiO₂ nanocomposites by ployol method [48]. In this synthesis process, Pd(acac)₂ is the Pd precursor, ethylene glycol is the reductant, and nano TiO₂ powder (Degussa P25) is the support, in which the nanoparticles of Pd are highly dispersed on the surface of TiO₂. The Pd/TiO₂ is deposited on the alumina substrate with a comb-like gold electrode, and then it is calcined at various temperatures in air. Figure 2-12 shows the SEM image of the film after calcined at 350 °C, which reveals that the microstructure of the film was composed of the uniform particles and a porous surface morphology. In dark environment, the conductivity of both TiO₂ and PdO/TiO₂ film were very low in room temperature in nitrogen duo to the large resistance of the prepared films. As a comparison, the conductivity of the PdO/TiO₂ film is sharply increased under visible light illumination. Figure 2-13 shows the change of photoconductivity as a function of time under alternate visible light irradiation. During the first 5 min in dark, the film keeps a constant electric current with a very low value. When the lamp was switched on, the current immediately increased. It is a very rapid process at first, and then the photocurrent in the film gradually increased with illumination time.

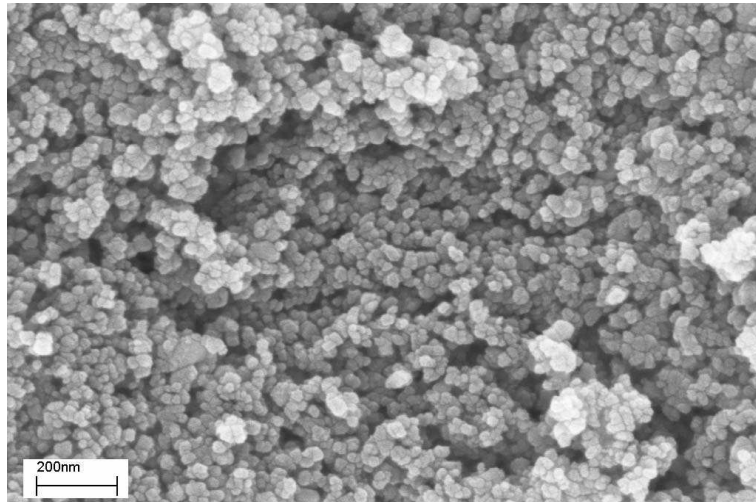


Figure 2-12 FSEM image of the PdO/TiO₂ film calcined at 350 °C [48].

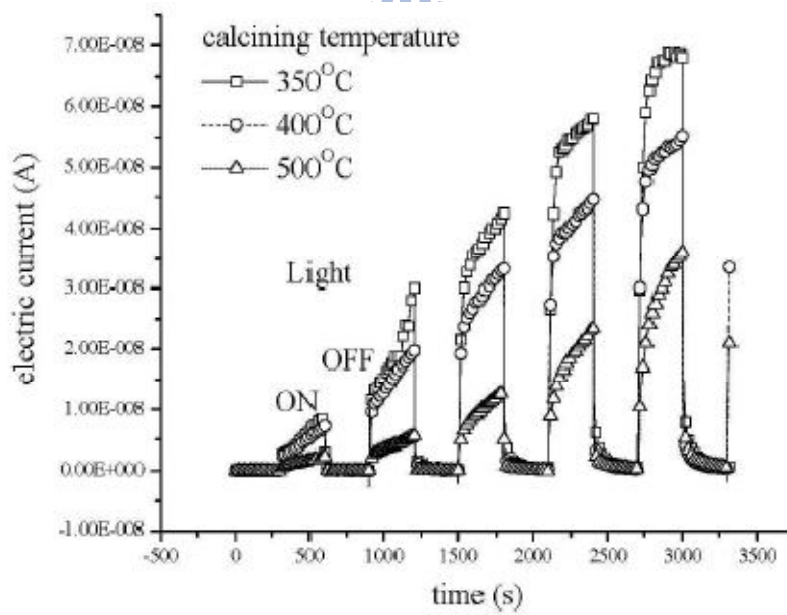


Figure 2-13 Photoconductivity of the PdO/TiO₂ film calcined at various temperatures under visible light in flowing pure N₂ [48].

2.6 Photoexcitation and photocatalytic reaction process of semiconductors

Unlike metals, which have a continuum of electronic states, semiconductors have a void energy region, where no energy levels are available to promote recombination of electron-hole pairs produced by photoactivation in the solid [49]. The void region which extends from the top of the filled valence band to the bottom of the conduction band is called the band gap. When excitation occurs across the band gap there is a sufficient lifetime (nanosecond) for the created electron-hole pair to charge transfer to adsorbed species on the semiconductor surface from solution or gas phase contact. If the semiconductor remains intact and the charge transfer to the adsorbed species is continuous and exothermic the process is termed heterogeneous photocatalysis. The initial process for heterogeneous photocatalysis of organic and inorganic compounds by semiconductors is the generation of electron-hole pairs in the semiconductor particles [49]. The enlarged section of figure 2-14 shows the excitation of an electron from the valence band to the conduction band initiated by light absorption with energy greater than the band gap of the semiconductor. Upon excitation, the separated electron and hole can follow several pathways. Figure 2-14 illustrates some of the pathways for the electrons and holes. The photogenerated electrons transfer to adsorbed organic or to the solvent results from the migration of electrons

and holes to the semiconductor surface. The electron transfer process is more efficient if the species are preadsorbed on the surface. While at the surface the semiconductor can give away electrons to reduce an electron acceptor (pathway C); by turns, a hole can migrate to the surface where an electron from a donor species can combine with the surface hole oxidizing the donor species (pathway D). The probability and rate of the charge transfer processes for electrons and holes depends upon the respective positions of the band edges for the conduction and valence bands and the redox potential levels of the adsorbate species.

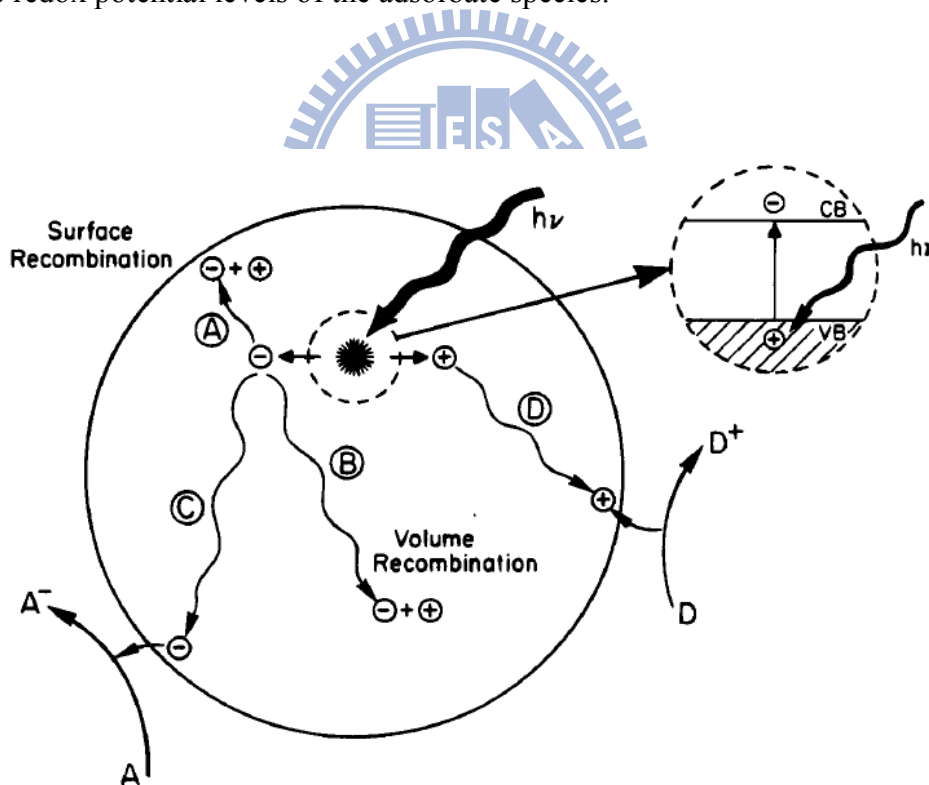


Figure 2-14 Schematic photoexcitation in a solid followed by deexcitation events [49].

2.7 Enhanced Photoactivity of TiO₂ by Heterostructure

The photocatalytic activity and light absorption of TiO₂ can be improved by many sample treatment methods, such as selective syntheses of TiO₂ nanostructures with high-energy surfaces [50] and preparation of nitrogen-doped TiO₂ catalysts [51-52]. However, TiO₂ of a single chemical phase is considered far from a practical photocatalyst due to the lack of visible light absorption and a fast recombination rate of photogenerated carriers [49, 53]. In the past decades, TiO₂ based composites have been extensively studied on the improvement in the photocatalytic performance of TiO₂ by forming a potential barrier at the heterojunction, which can effectively separate photogenerated electron-hole (e-h) pairs and thus decrease the carrier recombination rate [49, 54]. For instance, noble metals, such as Pt [55-56], Au [57] and Ag [58], have been employed to form schottky barriers with TiO₂. Another and more popular approach is to form a heterojunction of TiO₂ with another semiconductors, such as CdS [59], Cu₂O [60-61], Fe₃O₄ [62] and Ag₂O [63], to facilitate fast charge separation and thereby reduce charge carrier recombination [59-60, 64]. In addition to the increase in the lifetime of photogenerated e-h pairs, it is generally believed that these narrow bandgap semiconductors, which usually have a light absorption spectrum covering the visible light range, can also improve the solar energy utilization, resulting in a better photocatalytic performance of TiO₂.

Figure 2-15 shows the morphology of the TiO_2 film/ Cu_2O microgrid heterojunction manufactured by the microsphere lithography method [61]. The underlying TiO_2 film is composed of nanosized particles covered by microgrids of Cu_2O , which are composed of particles smaller than 20 nm. Using the micrograph, the authors can calculate that ~51% of the surface of the TiO_2 film is covered by the Cu_2O microgrid, which indicates that the two semiconductors have similar surface areas exposed to the irradiation source as well as to substances in the solution. The transmittance spectra of the samples coated on the quartz substrate are illustrated in figure 2-16(a). The absorption edge of the Cu_2O film is at ~520 nm, corresponding to a band gap of 2.4 eV, while the band-gap of the TiO_2 film is ~3.2 eV. Because Cu_2O can absorb visible light, deposition of the Cu_2O microgrid on the TiO_2 film will couple these two semiconductors to absorb both UV and visible light as shown in the schematic energy diagram of figure 2-16(b). The TiO_2 film/ Cu_2O microgrid heterojunction possesses a higher photocatalytic activity than the bare TiO_2 and Cu_2O films under UV-vis light irradiation as shown in figure 2-17. Several factors result in the high photocatalytic activity of the TiO_2 film/ Cu_2O microgrid heterojunction. First, TiO_2 and Cu_2O absorb UV and visible light respectively to generate electron-holes pairs, which will migrate to the surface of the particles and accomplish the photocatalysis procedure. The similar opportunity that each of TiO_2 and Cu_2O

has to be exposed to the adsorbates reduces the recombination. Meanwhile, the excited electrons on Cu_2O can also transfer to TiO_2 because the conduction band of Cu_2O is less anodic than that of TiO_2 , facilitating the charge separation and efficiency of the photocatalysis process. Furthermore, the electron-hole separations are also driven by the built-in electric fields in the heterojunction because Cu_2O is a p-type semiconductor and TiO_2 is an n-type semiconductor. Therefore, the TiO_2 film/ Cu_2O microgrid system exhibits much higher photocatalytic activity than the bare TiO_2 and Cu_2O films.

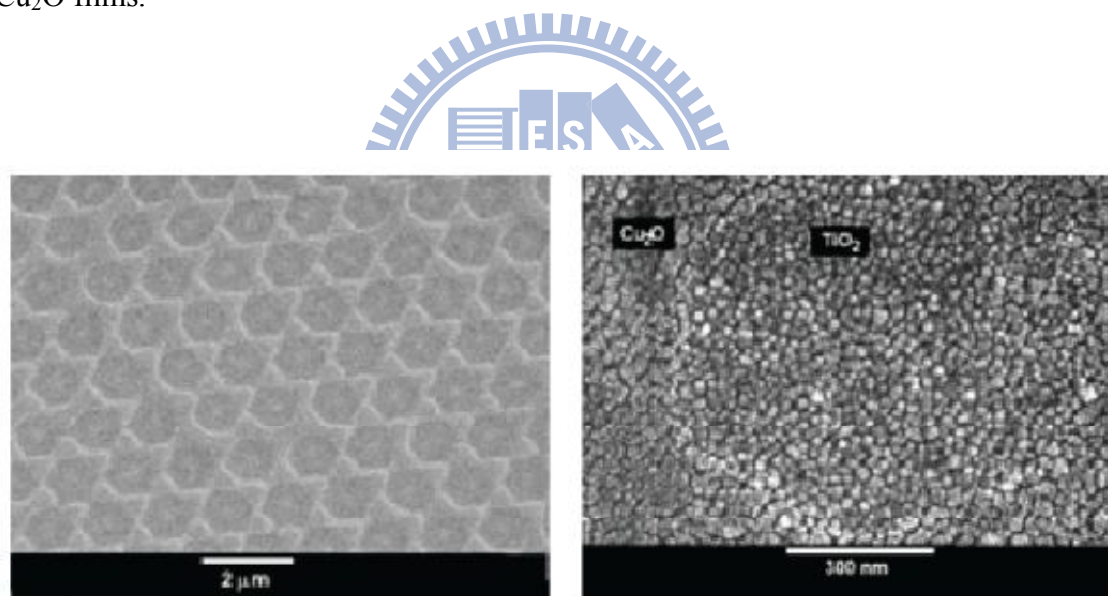


Figure 2-15 SEM micrographs of the TiO_2 film/ Cu_2O microgrid heterojunction [61].

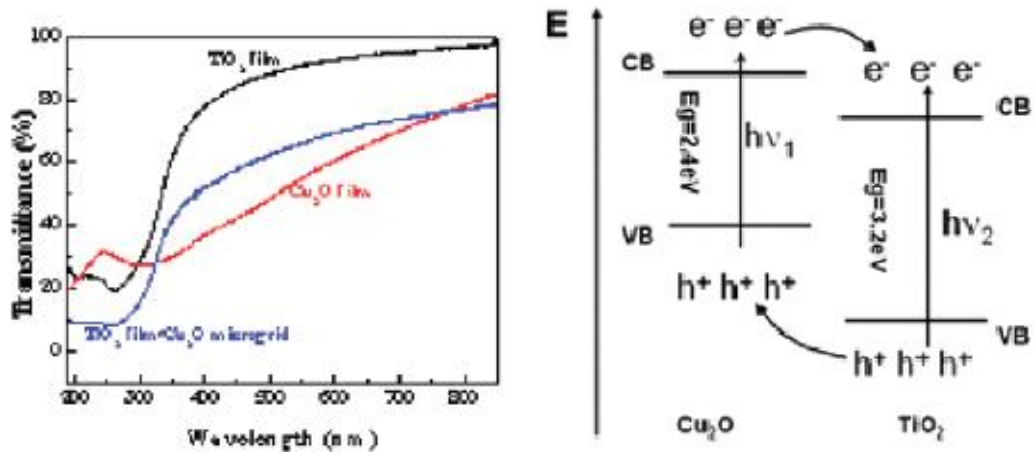


Figure 2-16 (a) Transmittance spectra of the TiO₂ film, Cu₂O film, and TiO₂ film/Cu₂O microgrid heterojunction. (b) Schematic energy diagram of Cu₂O and TiO₂ [61].

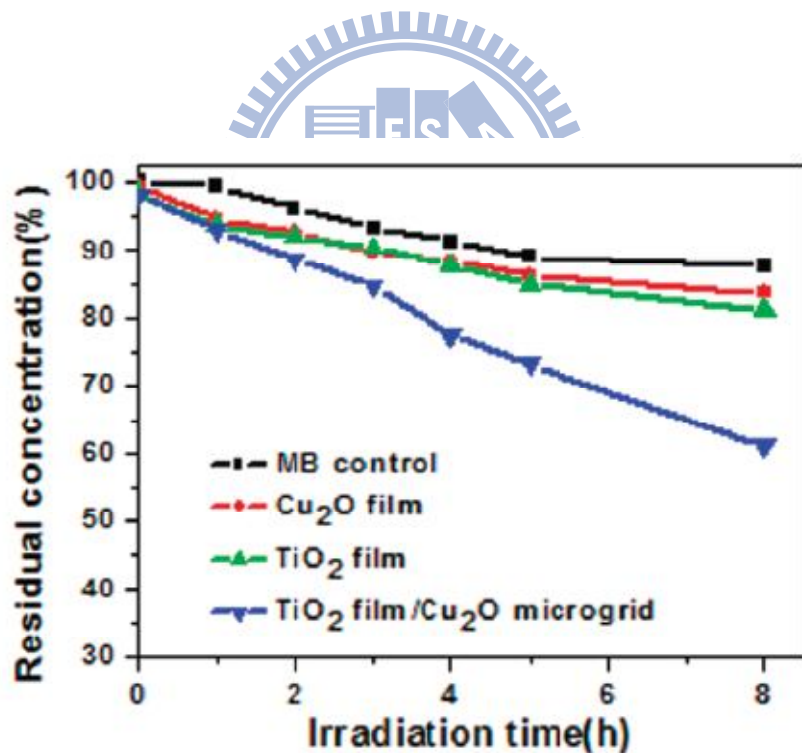


Figure 2-17 Photocatalytic decomposition of MB by the Cu₂O film, TiO₂ film, and TiO₂ film/Cu₂O microgrid heterojunction under irradiation of UV-vis light [61].

2.8 Enhanced Photoactivity of TiO₂ by PdO

PdO has a bandgap energy in the visible light range, thus it has been widely used as a modifier to enhance visible-light absorption for many wide-band-gap oxides, such as TiO₂ and SnO₂. The PdO-assisted visible-light absorption enhancement is particularly desirable for those applications demanding a large active surface area, such as photocatalysis, gas sensing and microbial inactivation. For instance, PdO nanoparticles formed in TiO₂ thermally impregnated with Pd was found to be important for photocatalytic oxidation of NO in gas phase [22]. Figure 2-18 shows the NO conversion efficiency on 0.05 wt.% Pd/TiO₂ and P25 with different inlet concentration of NO. The photocatalytic oxidation efficiency of NO both decline with the increase of NO concentration. For P25, the conversion of NO was 72.4% when the inlet concentration is 85 ppm, and decreased to 25.8% when the inlet concentration reaches 310 ppm. It had been reported that the reaction rate which placed on the Degussa P25 was limited by the Langmuir-Hinshelwood model, where the reaction was first-order at low concentrations and zero-order at high concentrations. However, the photocatalytic activity of 0.05 wt.% Pd/TiO₂ performed well at higher concentration of NO. The conversion of NO (87.2%) is ~1.13 times that of P25 (72.4%) at inlet NO concentration of 85 ppm, while the conversion (60.3%) is ~2.34 times that of P25 (25.8%) at 310 ppm. The result

indicates that the Pd/TiO₂ photocatalysts have a higher activity and could be potentially applied to oxidize higher concentration of NO.

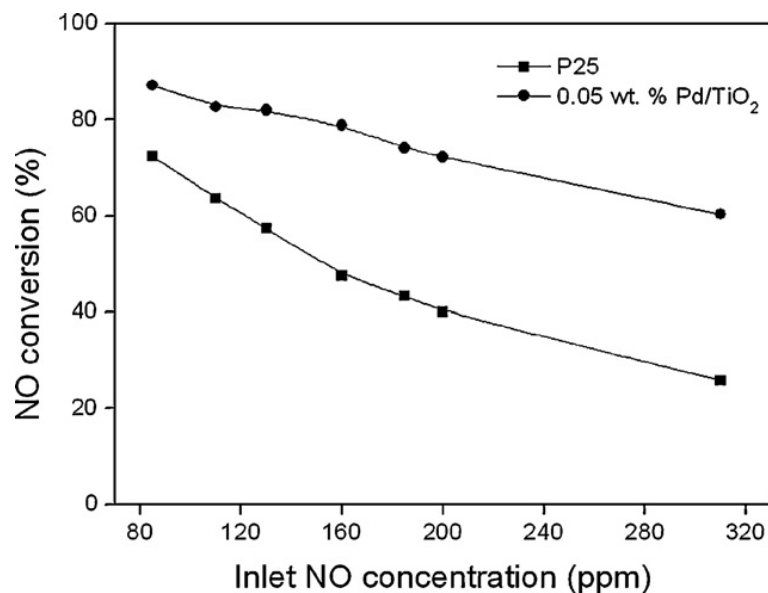


Figure 2-18 Effect of NO conversion efficiency with initial NO concentration after 1200 min irradiation using P25 and 0.05 wt.% Pd/TiO₂. *Conditions:* 125W Hg-arc, 80 °C, 75% RH, 10 s space time and 21% O₂ concentration [22].

2.9 Enhanced Photoactivity of SnO₂ by PdO

PdO can enhance the photoactivity of SnO₂ toward microbiogenic reactions [24] under visible light irradiation. The optical absorbance of bare SnO₂ and 1% palladium over tin dioxide (1% PdO/SnO₂) samples were analyzed. As observed from figure 2-19, a wide absorbance band between 200 and 360 nm was obtained for bare SnO₂ and between 270 and 360 nm for 1% PdO/SnO₂ samples. 1% PdO doped

sample yields much higher absorbance than the bare SnO₂ indicating the metal doping dominates the optical absorbance in the UV range. The most important point of this analysis is the wide blue shift of bare SnO₂ absorbance band to the higher energy, while the optical edge around 360 nm was observed for both SnO₂ and PdO/SnO₂ sample. The photocatalytic antibacterial properties of SnO₂ and PdO/SnO₂ coated glass samples were also performed to verify the effect of palladium doping on semiconductor photocatalytic materials. Similar inactivation experiments were conducted with bare SnO₂ and PdO/SnO₂ coated glass samples against *E. coli*. As shown in figure 2-20, 56 and 68% inactivation of *E. coli* was observed on SnO₂ and PdO/SnO₂ films after 2 h irradiation, respectively. It revealed that palladium doping on the SnO₂ semiconductor catalyst can increase the photocatalytic activity. The first order kinetic analysis of the inactivation data against *E. coli* yield 0.007 and 0.008 min⁻¹ for bare SnO₂ and palladium doped SnO₂ coated glass samples, respectively.

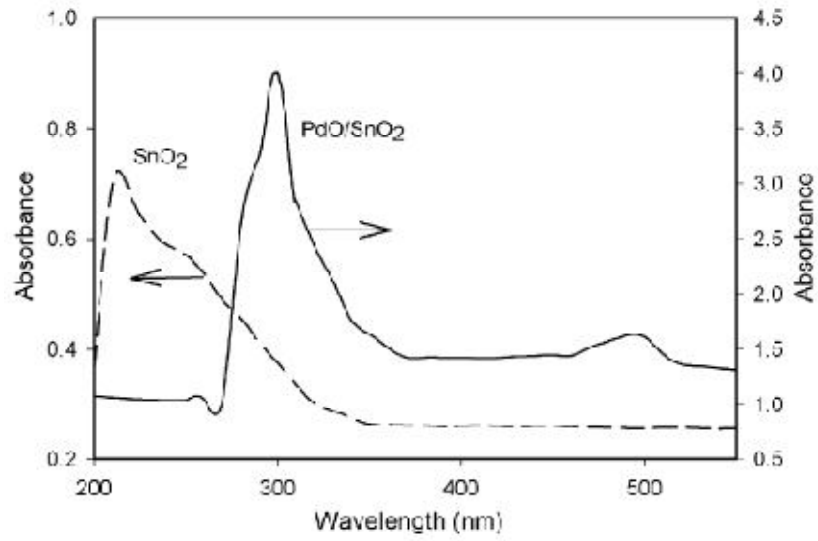


Figure 2-19 UV-vis spectra of bare SnO₂ and PdO/SnO₂ samples [24].

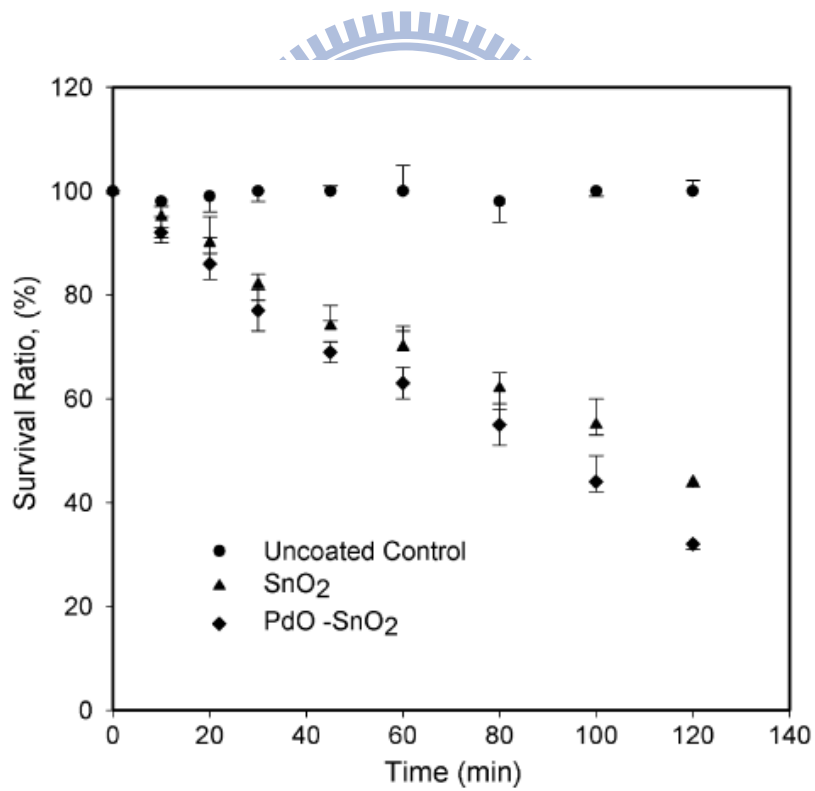


Figure 2-20 Effect of irradiation time (10 mW/cm²) on the survival ratio of *E. coli* over SnO₂ and PdO/SnO₂ films[24].

Chapter 3

Experimental methods

3.1 Experimental flowchart

Figure 3-1 illustrates the experimental flowchart of preparations and analyses of Pd-PdO coreshell nanoflakes, single-crystalline PdO nanoflakes and PdO/TiO₂ heterostructure. Arrows of different colors stand for different experiment purposes and applications such as field emission (F-E), photocurrent (P-C) and photocatalysis (P-cata.). The surface morphology of the PdO nanoflake thin film was examined by scanning electron microscopy (SEM), and the chemical composition was characterized by x-ray photoelectron spectroscopy (XPS) and Auger electron spectroscopy (AES). X-ray diffractometry (XRD) and transmission electron microscopy (TEM) were used to study the microstructure of the nanoflakes. UV-vis absorption spectra were measured on a spectrophotometer in the diffuse reflectance mode. The field emission measurements (*J-E*) of the specimens were conducted by the simple diode configuration and performed in high vacuum. The photocurrent was generated by illuminating the PdO sample with a UV light source with the primary wavelength at 365 nm, and was measured by a Keithley source meter. The photocatalytic activity of PdO/TiO₂ heterostructures are measured by using An

aqueous MB solution of 1×10^{-5} M as the test reagent

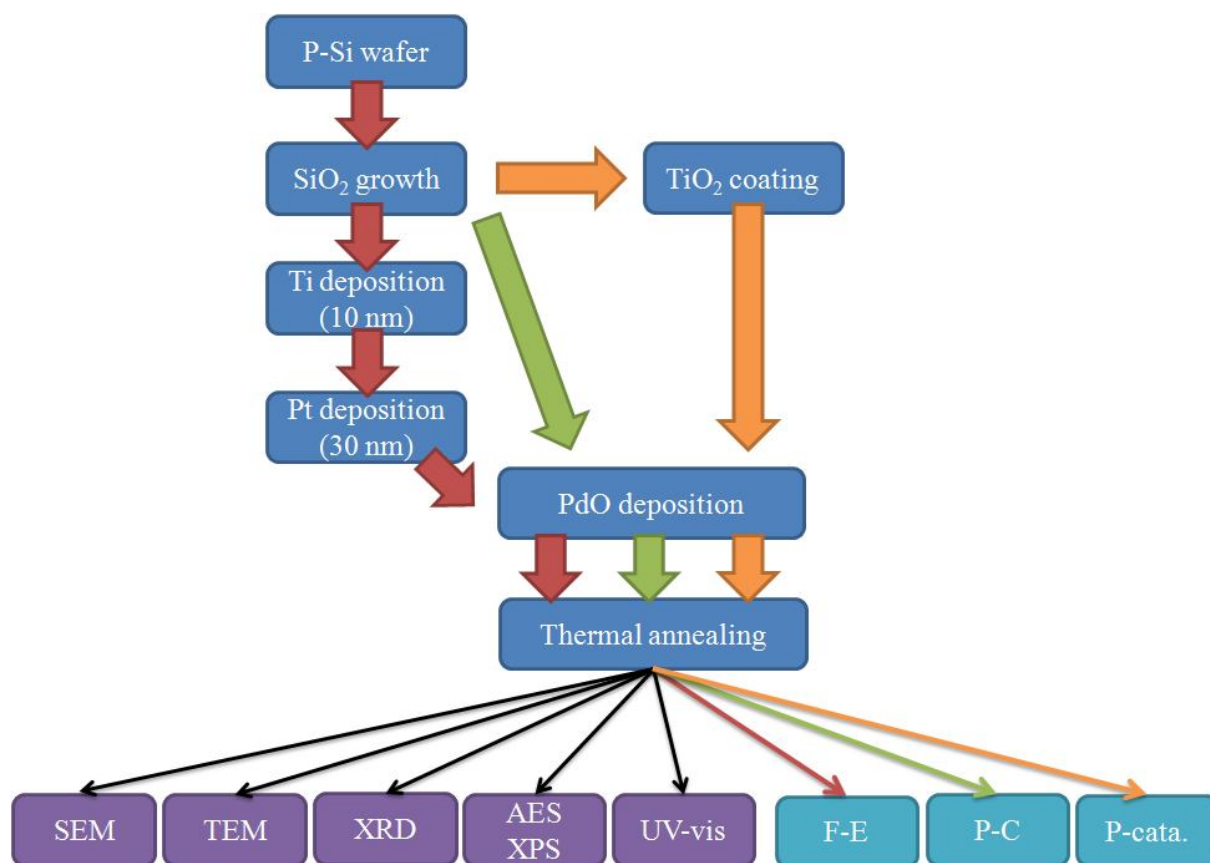


Figure 3-1 Experimental flowchart for the fabrications and analyses of the Pd-PdO core-shell nanoflakes, single-crystalline PdO nanoflakes and PdO/TiO₂ heterostructures.

3.1.1 Preparation of PdO nanoflakes

Deposition of PdO nanoflakes was carried out in a radio frequency magnetron sputter deposition system. The palladium target was 2 in in diameter and with a purity of 99.99%. Reactive sputter deposition was performed with a gas mixture of Ar (20 sccm) and O₂ (20 sccm) at the working pressure of 9×10^{-3} torr and the rf power

of 50 w. The sample preparation is started with thermal growth of an SiO₂ layer 100 nm thick on a 6 in P-type (100) silicon wafer. The SiO₂ thin film was grown on an RCA-cleaned Si wafer at 980°C for 22 min in a gas mixture of O₂/H₂ (5 slm/8 slm) at 1 atm. A Ti layer 10 nm thick was then deposited by electron-beam-evaporation (e-beam) on the oxide as an adhesion layer for the subsequently e-beam deposited Pt thin film with a thickness of 30 nm. The nanoflake film was then deposited on the Pt film at various temperatures. The nanoflake film was also deposited on the SiO₂ film at a substrate temperature of 25°C and then annealed at various temperatures.

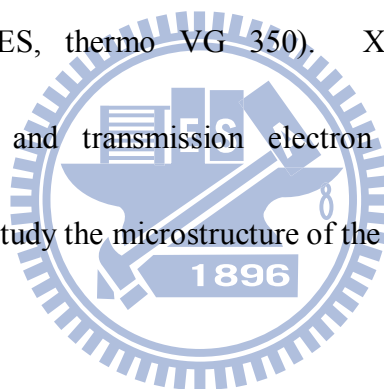
3.1.2 Preparation of PdO/TiO₂ heterostructures

The PdO/TiO₂ heterostructure was prepared by depositing PdO nanoflakes on TiO₂ nanoparticles, which were dispersed on a 150 nm thick SiO₂ thin film thermally grown on a 6 in. p-type Si(100) wafer. To disperse TiO₂ nanoparticles on the SiO₂ substrate, we first prepared the suspension solution of commercial Degussa TiO₂ powders (P-25) in ethanol at room temperature in an ultrasonic bath. The P-25 suspension solution was then spun on the substrate, followed by drying at 120°C. Deposition of PdO on the P-25 TiO₂ nanoparticles was carried out at room temperature in a radio frequency magnetron sputter deposition system. Five PdO/TiO₂ heterostructure thin films with different PdO deposition times (1, 3, 4, 8 and 12 min) were prepared, and denoted, respectively, as TiO₂-PdO-1, TiO₂-PdO-3,

TiO₂-PdO-4, TiO₂-PdO-8 and TiO₂-PdO-12 according to the deposition time. The as-prepared PdO/TiO₂ heterostructure thin film was annealed at 400°C for 2h to improve the crystallinity of the PdO nanoflakes before photocatalysis tests.

3.1.3 Characterizations of PdO nanoflakes and PdO/TiO₂ heterostructures

The surface morphology of the PdO nanoflake thin film was examined by scanning electron microscopy (SEM, JEOL JSM-6500F), and the chemical composition was characterized by x-ray photoelectron spectroscopy (XPS) and Auger electron spectroscopy (AES, thermo VG 350). X-ray diffractometry (XRD, PANalytical X'Pert Pro) and transmission electron microscopy (TEM, JEOL JEM-3000F) were used to study the microstructure of the nanoflakes.



3.2 Radio frequency magnetron sputter deposition system

There are several sputtering systems for thin films deposition. Among these sputtering systems, the basic model is the DC diode sputtering system. The other sputtering system such as RF sputtering, is the improved systems from the DC diode sputtering. Following are the introduction of DC and RF sputtering.

(a) DC sputtering

The DC sputtering system is composed of a pair of planar electrodes. One is cathode and the other is anode. The substrates are set as anode. When Ar gas inlet

into the sputtering chamber and several kilovolts of DC voltage are applied between the two electrodes, the glow discharge is initiated. The Ar ions in the glow discharge are accelerated at the cathode and sputter the target resulting in the deposition of thin film on the substrates.

(b) RF sputtering

The difference between the DC and RF sputtering is power supply system. For RF sputtering, the power supply is operated at a high frequency. The frequency set at 13.56 MHz for the sputtering is as regulated by the U.S. Federal Communication Commission. The RF diode operates with a slightly different way from the DC diode. For a small part of the RF cycle, the cathode and anode are electrically reversed. It eliminates charge built on an insulating surface by providing an equal number of ions, electrons, ions, and so on. This allows insulators or metals to be sputtered. The other advantage of the RF sputtering system is that the oscillation of fields in the plasma (at the driving frequency) results in additional electron motion within the plasma. Figure 3-2 shows the Schematic diagram of our plasma sputtering System.

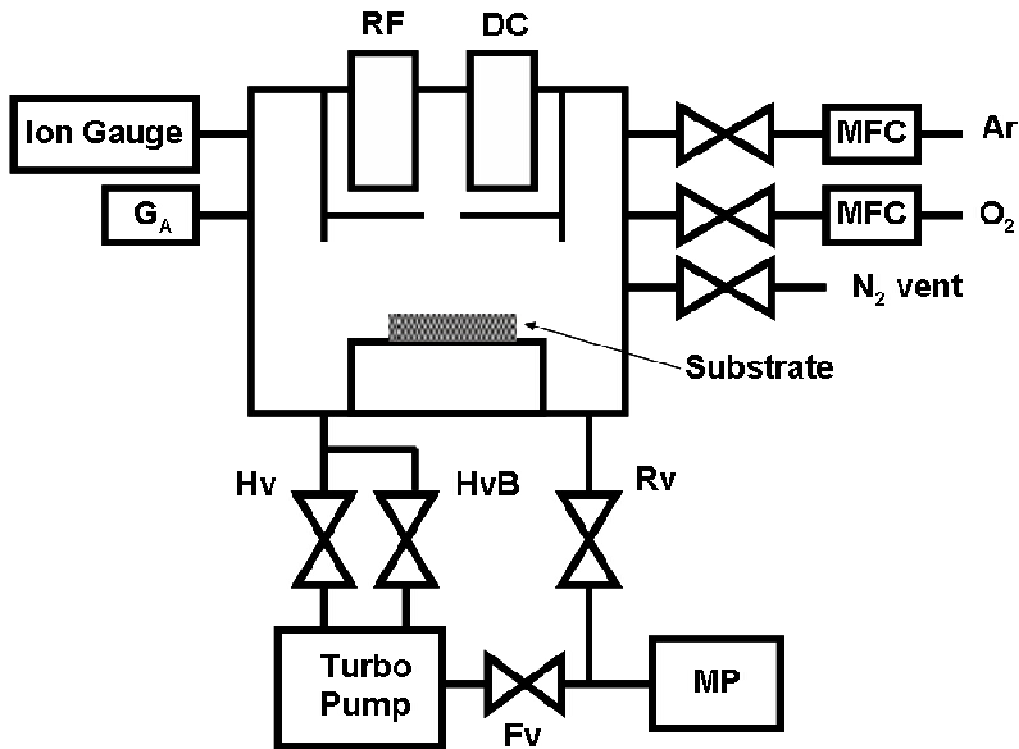


Figure 3-2 Plasma sputtering System.

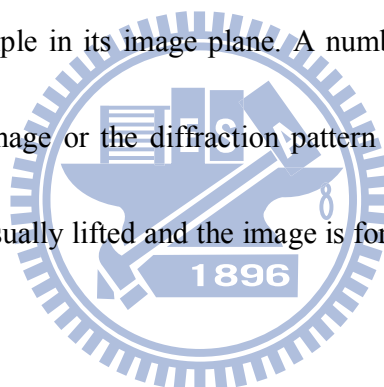
3.3 Materials Characterizations

3.3.1 Scanning Electron Microscope (SEM)

SEM is very powerful tool for observing surface morphology of specimens, which equips with an electron gun accelerated under 0.4-40kV voltage to generate electron beams and use secondary electrons or backscattered electrons detectors to form images by passing the signal to computer. In this study, the morphology of the PdO nanoflake thin films and PdO/TiO₂ heterostructures are characterized by a field-emission SEM (JEOL JSM-6500F), in which the accelerating voltage is set at 15kV with a emission current of 10μA. The working distance is 10mm and the working pressure is under 9.63×10^{-5} Pa.

3.3.2 Transmission Electron Microscopy (TEM)

This is the most important instrument to study the crystal structure and defects of materials in depth. TEM reveals the interior microstructure of the specimen, and it can give the high-resolution lattice image and the electron diffraction pattern as well. In this study, transmission electron microscopy (TEM) (JEOL JEM-2100F) is operating at 200 kV accelerating voltage. Transmitted and diffracted electrons are recombined by objective lens to form a diffraction pattern in the back focal plane of that lens and a magnified image of the sample in its image plane. A number of intermediate lenses are used to project either the image or the diffraction pattern onto a fluorescent screen for observation. The screen is usually lifted and the image is formed on photographic film for recording.



3.3.3 X-ray Photoelectron Spectroscopy (XPS)

Surface analysis by XPS includes of irradiating a solid in vacuum with monoenergetic soft X-rays and analyzing the energy of emitted electrons. The spectrum is plotted as the number of detected electrons versus their kinetic energy. Quantitative data can be obtained from peak intensity or integration areas, and the chemical states of elements can be identified from exact peak positions and separations. In this study, XPS was used to analyze the chemical states of palladium

oxide nanoflakes. XPS analyses were performed on a Thermo VG Scientific 350 system with Mg α -K α (1253.6 eV) excitation. X-ray emission energy was 300 W with 10 kV accelerating voltage.

3.3.4 Auger Electron Spectroscopy (AES)

AES analysis technique employs an electron beam (10 keV) irradiating the specimen surface to excite Auger electrons which have specific energy. By analyzing the kinetics energy of the Auger electrons, we can identify the element composition and chemical state of the specimen. Because the incident electrons with low-energies (1-3 keV) have very short inelastic mean free paths (5-20 Å) in the solid materials, AES technique is usually used to catch the information within 50 Å away from the surface (surface analysis). In this study, AES was employed to investigate the bonding structure of the PdO nanostructures and to study the atomic composition of the nanodots as a function of the time of argon ion sputtering (depth profiling). The AES analyses were performed using a Thermo VG Scientific 350 Auger system with a Schottky field emission electron source.

3.3.5 X-ray diffractometry (XRD)

X-ray diffraction (XRD) is a versatile technology for exhibiting detailed material information of chemical composition, crystal orientation and crystal structure. The

diffraction angle and the associated peak intensity are the unique characteristic of crystalline materials. Therefore, various crystal structure information of the specimen can be determined by XRD. In this study, the crystal structure of the prepared PdO, Pd-PdO core-shell nanoflake thin films and PdO/TiO₂ heterostructures was analyzed by X-ray diffractometry (PANalytical X'Pert Pro). The Cu-K α line at 0.15406 nm was used as the source for diffraction as 2 θ from 30-90 degree.

3.3.6 UV-Vis Absorption Spectroscopy

UV-vis spectroscopy is the measurement of the wavelength and intensity of near-ultraviolet and visible light absorbed by specimens. UV-vis spectroscopy is usually applied to molecules and inorganic ions or complexes in solution. The UV-vis spectra have broad features that are of limited use for sample identification but are very useful for quantitative measurements. The concentration of an analyte in solution can be determined by measuring the absorbance at some wavelength. The bandgap of a semiconductor can also be measured by the UV-Vis Absorption Spectroscopy in the diffuse reflectance mode. UV-vis spectra analyses are performed on a Hitachi U-3900H system.

3.4 Measurement of PdO nanoflakes photoelectric properties

3.4.1 Field Emission Measurement

Field emission measurements of the nanoflakes were carried out under a vacuum condition of 5.0×10^{-6} torr with a high voltage measurement source (Keithley 237), using the planar capacitor measurement configuration. The separation between the nanoflake cathode and the indium tin oxide (ITO) coated anode plate was 100 μm . The Schematic diagram of the field emission measurement system is shown in figure 3-3.

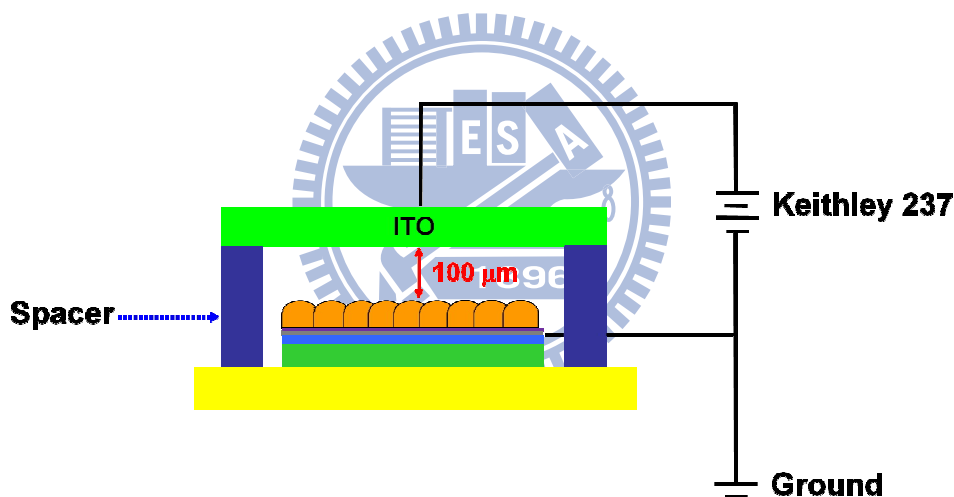


Figure 3-3 Schematic diagram of the field emission measurement.

3.4.2 Photoresponse Measurement

The photocurrent was generated by illuminating the PdO sample with a UV light source with the primary wavelength at 365 nm, and was measured by a Keithley source meter (model No. 2400). The measurement structure has two Ag paste electrodes 1 cm apart on a PdO thin film stripe as shown in figure 3-4. By carefully

defining the contact area of the Ag electrodes on the PdO sample during the electrode preparation, the UV-illuminated region was limited to an area of $\sim 1 \times 1 \text{ cm}^2$. The measured current is thus directly referred to as the current density.

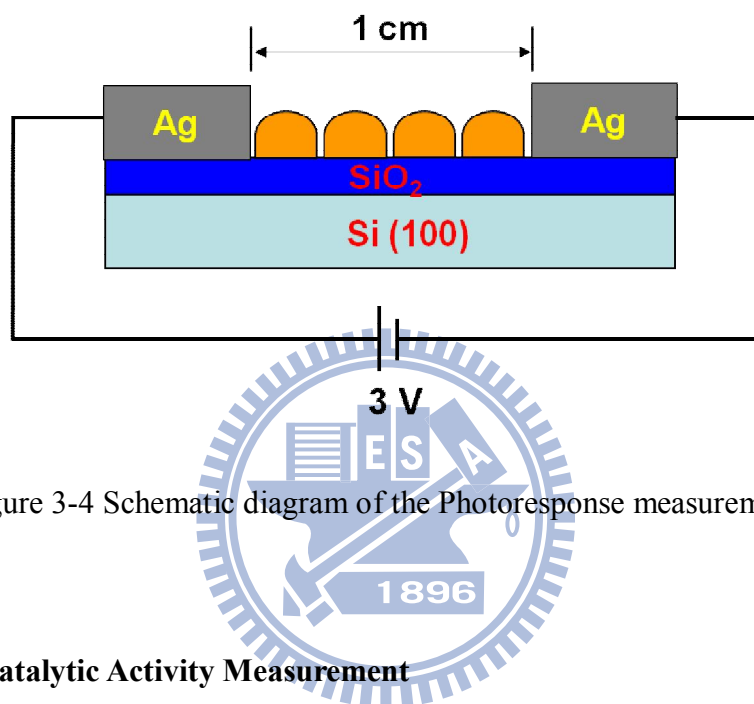


Figure 3-4 Schematic diagram of the Photoresponse measurement.

3.4.3 Photocatalytic Activity Measurement

An aqueous MB solution of $1 \times 10^{-5} \text{ M}$ was used as the test reagent in the study. Fifty milliliters of the MB solution was transferred to a cuboid quartz tube ($3 \times 3 \times 8 \text{ cm}^3$) and, prior to light irradiation, the solution was stirred for 30 min in dark to stabilize MB adsorption on the wall surface of the test tube. A 250 W Xe lamp was used as the UV/vis light source. An edge filter ($\lambda < 420 \text{ nm}$) was used when visible light source is required. The photocatalyst sample was cut into a square shape with an area of $\sim 2 \times 2 \text{ cm}^2$. The distance between UV/vis light source and photocatalyst sample is $\sim 1 \text{ m}$. The concentration of the MB was evaluated using a Hitachi

U-3900H UV-vis spectrophotometer by measuring the absorption peak at 665 nm.

The experimental instrument is shown in figure 3-5.

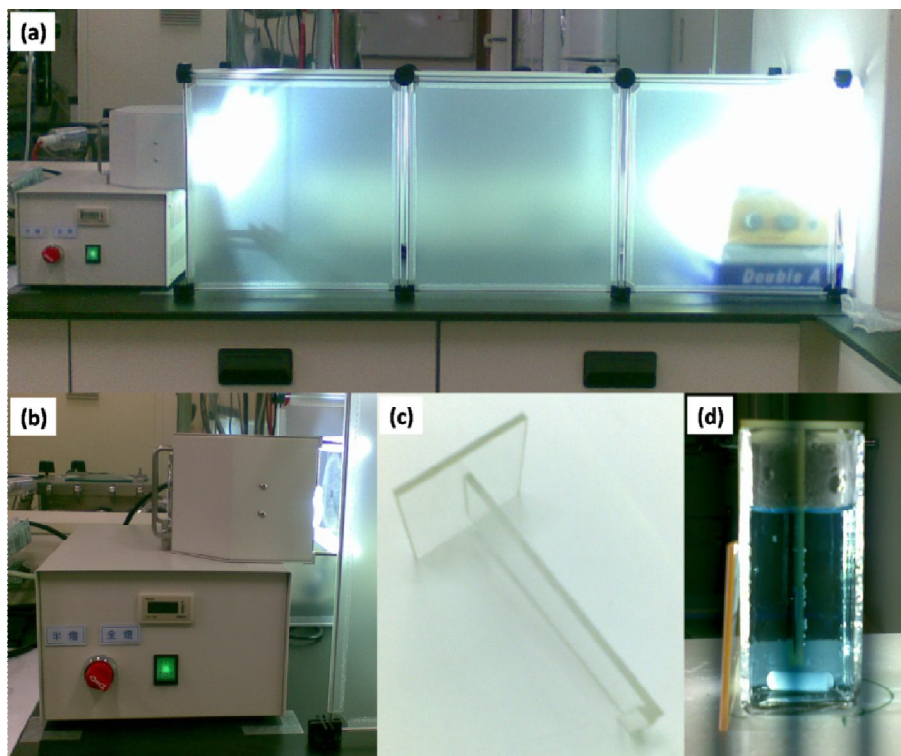


Figure 3-5 images of instruments for photocatalytic activity measurement.

Chapter 4

Growth and Field Emission of Reactive Sputtered Pd-PdO Core-shell Nanoflakes on Platinum

4.1 Growth of Pd-PdO core-shell Nanoflakes on Pt substrate

Figures 4-1(a) and (b) show the plane-view SEM images of PdO thin films reactive-sputter deposited on the Pt substrate for 15 min at 25 °C and 200 °C, respectively. For both the deposition temperatures, the PdO thin films had a flake-like morphology. The 60°-tilted SEM image of the PdO deposited at 200 °C shown in figure 4-1(c) indicates that the PdO thin film was composed of many individual fish-scale like flakes vertically standing on the substrate. While the length of the nanoflakes increased with the deposition temperature, the heights of the nanoflakes deposited at 25 °C and 200 °C were the same. PdO nanoflakes deposited at 200 °C had a width of ~15-20 nm, a length of ~250-280 nm and a height of ~200 nm.

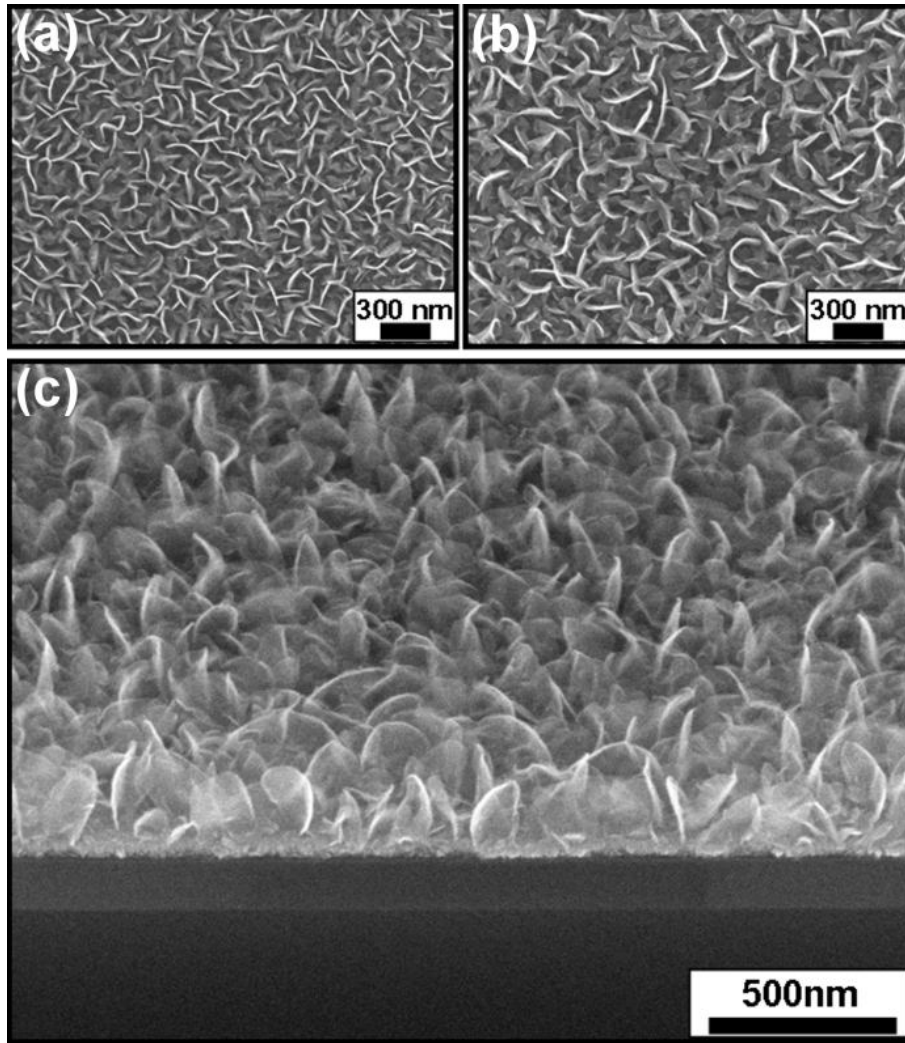


Figure 4-1. SEM images of Pd-PdO nanoflakes deposited on the Pt substrate at (a) 25 °C and (b) 200 °C. (c) 60°-tilted SEM image for nanoflakes deposited at 200 °C.

The glancing-angle X-ray diffraction (GAXRD) spectra of as-deposited nanoflake thin films are shown in figure 4-2. For the nanoflakes grown at 25 °C, four reflection peaks, corresponding to the (111), (200), (220) and (311) planes of the Pd fcc structure, were clearly observed, and a small peak situated at 33.8° was identified as the PdO(101) plane. As the growth temperature was raised to 200 °C,

while the four diffraction peaks for metallic Pd were still detected with similar intensity ratios, the peak intensity of the PdO(101) plane significantly increased and two more peaks due to the PdO(112) and (103) planes became obvious. This result indicated that the deposited nanoflakes were composed of crystalline Pd and PdO, and the PdO phase deposited at 200 °C had better crystallinity than that at 25 °C. Also shown in figure 4-2 are two Pd(3d) XPS spectra of nanoflakes deposited separately at 25 °C and 200 °C (inset). For both the two deposition temperatures, the Pd(3d_{5/2}) peak situated at ~336.9 eV, corresponding to the chemical state of PdO. No signal at 335.0 eV was detected indicating that metallic Pd was absent on the surface of the nanoflakes. Combined with the XRD results, the XPS analysis suggested that the nanoflake was capped by a PdO surface layer with a thickness probably larger than five times the inelastic mean free path of the Pd(3d) photoelectrons (~5 nm), and the PdO layer had a strong (101) texturing. TEM study further showed that a single crystalline Pd grain was encapsulated by the PdO layer.

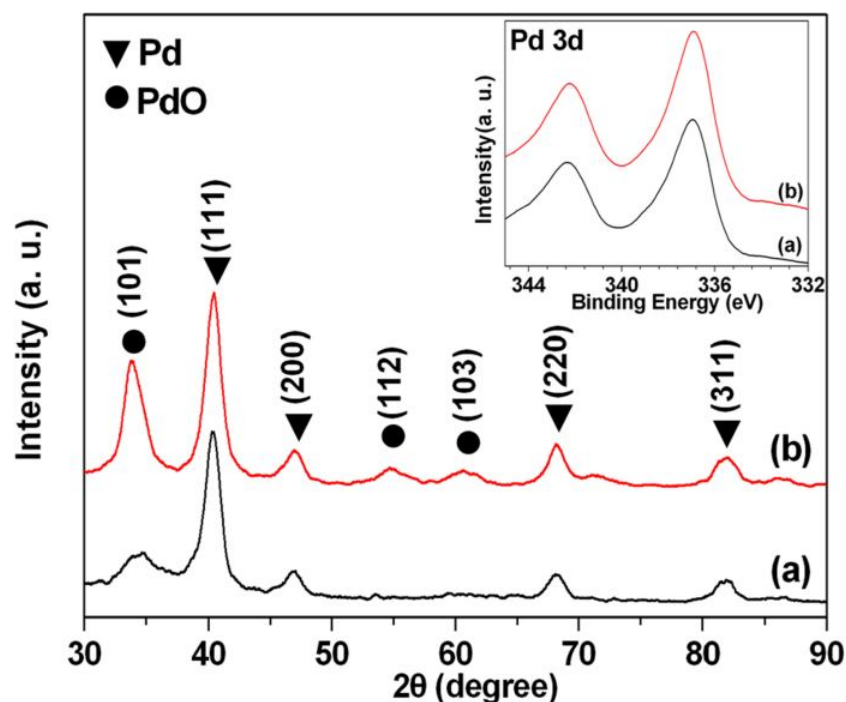


Figure 4-2. XRD spectra of Pd-PdO nanoflakes deposited on the Pt substrate at (a) 25 °C and (b) 200 °C. The inset shows the Pd(3d) XPS spectra of nanoflakes deposited at (a) 25 °C and (b) 200 °C

The TEM images of a nanoflake deposited at 200 °C is shown in figure 4-3. The nanoflake was separated from the thin film by ultrasonic agitation in ethanol. The observation of Moiré fringes in the TEM image of figure 4-3(a) indicated that different crystalline phases were present in the thin nanoflake. The inset shows the selected area electron diffraction (SAED) pattern of the nanoflake. Two sets of diffraction spots, marked separately by the solid and dashed lines, can be clearly identified from the SAED pattern, revealing that the nanoflake was composed of two single crystalline phases. Because the two diffraction sets have a symmetrical

arrangement with respect to each other, the two corresponding crystals should be epitaxially aligned with each other in the nanoflake. The diffraction set with orientation labels of $(0\bar{2}2)$, $(1\bar{1}1)$ and (200) corresponded to the Pd fcc structure with the zone axis of $[011]$ and the other set with labels of $(1\bar{1}2)$, (101) and (110) was due to the PdO tetragonal structure with the zone axis of $[\bar{1}11]$. The high resolution TEM (HRTEM) image of an edge area of the nanoflake (highlighted by the circle in figure 3(a)) is shown in figure 4-3(b). The fringe spacings of 0.269 nm and 0.218 nm corresponded to the lattice spacings of PdO(101) and (110), respectively. The fast-Fourier-transform diffraction (FFTD) pattern (inset of figure 3(b)) of the area marked by the square in the HRTEM image indicated a single crystalline phase in the edge area of the nanoflake. The TEM analysis clearly demonstrated that the nanoflake had an epitaxial core-shell structure with a Pd single crystalline grain surrounded by the PdO surface layer.

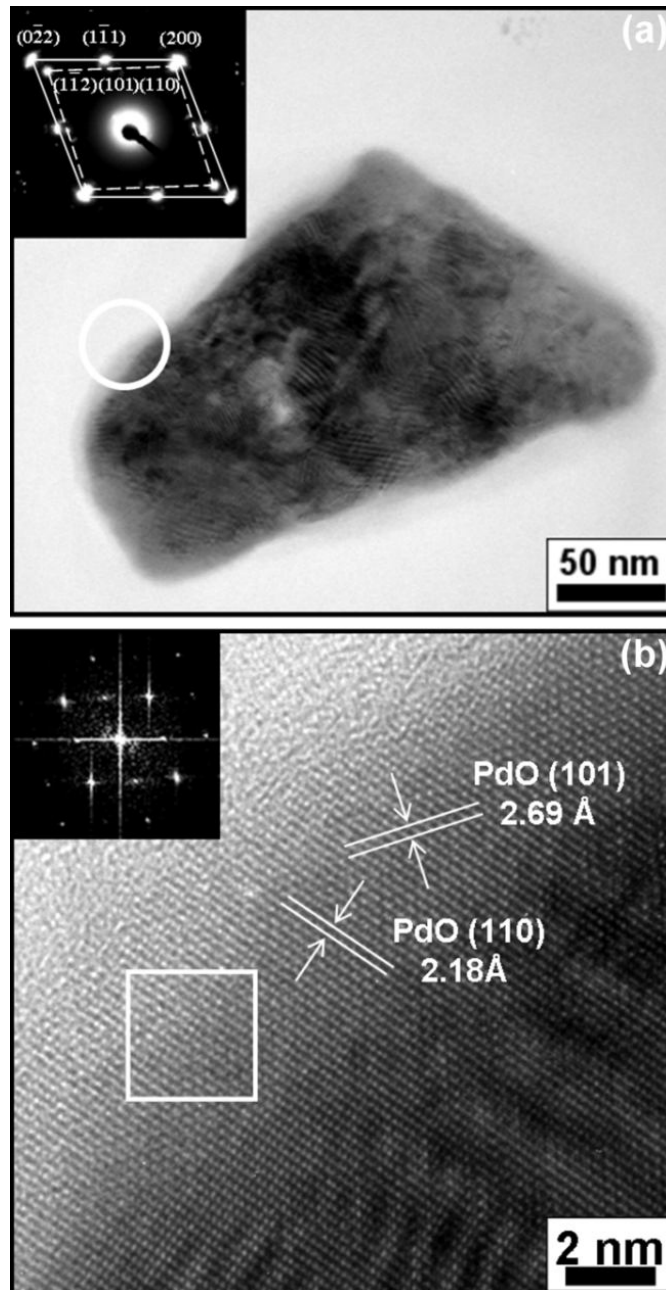


Figure 4-3. (a) TEM image of a Pd-PdO nanoflake separated from the nanoflake thin film deposited at 200 °C for 15 min. The inset is the SAED pattern of the nanoflake. Two diffraction sets are identified to correspond to the Pd fcc structure (solid line) and the PdO tetragonal structure (dashed line). (b) The HRTEM image of the edge area marked by circle in (a). The inset shows the FFTD pattern of the area marked by square in (b).

4.2 Growth and core-shell mechanism of PdO Nanoflakes

To explore the growth mechanism of the Pd-PdO nanoflakes, we have grown nanoflakes for various deposition times. The SEM images of figure 4-4 show variation in surface morphology of the nanoflake thin film deposited at 25 °C as a function of the deposition time. The thin film deposited for 2 min had a very smooth surface (figure 4-4(a)). Islands began to emerge on the film surface after 3 min deposition, and a few islands already exhibited flake-like feature (figure 4-4(b)). The flakes grew larger both in length and height with increasing the deposition time as shown by Figs. 4-4(c) and 4-4(d). The observation implied that the nanoflakes were not directly formed on the substrate via the Volmer-Weber growth mode, but rather evolved due to a certain driving force developing in the early stage of the film deposition. The XPS spectrum of the smooth thin film deposited for 2 min is shown in figure 4-5. A close examination of the Pd(3d) peaks indicated that, within the probe depth of the XPS measurement, PdO was the only chemical state of Pd. Because Pt(4f) photoelectrons from the substrate was also detected, the presence of metallic Pd in the thin film could be ruled out. Thus the XPS analysis suggested that PdO was the primitive product at the beginning of the reactive-sputter deposition, and very likely the precursor for the formation of the crystalline Pd grain in the nanoflake.

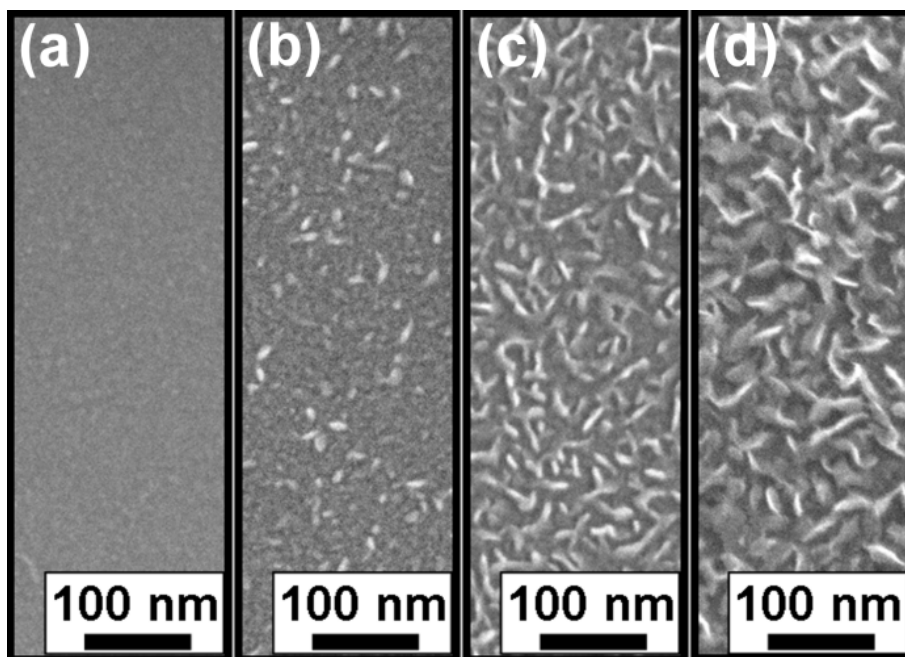


Figure 4-4 SEM images of Pd-PdO nanoflakes deposited on the Pt substrate at 25 °C for (a) 2 min, (b) 3 min, (c) 4 min and (d) 5 min.

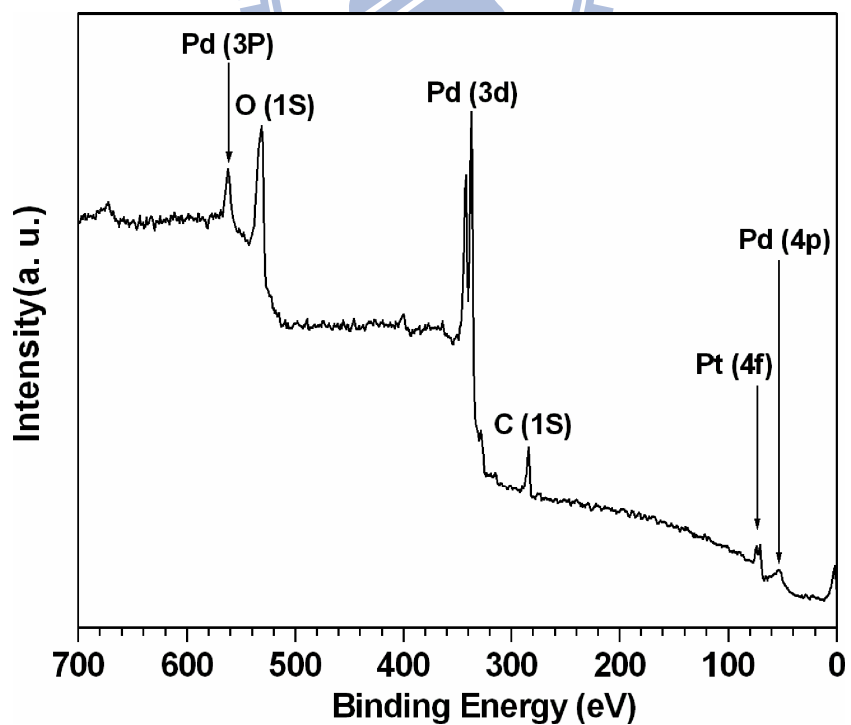


Figure 4-5 XPS survey spectra for 2 min deposition at a substrate temperature of 25 °C.

In order to study the role of the Pt substrate in the growth of the Pd-PdO core-shell nanoflakes, we have also reactive-sputter deposited PdO at 200 °C on a sputter-deposited Ti and a thermally grown SiO₂ thin film for comparison. Nanoflakes with a geometric shape like that shown in figure 4-1 were also produced on both the thin film substrates. According to XRD and XPS analyses, PdO was the only chemical composition of the nanoflakes deposited on the Ti and SiO₂ substrates. In addition, TEM analysis showed that the PdO nanoflake was a single crystalline grain (not shown). Based on simple surface energy consideration, formation of the crystalline PdO nanoflake rather than a spherical structure suggested that the growth of the PdO nanoflake was via an anisotropic process. The anisotropic growth process might be related to the planar coordination arrangement of Pd and oxygen atoms in the PdO crystal lattice, in which each Pd atom is coordinated with four oxygen atoms. Because the nanoflake grown on the SiO₂ and Ti surfaces was composed of only the crystalline PdO phase, the Pt surface must play a critical role in the formation of Pd-PdO core-shell nanoflakes on the Pt substrate. The observation that the core-shell nanoflake grown on the Pt substrate has the same geometric shape as the crystalline PdO nanoflake grown on the SiO₂ and Ti substrates seemed to suggest that PdO was first deposited on the Pt substrate, followed by formation of the

crystalline Pd core sheet with a shape compliant with that of the PdO nanoflake.

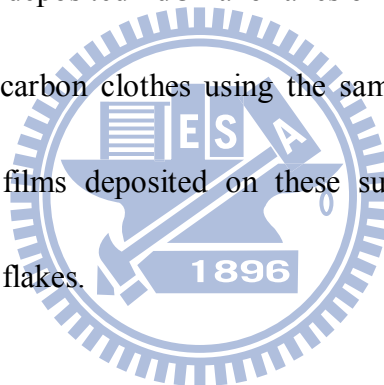
This suggestion is in agreement with the discussion about Figs. 4-4 and 4-5.

PdO has a crystal structure of tetragonal cooperite structure with the lattice constants: $a = b = 3.0434 \text{ \AA}$ and $c = 5.3363 \text{ \AA}$. [31] On the other hand, the Pt fcc structure has a lattice constants $a = b = c = 3.924 \text{ \AA}$, which are very close to the lattice constants of the Pd fcc structure ($a = b = c = 3.891 \text{ \AA}$). As the PdO film grew thicker, the interfacial stress between the PdO deposit and the Pt substrate became so large, due to the large lattice mismatch, that decomposition of the PdO phase and lattice reconstruction could be initiated at the interface. Furthermore, the negligible difference in the lattice parameters between the Pd and Pt lattices (0.8%) could facilitate nucleation of the Pd crystal on the Pt substrate during the initial stage of the phase transformation. The lattice mismatch between the PdO and Pd lattices was very large as well, thereby a large interfacial stress always existed at the PdO-Pd interface. Therefore, the phase transformation from PdO into Pd must progressively proceed at the interface between the growing Pd crystal and the PdO surface layer, which was continuously deposited on the nanoflake during the reactive sputter deposition. The continuous stress building up between the Pd core sheet and the PdO surface layer would limit the thickness of the PdO layer deposited on the nanoflake. According to the XPS and HRTEM analyses, the PdO surface layer was

probably ~4-6 nm in thickness. Because the thickness of the nanoflake was ~15-20 nm as discussed above, the Pd core sheet in the nanoflake must be just a few nm in thickness. From the SAED diffraction pattern shown in figure 3(a), the PdO surface layer was epitaxially aligned with the Pd crystal. It has been reported previously that the PdO(110) plane was epitaxially aligned with the Pd(200) plane when Pd particles supported on SiO₂ were oxidized in oxygen.[33] The same epitaxial arrangement was also observed in this study. The lattice spacing of the PdO(110) and the Pd(200) planes are 2.11 Å and 1.95 Å, respectively. Compared with other lattice planes of the two crystal structures, these two planes have the smallest difference in the lattice spacing, and are more likely to be epitaxially arranged with each other. Within this thickness range of the PdO surface layer, the epitaxial arrangement of the Pd-PdO core-shell structure seemed to be relatively stable.

The observation of the growth of single-crystalline PdO nanoflakes on the SiO₂ substrate is very different from what we found in a recent study on PdO deposition on the Pt substrate. Pd-PdO core-shell nanoflakes can be grown on the Pt substrate under the same reactive sputter deposition condition as this study.[65] We ascribed the formation of the Pd-PdO core-shell structure to lattice mismatch at the interface between the PdO surface layer and the Pt substrate. PdO has a tetragonal cooperite structure with the lattice constants significantly different from those of the Pt and the

Pd fcc lattice structures. When the deposited PdO layer becomes thicker, the large interfacial stress due to the lattice mismatch will initiate PdO decomposition and phase transformation into metallic Pd at the interface. In this study, because the SiO₂ substrate is amorphous, the interfacial stress due to lattice mismatch is greatly relaxed at the interface between the deposited PdO nanoflake and the SiO₂ substrate. Therefore, PdO decomposition and phase transformation do not take place during the anisotropic growth of the PdO nanoflake, and thus single-crystalline PdO nanoflakes are formed. We have also deposited PdO nanoflakes on different kinds of substrates, including TiO₂, glass and carbon clothes using the same deposition condition, and found that the PdO thin films deposited on these substrates comprised of only single-crystalline PdO nanoflakes.



4.3 Field Emission Characteristics of PdO Nanoflakes

PdO is a semiconductor and, therefore, not an ideal field emission material in respect to its relatively high electrical resistivity. However, the metallic Pd core sheet can increase the conductivity of the Pd-PdO core-shell nanoflake as a whole, thereby may improve the field emission efficiency. Moreover, because the nanoflakes vertically standing on the substrate had a sharp top edge and a high aspect ratio in terms of the thickness and height, they are expected to have good field

emission properties. Figure 4-6 shows the field emission current density–applied field (J-E) curves of the PdO nanoflakes deposited for 15 min at 25 °C and 200 °C. According to the J-E curve, nanoflakes deposited at 200 °C had a much better field emission performance than that deposited at 25 °C. At the applied field of 11 V μm^{-1} , nanoflakes deposited at 200 °C and 25 °C had a field emission current density of 30.7 $\mu\text{A cm}^{-2}$ and 4 nA cm^{-2} , respectively. The linear Fowler-Nordheim (F-N) plots shown in the inset of figure 4-6 indicated that the field-emission followed the Fowler-Nordheim field emission mechanism. The turn-on field of the nanoflakes deposited at 25 °C and 200 °C was determined to be 10 and 6 V μm^{-1} , respectively. The turn-on field was herein defined as the field at the intersection of the two straight lines extrapolated separately from the linear rising segment and the background of the F-N plot. The better field emission characteristics of the nanoflake deposited at 200 °C may be attributed to that the PdO surface layer on the nanoflake deposited at 200 °C had a well textured and better crystalline structure than that deposited at 25 °C. According to the F-N theory,[66] the field enhancement factor (β), which is strongly dependent on the geometric structure of the field emitter, can be approximated by

$$\beta = -\frac{B\phi^{3/2}}{S} \quad (1)$$

where $B = 6.83 \times 10^3$ ($\text{VeV}^{-3/2} \mu\text{m}^{-1}$), ϕ is the work function of the emitter and S is the slope of the F-N plot. The F-N plot slope of the nanoflake deposited at 200 °C was

-108.3. The β values of the nonflake was thus determined to be 791, assuming a work function of 5.4 eV for PdO [26]. The β value of Pd-PdO nanoflakes is comparable to that of Co_3O_4 nanowalls [67] and some previously reported one-dimensional nanoemitters, such as carbon nanotubes and Si nanotips [68-69]. Due to the desirable field emission characteristics, combined with easy preparation method and chemical and thermal stabilities, the Pd-PdO nanoflakes can be considered as a potential emitter for field emission applications.

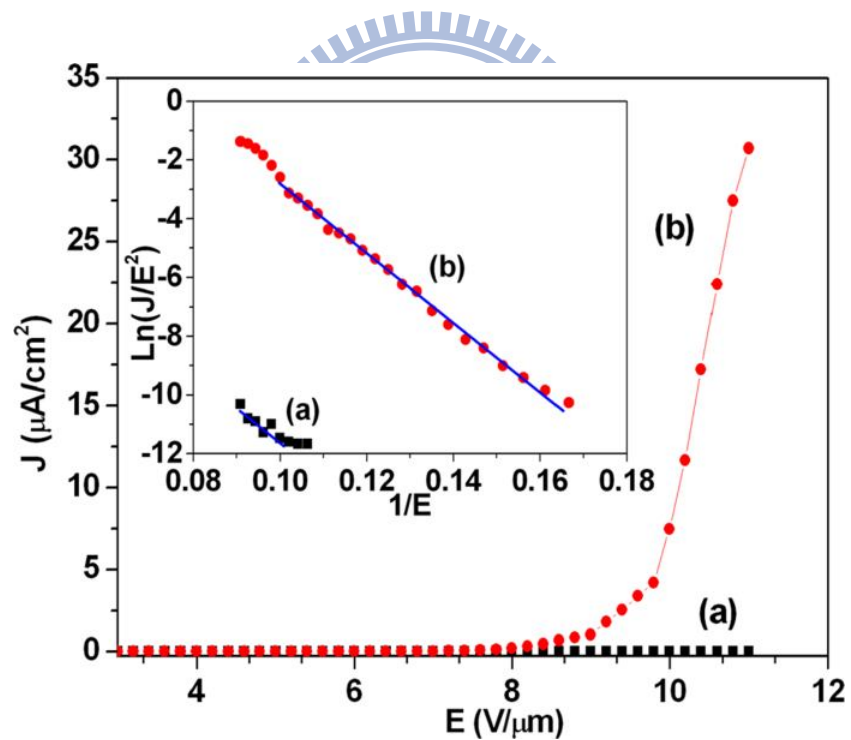


Figure 4-6. Field emission J-E curves of Pd-PdO nanoflakes deposited on the Pt substrate at (a) 25 °C and (b) 200 °C. The corresponding F-N plots of the J-E curves (a) and (b) are shown in the inset.

4.4 Summary

In summary, we have deposited PdO on the Pt substrate by reactive sputter deposition. At temperatures at 200 °C and below, the PdO thin film grown on the Pt substrate had a flake-like morphology. TEM, XRD and XPS studies revealed that the nanoflake had a core-shell structure with a single Pd grain encapsulated by a crystalline PdO surface layer. The PdO layer was about 4-6 nm in thickness and epitaxially aligned with the Pd lattice. Formation of the Pd-PdO nanoflakes resulted from the large interfacial stress due to the large lattice mismatch between the PdO surface layer and the Pt substrate. The Pd grain growth in the nanoflake was facilitated by the close similarity in the lattice parameters of the Pt and Pd fcc crystal structures. Because of the sharp top edge and a high aspect ratio, the Pd-PdO nanoflake exhibited a field emission efficiency comparable to many 1-D nanoemitters. A β value of 791 was obtained for the nanoflake deposited at 200 °C.

Chapter 5

Growth and Photoresponse Study of PdO Nanoflakes Reactive-sputter Deposited on SiO₂

5.1 Growth of PdO Nanoflakes on SiO₂ substrate

PdO thin films reactive-sputter deposited on the SiO₂ substrate at temperatures below 250°C has a flake-like morphology. Figure 5-1(a) shows a plane-view SEM image of a PdO thin film deposited at 25°C for 15 min, and the corresponding 60°-tilted SEM image is shown in figure 5-1(b). The as-deposited PdO thin film is composed of interconnected bowed flakes standing on the SiO₂ substrate. The flakes have a thickness of ~10-15 nm, a length of ~145-175 nm and a height of ~200 nm. When annealed in air at 200°C for 2 h, the nanoflakes change little in size. For the PdO thin film annealed at 400°C, the thickness and length of the nanoflakes increase to ~15-20 nm and ~180-225 nm, respectively. Figures 5-1(c) and (d) show the SEM images of the 400°C-annealed PdO thin film. According to XPS analysis, the nanoflake thin films are comprised of PdO. The XPS survey spectrum of the as-deposited nanoflake thin film (figure5-2(a)) clearly shows that Pd and oxygen are the two primary surface elements. The peaks denoted by asterisk symbols are due to an ultrathin Pt film which was sputter-deposited on the nanoflake thin film for energy

calibration; the C(1s) peak is likely due to inadvertent surface contaminants. The Pd(3d) XPS spectra of the as-deposited, 200°C-annealed and 400°C-annealed PdO nanoflake thin films are shown in figure5-2(b). For all the three PdO nanoflake thin films, the Pd(3d_{5/2}) peak situated at 336.9 eV corresponds to the chemical state of PdO. The absence of the signal at 335.0 eV indicates that no metallic Pd phase is present in the PdO nanoflake thin films.

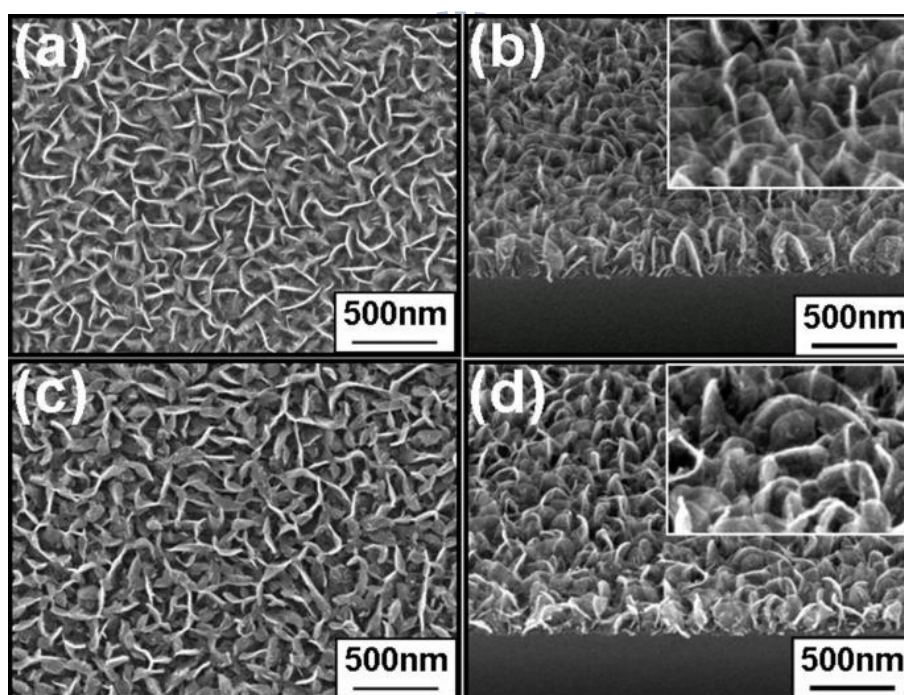


Figure 5-1 (a) Plane-view and (b) 60°-tilted SEM images of the as-deposited PdO nanoflake thin film, respectively; (c) Plane-view and (d) 60°-tilted SEM images of the 400°C-annealed nanoflake thin film, respectively. The insets in (b) and (d) are the corresponding enlarged SEM images.

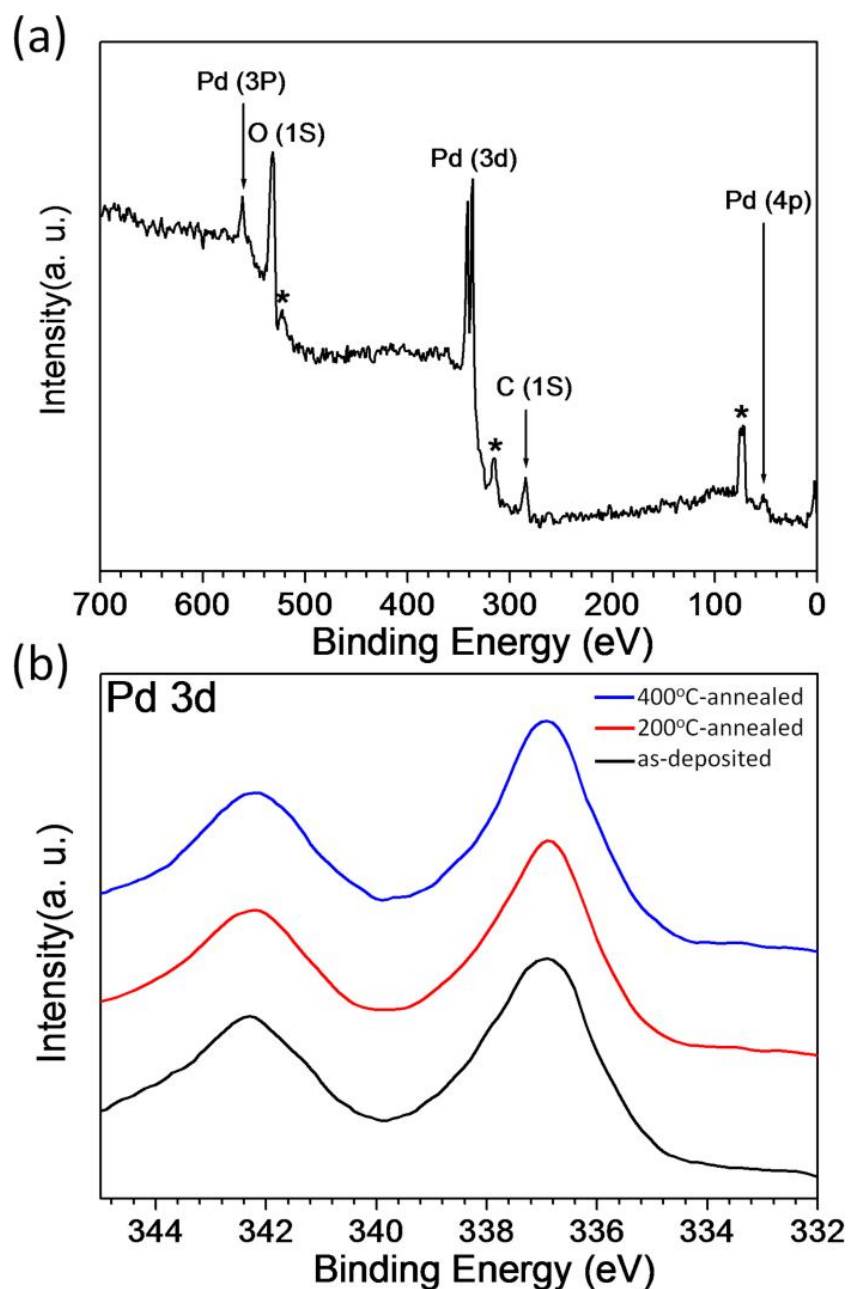


Figure 5-2 (a) XPS survey spectra for the as-deposited PdO nanoflake thin film; the peaks denoted by asterisk symbols are due to the ultrathin Pt film for energy calibration; (b) Pd (3d) XPS spectra of the 25°C-deposited, the 200°C-annealed and the 400°C-annealed nanoflake thin films.

Figure 5-3 shows glancing-angle XRD spectra of the as-deposited, the 200°C-annealed and the 400°C-annealed PdO thin films. For the as-deposited nanoflake thin film, the diffraction peak due to the (101) plane of the PdO tetragonal lattice is broad and weak, suggesting the presence of a poorly crystalline structure. After annealed at 200°C in air for 2 h, the PdO thin film is preferentially oriented in the (112) plane, while the (101) peak becomes less definite in shape. When the annealing temperature is increased to 400°C, diffraction peaks due to the (110), (103) and (202) planes are clearly detected and the (101) peak grows into the strongest peak. The XRD analysis indicates that the nanoflake thin film is well-crystallized after the 400°C anneal.



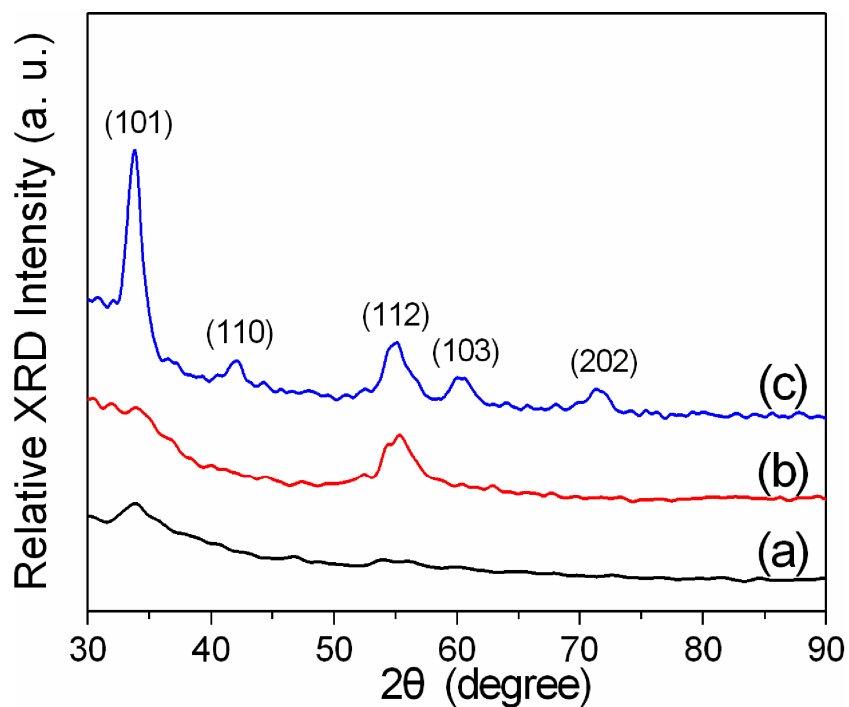


Figure 5-3 XRD spectra of the PdO thin films: (a) 25°C-deposited nanoflake thin film, (b) 200°C-annealed nanoflake thin film and (c) 400°C-annealed nanoflake thin film.

Figure 5-4(a) shows a bright-field (BF) TEM image of a nanoflake, which was separated from the 400°C-annealed nanoflake thin film by ultrasonic agitation in ethanol. The high resolution TEM (HRTEM) image of an edge area of the nanoflake, highlighted by the circle in the BFTEM image, is shown in figure 5-4(b). The lattice fringes with a lattice spacings of 0.211 nm and 0.298 nm correspond to the PdO(110) and (100) planes, respectively. From the BFTEM image, there are alternating dark and bright bands extending from the left to the right of the nanoflake, suggesting that they are bend contours as a result of the bowed shape of the nanoflake as shown by

the SEM images in Fig 5-1. Also shown in the BFTEM image are many nano-sized bright and dark spots randomly distributing on the nanoflake. The contrast pattern of these spots changes when the nanoflake specimen is slightly tilted from the [001] zone axis. The appearance of these spots results from the epitaxial growth of PdO nanograins on the bowed nanoflake according to HRTEM analysis as shown in figure 5-5. A selected area electron diffraction (SAED) pattern of the nanoflake is shown in the inset of figure 5-4(a). The diffraction spots labeled by $(1\bar{1}0)$, (100) and (110) are due to corresponding lattice planes of the PdO tetragonal structure with the zone axis of [001]. The distinct SAED pattern suggests that the nanoflake is one single-crystalline PdO grain without any microstructure phase other than the PdO lattice.

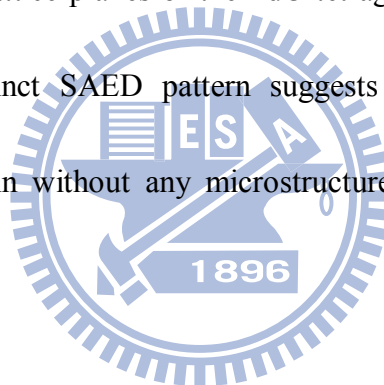


Figure 5-5(a) shows the HRTEM image of a selected area on a PdO nanoflake. Squared nanograins distribute over the bowed nanoflake and, according to the lattice spacing measurement and the fast Fourier transform (FFT) analysis, these nanograins have a PdO tetragonal lattice structure. Figure 5-5(b) shows the inverse FFT image of a nanograin in the (010) plane. The inverse FFT image clearly shows that the nanograin seems to grow epitaxially on the nanoflake, but the nanograin and its adjacent area are rich in dislocations.

The 200 °C-annealed nanoflake thin film also has a SAED pattern corresponding

to the PdO lattice structure, but the intensity of the diffraction spots is much weaker than that of the 400°C-annealed nanoflake thin film. Moreover, the 200 °C-annealed nanoflake is unstable under electron beam irradiation. During the SAED analysis, the intensity of the diffraction spots decreased with time. Deformation in the shape of the nanoflake was perceivable during the TEM analysis. The shape deformation became much more severe when HRTEM analysis was performed. The 200°C-annealed nanoflake seemed to be totally melted down within 20 sec under the focused electron beam irradiation. We suspect that the unstable microstructure is likely due to the presence of defects, such as oxygen vacancy, which leads to the disintegration of the PdO crystal upon the electron irradiation. The poorly defined XRD spectrum of the 200°C-annealed nanoflake thin film shown in figure 5-3 is very likely results from the defective microstructure.

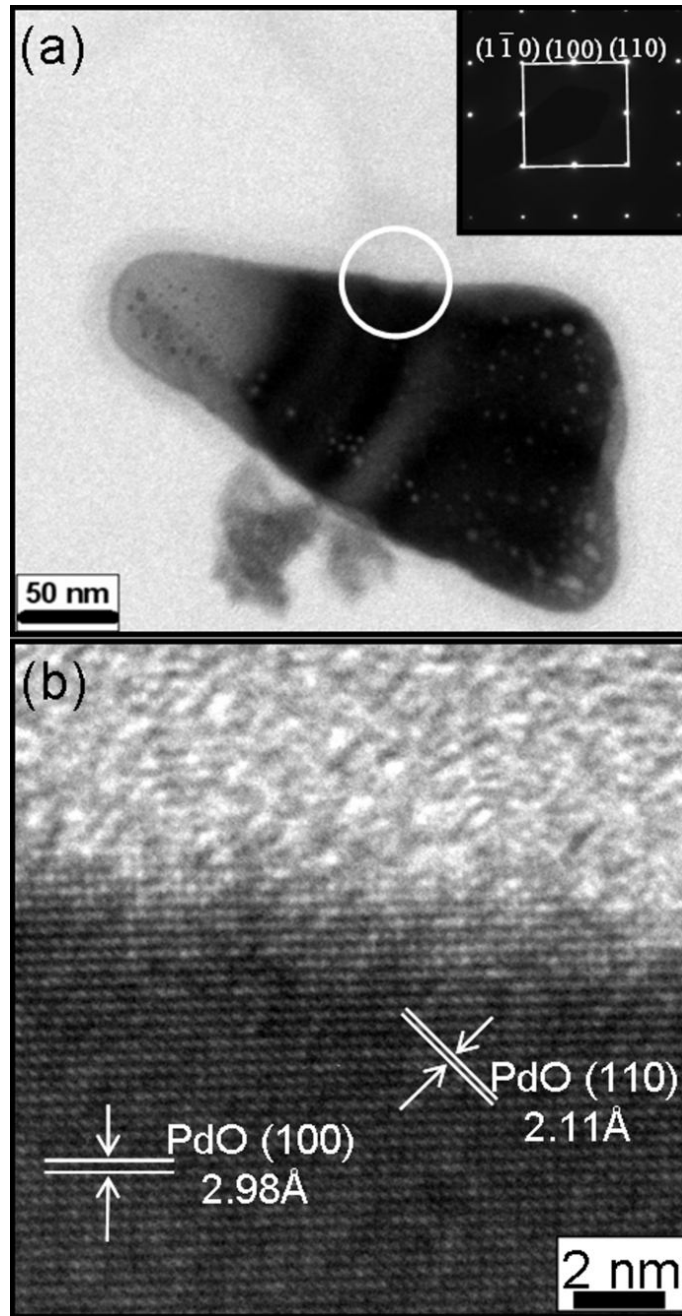


Figure 5-4 (a) BFTEM image of a PdO nanoflake separated from the 400°C-annealed nanoflake thin film and the corresponding SAED pattern (inset); (b) HRTEM image of a top-edge area marked by the circle in (a).

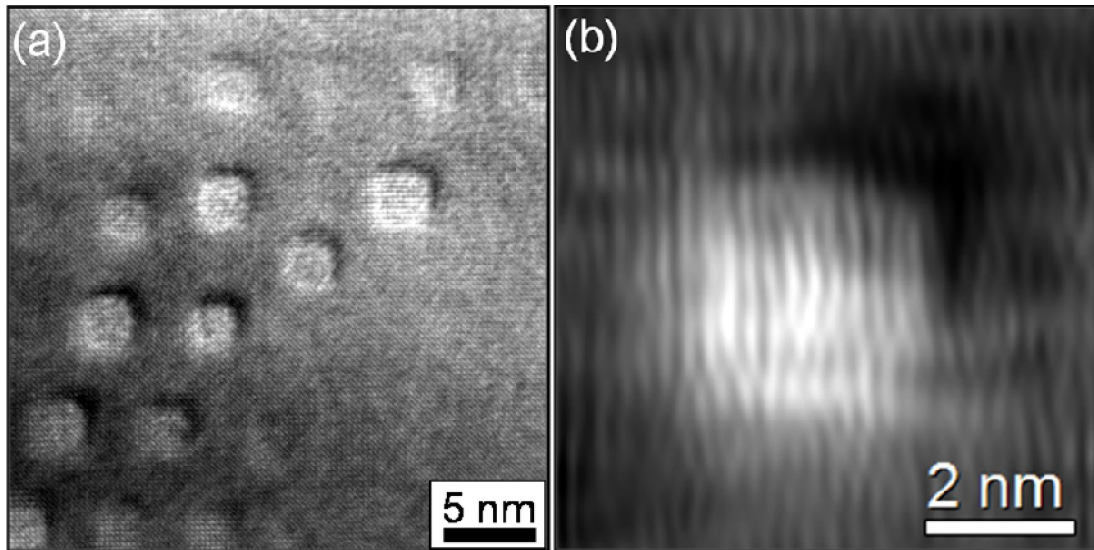


Figure 5-5(a) HRTEM image of a selected area on the nanoflake shown in the inset; (b) inverse fast Fourier transform image of a nanograin in the (010) plane.

5.2 Bandgap Energy of PdO nanoflakes

The bandgap of PdO has a wide reported range from 0.8 to 2.2 eV, depending on crystallinity and purity [14, 19, 27]. To determine the bandgap energy of the nanoflake PdO thin film, diffuse reflectance UV-vis spectroscopy was used. UV-vis spectra of the as-deposited (at 25°C), the 200°C-annealed and the 400°C-annealed PdO nanoflake thin films are shown in figure 5-6(a). The 400°C-annealed thin film has an absorption maximum at ~620 nm, and the as-deposited and the 200°C-annealed thin films have similar absorption features, having a broad absorption band with two maxima at ~632 nm and ~652 nm. The optical absorbance (F) can be correlated with the reflectance (R) via the Kubelka–Munk (KM) function[70]

$$F(R) = \frac{(1-R)^2}{2R} \quad (1)$$

The KM function is often used to evaluate the bandgap of a semiconductor material in terms of the Tauc plot[71], which is constructed by plotting the KM function, in the form of $(F(R \times hv))^n$, versus hv , where h is the Planck constant, v is the absorption frequency and $n = 1/2$ for a direct bandgap semiconductor. By extrapolating the linear Tauc regime above the absorption edge to the hv axis (as shown in figure 5-6(b)), one can determine the bandgap energy of the PdO nanoflake thin film, which is a direct bandgap semiconductor.[29] The determined bandgap energies of the as-deposited, the 200°C- and the 400°C-annealed PdO nanoflake thin films are ~1.90, ~1.96 and ~2.06 eV, respectively. Electron-hole pairs can be generated upon illumination with photon energies larger than the bandgap energy of a semiconductor. Therefore, the low direct bandgap energy makes the PdO nanoflake thin film a good photoconductor under visible and UV illumination.

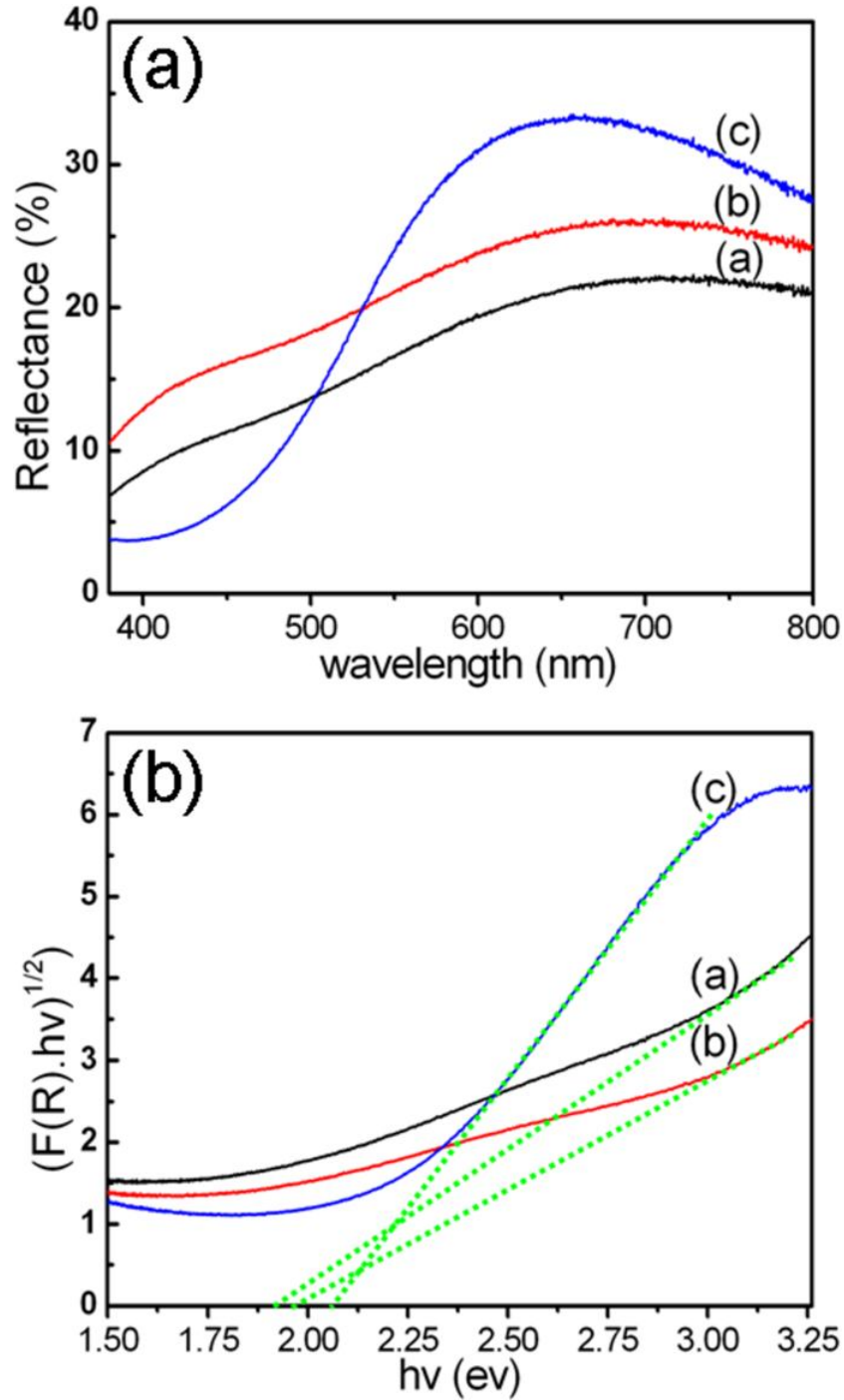


Figure 5-6 (a) Diffusion reflectance spectra of the reactive-sputtered PdO thin films, and (b) Tauc plots constructed from (a); curves a, b and c represent the UV-vis spectra and the Tauc plots of the as-deposited, the 200°C-annealed and the 400°C-annealed nanoflake thin films, respectively.

5.3 Photoresponse of PdO nanoflakes

The crystallinity strongly affects photoresponse characteristics of the reactive-sputtered PdO thin films. Figure 5-7 shows photoresponse profiles of the PdO thin films under the UV illumination at 365 nm as a function of the illumination time. The photoresponse measurement configuration, as shown in the inset, has two Ag paste electrodes placed 1 cm apart on the PdO thin film stripe. The photocurrent was measured at a bias of 3 V and the UV light was periodically switched on and off at a power density of 21 mW/cm². For the 400°C-annealed PdO thin film, the photocurrent density, which is defined herein as the current density difference between with and without the UV illumination, promptly reaches the maximum value of 145 μA/cm². However, the photoresponse of the as-deposited nanoflake thin film is not perceivable under the measurement condition (not shown in figure 5-7), and the 200°C-annealed thin film responses weakly to the UV exposure with a photocurrent density smaller than ~5 μA/cm². The much more sensitive photoresponse of the 400°C-annealed nanoflake thin film can be ascribed to the better crystallinity. Photoconductors of better crystallinity usually demonstrate a better photoconductivity because less defects are present in the crystal, which may act as recombination centers and traps degrading the photoresponse performance [72-73]. The high dark current density (275 μA/cm²) of the 400°C-annealed nanoflake thin film indicates a relatively

low film resistance ($\sim 10\text{ K}\Omega$) due to the good crystallinity. On the other hand, the 200°C -annealed nanoflake thin film has a low electrical conductivity due to the poor crystallinity, resulting in a much smaller dark current density. The low electrical conductivity hampers carrier transport leading to a much smaller photocurrent density.

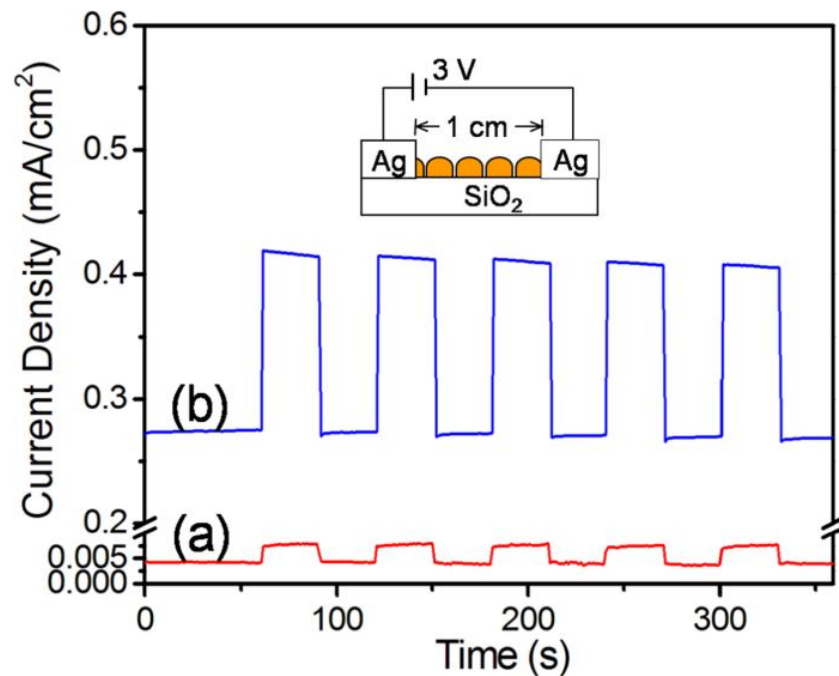


Figure 5-7 Photocurrent density of the PdO thin films under the periodic UV exposure at 365 nm as a function of the photoresponse measurement time: (a) the 200°C -annealed nanoflake thin film and (b) the 400°C -annealed nanoflake thin film. Photoresponse profiles a and b were obtained at a bias of 3 V with the photocurrent measurement configuration shown in the inset.

The photocurrent density of the 400°C-annealed PdO thin film declines slightly during each UV illumination cycle of 30 sec as shown in figure 5-7. Figure 5-8 shows the photocurrent density (PD)-time profile of the nanoflake thin films under the UV illumination for 30 min. The photocurrent density of the 400°C-annealed thin film gradually decreases to $\sim 135 \mu\text{A}/\text{cm}^2$ after the UV illumination of 5 min. The decrease in the photocurrent density ($\sim 10 \mu\text{A}/\text{cm}^2$) probably results from a decrease in the surface coverage of O_2^- anions on nanoflakes as will be discussed later. After the gradual decrease in the first 5 min, the photocurrent density becomes to steadily increase till the UV light source is switched off. The steady increase is not a consequence of the UV illumination. When the electrical measurement is carried out in dark, the measured current steadily increased with time (up to 30 min) as well. Therefore, the steady photocurrent increase observed in the PD-Time profile is a result of superimposition of the increasing dark current and the photogenerated current. Because the dark current slightly decreases when the measurement is performed in vacuum, we suspect that the dark current increase is due to an ambient gas (other than oxygen) adsorption during the electrical measurement. A study on the dark current variation as a function of gas adsorption is being undertaken.

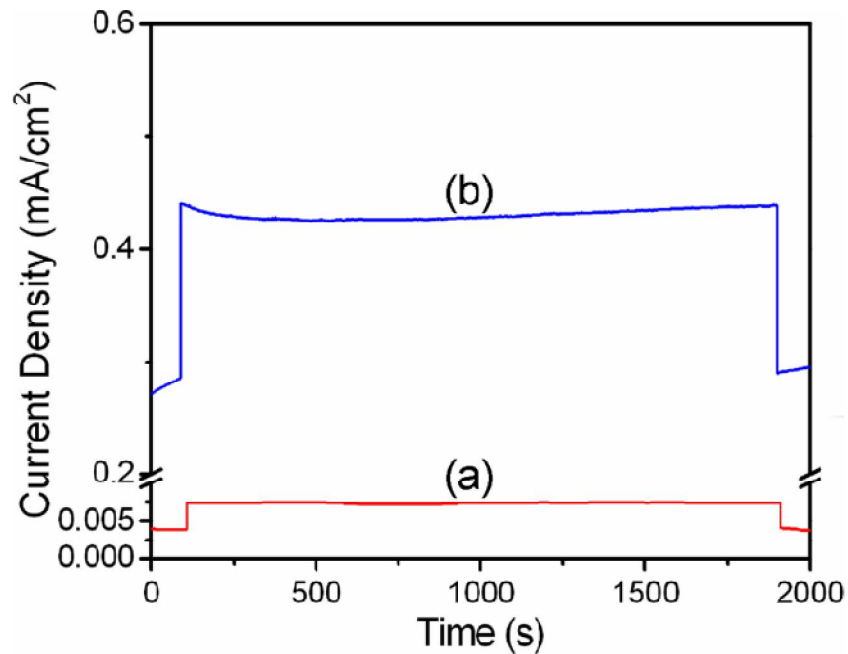


Figure 5-8 Photocurrent density-time profiles : (a) the 200°C-annealed nanoflake thin film and (b) the 400°C-annealed nanoflake thin film.

5.4 Effect of oxygen adsorption in photoresponse

In the framework of the oxygen ionosorption model, it is asserted that O_2^- anions chemisorbed on n-type semiconductor oxides, such as ZnO and TiO_2 , form a low-conductivity depletion layer near the surface.[74-75] Upon UV illumination, photogenerated holes migrate to the surface and discharge O_2^- anions leading to desorption of O_2 from the surface, resulting in an improvement of the photoconductivity of n-type semiconductor oxides.[39-40, 76] Opposite to ZnO and TiO_2 , PdO is a p-type semiconductor and, therefore, the presence of surface O_2^- anions will lead to an increase in the majority carrier concentration near the surface.

It has been reported that p-type semiconductor oxides are more liable to O_2^- anion adsorption than n-type ones.[77] Figure 5-9 shows O(1s) XPS spectra of the nanoflake thin film. Because various types of oxygen species, such as O_2^- , O^- , OH^- and H_2O , may be concurrently present on the PdO surface, and the Pd($3d_{3/2}$) peak also falls in the O(1s) energy window, it is very difficult to properly resolve every chemical component from the O(1s) spectra by curve fitting. Thus, we labeled O(1s) binding energies compiled from previous reports in the figure to indicate surface species likely present within the binding energy range.[17, 78-80] The O(1s) binding energy of O_2^- anions adsorbed on SnO_2 has been reported to be situated at 534.5 eV [78]. All the XPS spectra in figure 5-9 clearly show a large portion of signal extending to the high energy regime (>534.5 eV), and we tend to believe that O_2^- anions are present on the PdO thin films. The presence of O_2^- anions on the p-type PdO surface can create an accumulation layer near the oxide surface due to electron transfer from the PdO surface to adsorbed oxygen molecules, resulting in an increase in the surface conductivity of the thin film. Upon the UV illumination, O_2^- surface anions may give away electrons to the p-type oxide, which recombine with excess majority carriers generated by the photoexcitation, followed by O_2 desorption from the surface. The reduction in the hole concentration will decrease the

conductivity of the nanoflake thin film and thus the measured photocurrent decreases accordingly.

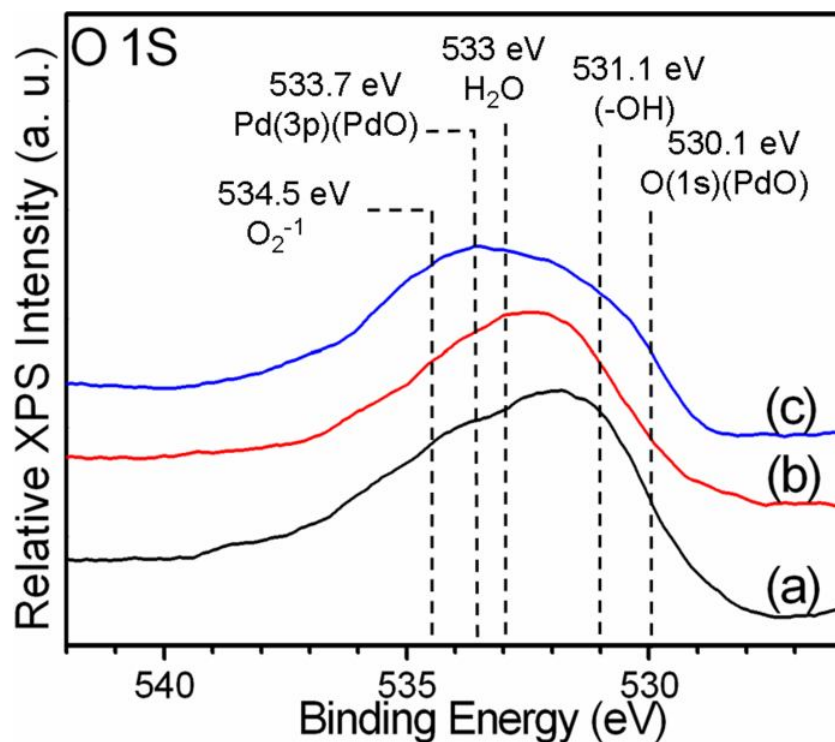


Figure 5-9 O 1s XPS spectra of the PdO nanoflake thin film: (a) the as-deposited, (b) the 200°C-annealed and (c) the 400°C-annealed nanoflake thin films. The labeled binding energies of the O 1s electron of various oxygen containing species and the Pd 3p_{3/2} electron are summarized from refs. [17, 78-80]. The XPS spectra were calibrated with the binding energy of the Pt(4f_{7/2}) electron.

5.5 Summary

PdO nanoflakes were also grown on the SiO₂ surface at the room temperature. After annealed at 400°C, the PdO nanoflake has a single crystalline structure according to TEM and XRD studies. The well-crystalline 400°C-annealed nanoflake thin film has a bandgap energy in the red-light range (~2.06 eV), and exhibits a very sensitive photoresponse upon the UV (365 nm) illumination. However, the as-deposited and the 200°C annealed thin films, which are poorly crystallized, respond weakly to the UV light exposure. The high photoresponse sensitivity of the 400°C-annealed nanoflake thin film is ascribed to a lower density of recombination centers and traps due to the excellent crystallinity of the nanoflakes and a high carrier extraction efficiency due to the low electrical resistivity. Adsorption of O₂⁻ anion is suggested to be a likely cause inducing the slight decrease in the photocurrent density of the 400°C-annealed nanoflake thin film during the initial stage of the UV illumination. This study indicates that the high-temperature annealed PdO nanoflake thin film has desirable characteristics for applications demanding sensitive photoresponse, such as photodetectors and photoswitches.

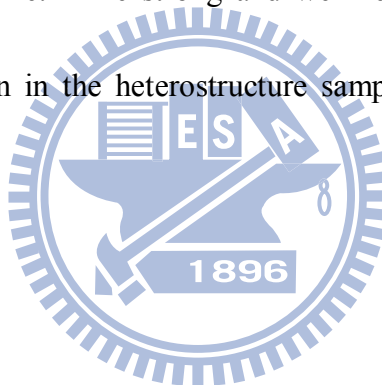
Chapter 6

Heterostructure of PdO Nanoflakes and TiO₂ Nanoparticles in Photocatalytic Application

6.1 Characterization of PdO/TiO₂ heterostructures

Figure 6-1 shows SEM images of the P-25 TiO₂ sample and the PdO/TiO₂ heterostructures prepared with different PdO deposition times and annealed at 400°C for 2 h. After the spinning deposition, P-25 TiO₂ nanoparticles are well dispersed on the SiO₂ substrate as shown in figure 6-1(a). The uniform dispersion of P-25 nanoparticles on the substrate ensures a constant P-25 loading for the subsequent preparation of different PdO/TiO₂ heterostructure samples. After 1 min PdO deposition, the TiO₂-PdO-1 sample shows little change in the surface morphology compared with the bare P-25 sample (figure 6-1(b)). This is because that deposited PdO grains, which is around 2-3 nm in size as revealed by TEM analysis, is too small to be perceived in the SEM image. According to figure 6-1(c), many islands present on the TiO₂-PdO-3 sample exhibit flake-like feature, indicating that PdO nanoflakes begin to grow on the sample surface at the deposition time of 3 min. The density and the size of PdO nanoflakes increase with the deposition time. The surface of the two samples, TiO₂-PdO-8 and TiO₂-PdO-12, is almost totally covered by PdO

nanoflakes as shown by Figs. 6-1(e) and 1(f), respectively. Figure 6-2 shows XRD spectra of the P-25 and the PdO/TiO₂ heterostructure samples. Before the PdO deposition, the bare P25-TiO₂ sample shows a XRD spectrum typical for commercial Degussa P-25 TiO₂ powders. The TiO₂-PdO-1 heterostructure does not show apparent diffraction peaks associated with PdO. However, for the heterostructure with the PdO deposition time larger than 1 min, the intensity of the diffraction peaks due to the (101), (110), (103) and (202) planes of the PdO tetragonal lattice increases with the PdO deposition time. The strong and well resolved XRD peaks indicate that PdO nanoflakes grown in the heterostructure samples has a good crystallinity after the thermal anneal.



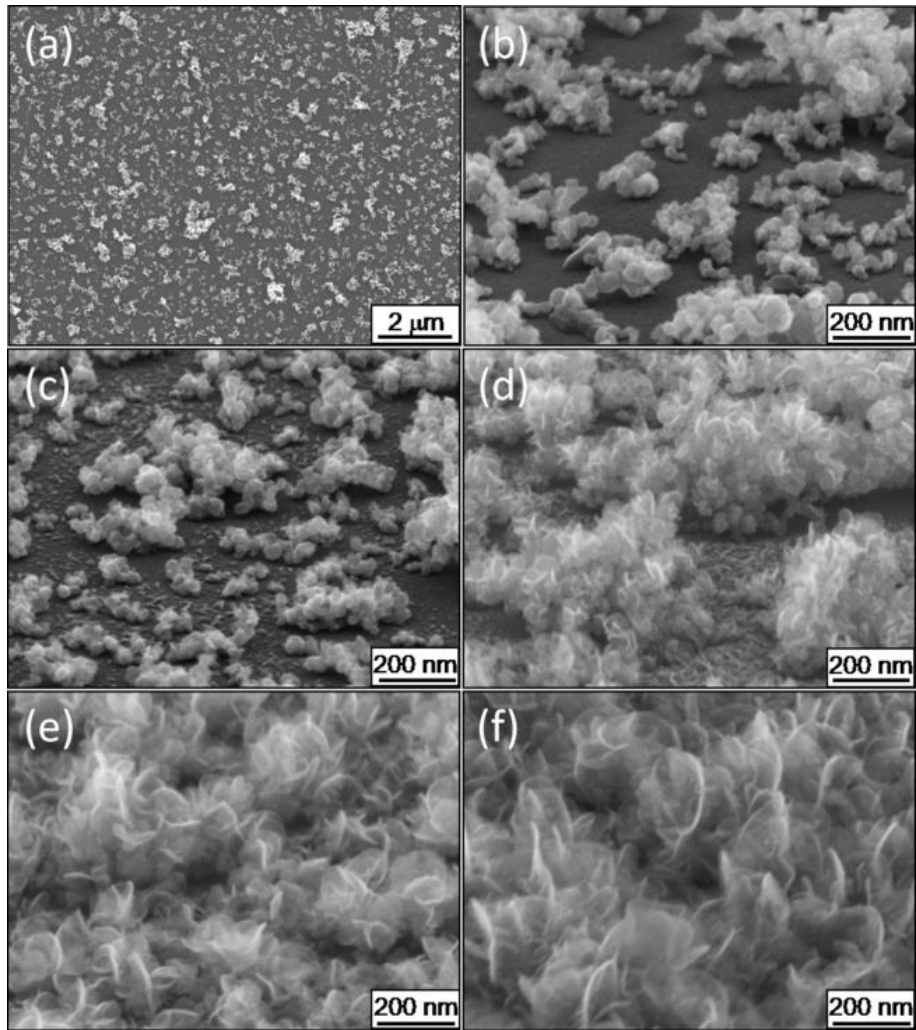


Figure 6-1 (a) SEM images of P-25 TiO₂ nanoparticles spun on the SiO₂ substrate; SEM images the PdO/TiO₂ heterostructures prepared with different PdO deposition times: (b) 1 min, (c) 3 min, (d) 4 min, (e) 8 min, and (f) 12 min.

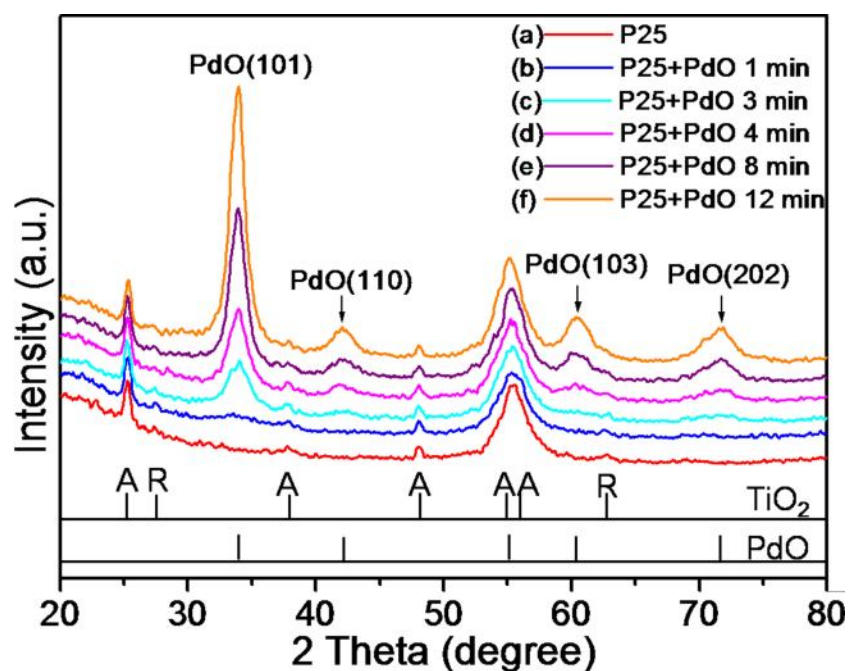


Figure 6-2 XRD spectra of (a) the P-25 sample, and the PdO/TiO₂ heterostructures prepared with different PdO deposition times: (b) 1 min, (c) 3 min, (d) 4 min, (e) 8 min, and (f) 12 min.

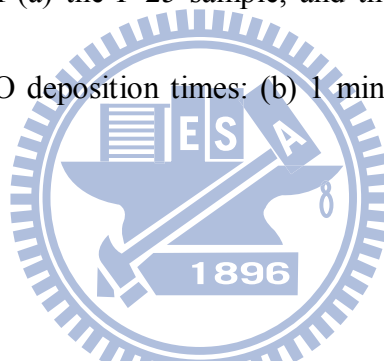
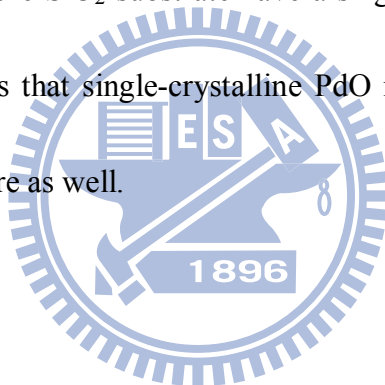


Figure 6-3 shows TEM images of the P-25 and the as-prepared PdO/TiO₂ heterostructure samples. The TEM specimens were prepared by scratching the sample surface with a tweezers. According to figure 6-3(a), the P-25 TiO₂ nanoparticles have a size of ~25-40 nm. After the PdO deposition of 1 min, nanograins with a size of ~2-3 nm uniformly distribute over the P-25 nanoparticle as shown in the inset of figure 6-3(b). The corresponding high resolution TEM (HRTEM) image (figure6-4(a)) indicates that the nanograins are PdO nanocrystals as revealed by the lattice fringe associated with the PdO(101) plane, which has a lattice

spacing of 0.267 nm. The TEM images of Figs. 6-3(c)-(f) clearly show the presence of ultrathin sheets mixed with P-25 nanoparticles. These ultrathin sheets must be the nanoflakes observed in the above SEM images. Dark fringes observed in the TEM images are likely edge areas of the nanoflakes. The HRTEM image of figure 6-4(b) shows a selected area in figure 6-3(f), in which one dark fringe is present. The lattice spacings marked in the area of dark contrast correspond to the (103) and the (101) planes of the PdO tetragonal lattice structure. We have previously found that PdO nanoflakes grown on the SiO₂ substrate have a single crystalline structure [65]. The TEM analysis suggests that single-crystalline PdO nanoflakes can be grown in the PdO/TiO₂ heterostructure as well.



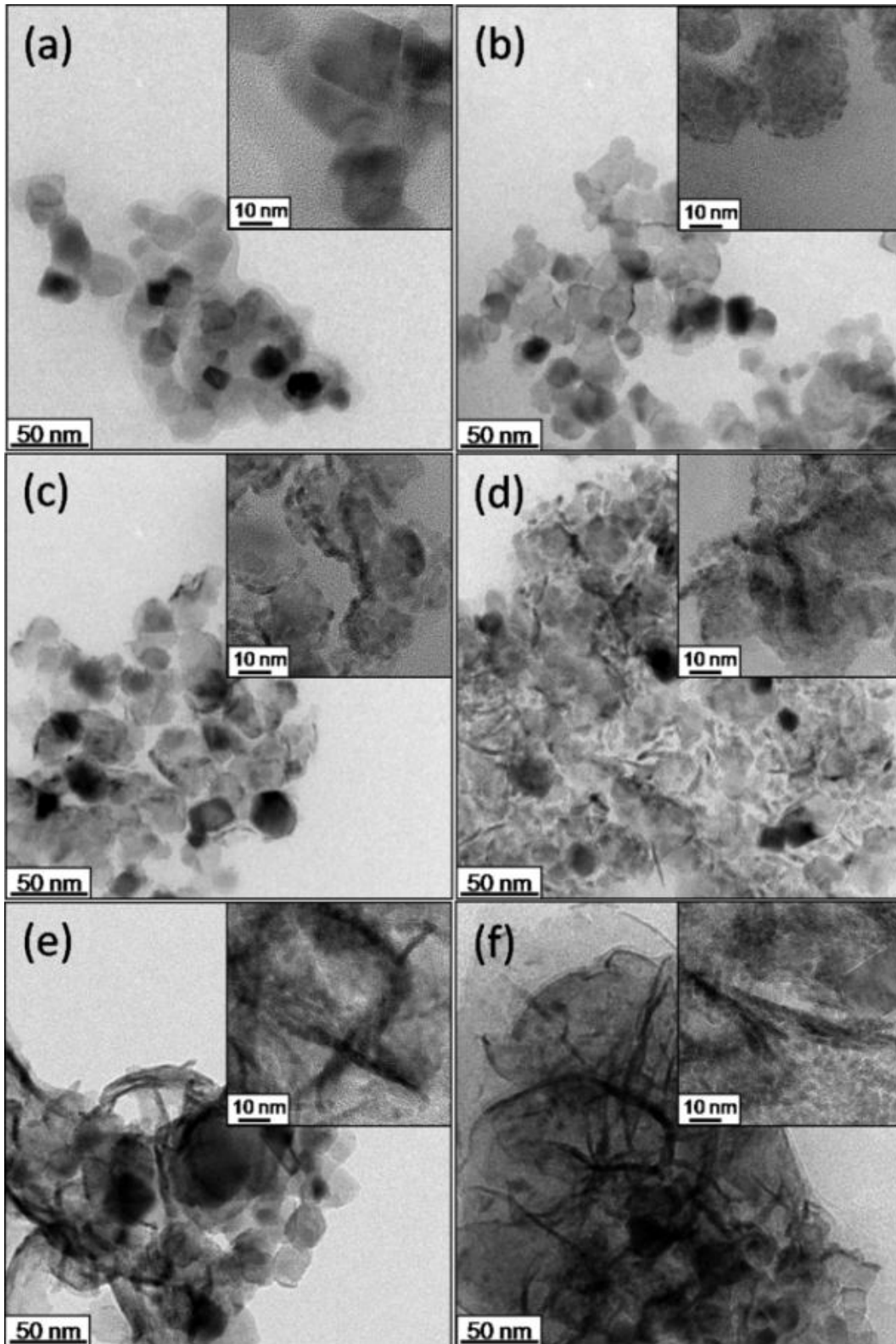


Figure 6-3 BFTEM images of the P-25 sample (a), and the PdO/TiO₂ heterostructures prepared with different PdO deposition times: (b) 1 min, (c) 3 min, (d) 4 min, (e) 8 min, and (f) 12 min. The insets in (a)-(f) are the corresponding HRTEM images.

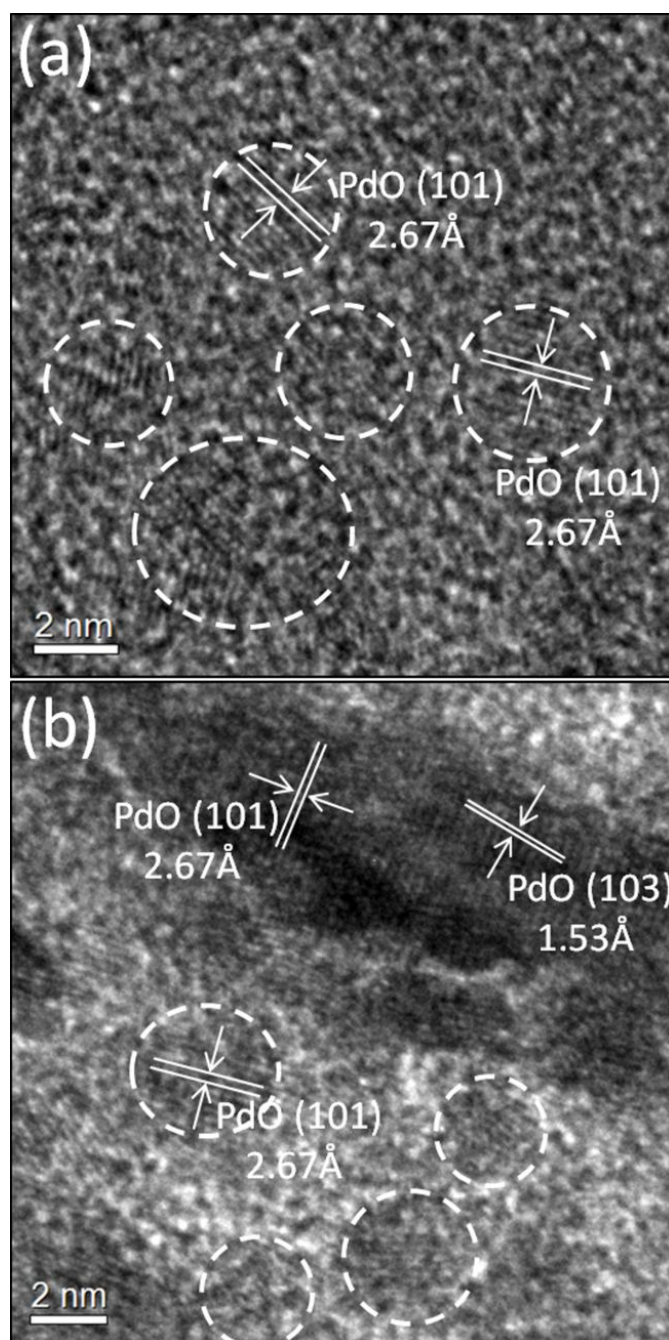


Figure 6-4 HRTEM images of (a) the TiO₂-PdO-1 and (b) the TiO₂-PdO-12 heterostructures.

The UV-vis diffuse reflection absorption spectra of the bare P-25 sample and the PdO/TiO₂ heterostructures prepared with five different PdO deposition times are

shown in figure 6-5. P-25 nanoparticles can only absorb light of wavelength shorter than ~ 380 nm because of its wide bandgap. After the PdO deposition, the absorption wavelength of the PdO/TiO₂ heterostructures extends to ~ 600 nm and the absorbance increases with the PdO deposition time. The extension of the light absorption to the lower energy region for the heterostructure samples must be due to the contribution from the visible light absorption by PdO nanoflakes, which have a light absorption range from ~ 300 -650 nm according to the UV-vis absorption spectrum.

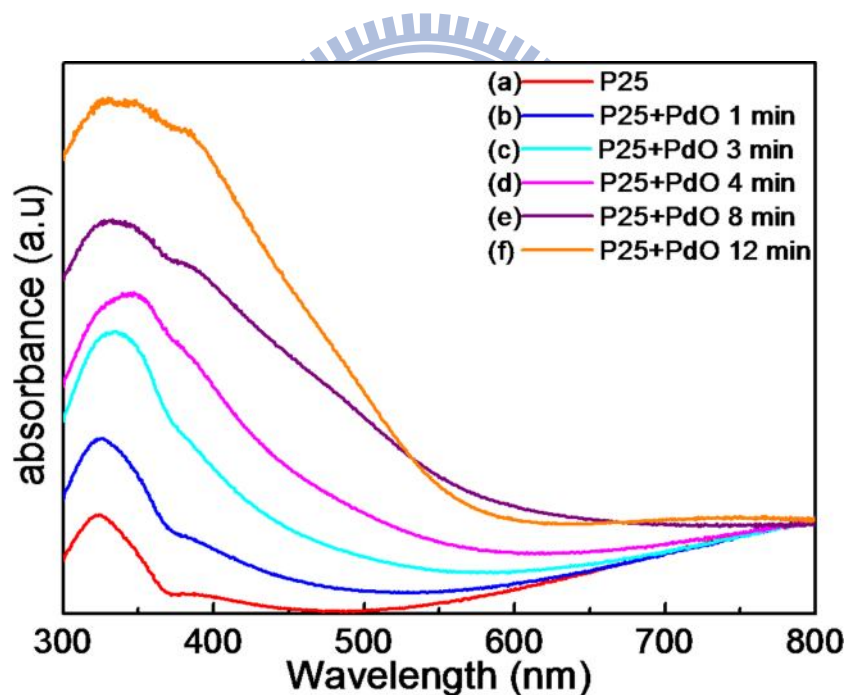


Figure 6-5 UV-vis diffuse reflection absorption spectra of the as-prepared photocatalysts: (a) the P-25 sample, and the PdO/TiO₂ heterostructures prepared with different PdO deposition times: (b) 1 min, (c) 3 min, (d) 4 min, (e) 8 min, and (f) 12 min.

6.2 Photocatalytic Degradation of Methylene Blue by PdO/TiO₂ heterostructures

UV-vis absorption spectroscopy is used to study the photocatalytic activity of PdO/TiO₂ heterostructures toward methylene blue molecules. Figure 6-6(a) shows time-dependent absorption spectra of MB solutions in the presence of TiO₂-PdO-4 under UV-vis light illumination. When the illumination time increases, the intensity of the light absorption at 665 nm greatly decreases, indicating that a considerable amount of MB molecules decompose under the photocatalytic reaction condition. Figure 6-6(b) shows the normalized MB concentration (C/C_0) as a function of the illumination time, where C and C_0 are the residual and the initial concentrations of MB, respectively, for the bare P-25 and the PdO/TiO₂ heterostructure samples. In the absence of the photocatalyst, the decrease in the MB concentration is due to the self-photolysis of the MB solution [51]. The degradation rate of the MB solution using the bare PdO thin film as the photocatalyst is similar to that of the MB control solution. On the other hand, the bare P-25 sample greatly enhances the MB photodegradation; about 71% of MB decomposes after four hours of UV-vis light illumination. When PdO is deposited on P-25 nanoparticles, the MB photodegradation rate can be much further enhanced. All the PdO/P25 heterostructures shown in fig. 6-6(b) exhibit a higher MB photodegradation rate

compared with the bare P-25 photocatalyst. The MB photodegradation efficiency using $\text{TiO}_2\text{-PdO-1}$, $\text{TiO}_2\text{-PdO-3}$ and $\text{TiO}_2\text{-PdO-4}$ as the catalyst are $\sim 89.7\%$, $\sim 92.6\%$ and $\sim 96.1\%$, respectively, after four hours of UV-vis light illumination. Taking the MB self-photolysis under UV-vis light illumination into account, we find that the $\text{TiO}_2\text{-PdO-4}$ heterostructure has a photodegradation efficiency about twice as large as the bare P-25 sample. However, the increase in the PdO loading does not accordingly increase the photocatalytic activity of the PdO/ TiO_2 heterostructure. The photocatalytic activity of $\text{TiO}_2\text{-PdO-8}$ and $\text{TiO}_2\text{-PdO-12}$ heterostructures becomes smaller when more PdO nanoflakes are deposited on the heterostructure samples. Among all the tested PdO/ TiO_2 photocatalysts, $\text{TiO}_2\text{-PdO-4}$ produces the best photodegradation efficiency and $\text{TiO}_2\text{-PdO-12}$ produces the least. Because PdO alone does not promote MB photodegradation under UV-vis illumination, the lower photocatalytic activity of the $\text{TiO}_2\text{-PdO-8}$ and $\text{TiO}_2\text{-PdO-12}$ samples is ascribed to a smaller bare TiO_2 surface area available for the MB photocatalysis. The other likely explanation is that the UV light absorption by TiO_2 nanoparticles is hindered when more PdO nanoflakes, which absorb a large part of incident UV photons, is deposited on the top of the TiO_2 nanoparticles.

To study if PdO could enhance the photocatalytic activity of TiO_2 in the visible light range, we cut off the UV light from the xenon lamp with a 420 nm edge filter

and repeated the MB photodegradation test using the same experimental condition. The experiment shows that all the test samples demonstrate little photocatalytic activity toward MB degradation as shown in figure 6-6(c). The decay of the MB concentration is due to self-photolysis of MB molecules under the visible light illumination. This result clearly shows that the PdO/TiO₂ heterostructure can exhibit photocatalytic activity enhancement only when both the semiconductor oxides are simultaneously photoexcited.



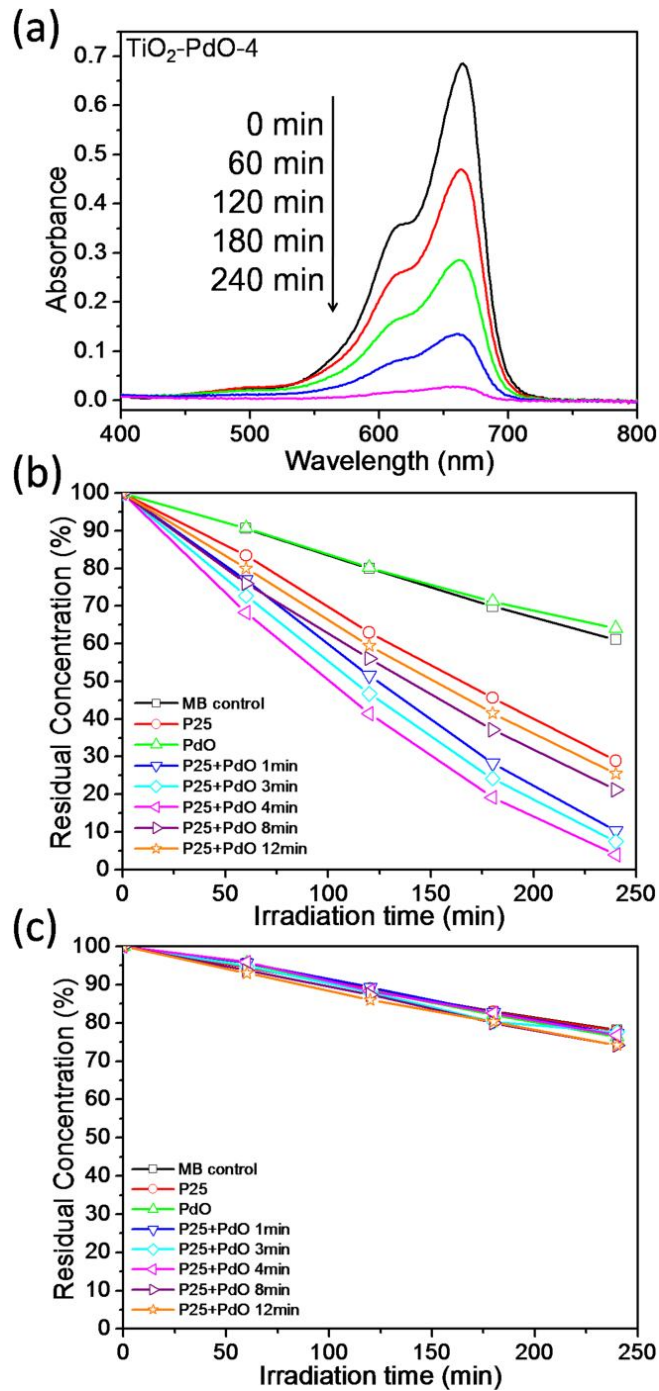


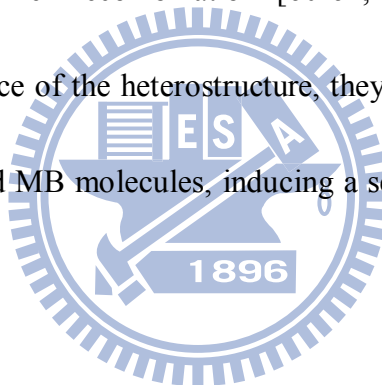
Figure 6-6 (a) Absorption spectra of MB solutions as a function of the UV light illumination time in the presence of $\text{TiO}_2\text{-PdO-4}$; The illumination time dependent normalized concentration of the MB aqueous solution photocatalyzed by the P-25 sample and the PdO/TiO_2 heterostructures prepared with different PdO deposition times (b) under UV-vis light illumination and (c) under visible light illumination.

6.3 Charge Transfer Mechanisms in PdO/TiO₂

heterostructures

The enhanced photocatalytic activity of the PdO/TiO₂ heterostructure toward MB degradation can be ascribed to fast charge transfer between the PdO and TiO₂ nanostructures, which effectively separates the photogenerated electron-hole pairs and thus promotes the efficiency of photocatalytic MB decomposition. To facilitate the MB decomposition, interfacial charge transfer between active surface species on the photocatalyst and adsorbed organic molecules must be prevailing over carrier recombination. Because the recombination lifetime (picoseconds to nanoseconds) [81] is much shorter than the time required for the interfacial charge transfer reaction (microseconds to milliseconds) [81], electron-hole pair separation should be fast enough so that the interfacial charge transfer reaction can take place before the carrier recombination occurs. In the case of the PdO/TiO₂ heterostructure, the junction barrier developed between the two oxide semiconductors can enhance electron-hole pair separation. When a semiconductor is brought in contact with the other semiconductor of larger bandgap, band alignment leads to the formation of a staggered heterojunction (type-II heterojunction) as illustrated by the band diagram in figure6-7 [61, 82-83]. Because of the large bandgap difference between PdO (~2.02 eV) and TiO₂ (~3.2 eV), the heterojunction formed by the p-type PdO and the n-type

TiO₂ nanostructures has asymmetrical energy barriers at the heterointerface. Upon UV-vis light illumination, electrons in the valence bands of the two semiconductors in the heterostructure are excited to the respective conduction bands, leaving holes in the valence bands. The energy barrier developed at the PdO/TiO₂ heterojunction will drive photogenerated electrons and holes to transport, respectively, to the conduction band of the TiO₂ and the valence band of the PdO. The built-in field at the heterojunction can promote fast separation of photogenerated electron-hole pairs, thereby greatly reduce carrier recombination [60-61, 84]. When the separated carriers diffuse to the surface of the heterostructure, they react with hydroxyl surface species, adsorbed water and MB molecules, inducing a series of reactions which lead to MB decomposition.



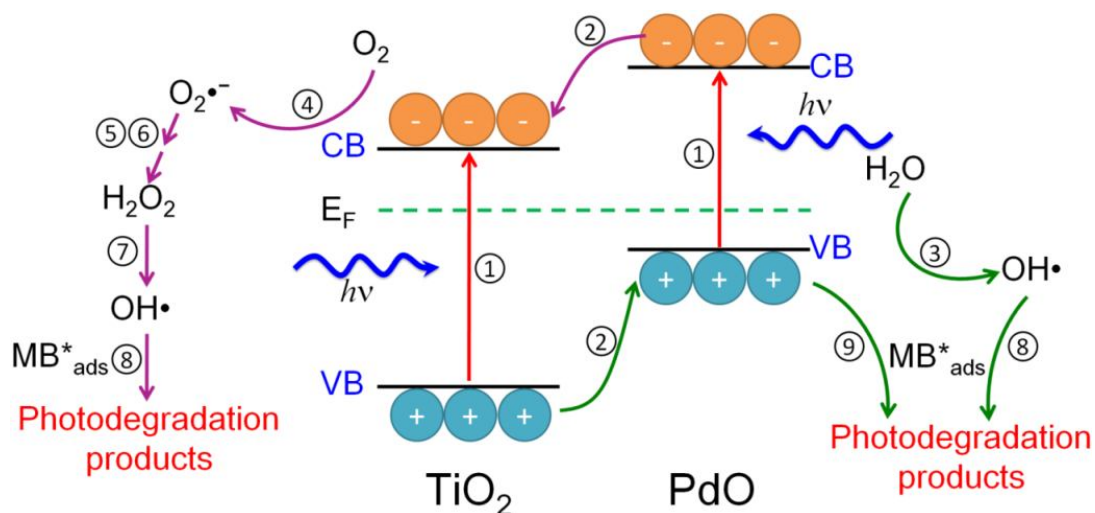
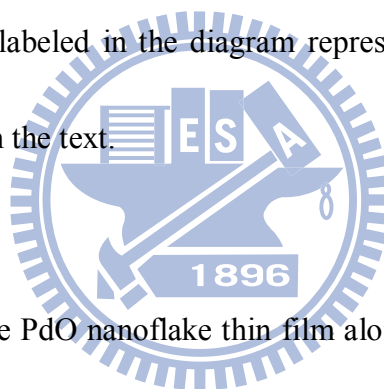


Figure 6-7 Schematic energy band diagram of the PdO/TiO₂ heterostructure.

Possible reaction paths leading to the photocatalytic MB decomposition are also illustrated. The numbers labeled in the diagram represent accordingly the reaction steps (eqs. 1-9) discussed in the text.



From figure 6-6(b), the PdO nanoflake thin film alone does not enhance the MB photodecomposition under UV-vis light illumination. Although the PdO nanoflakes have a strong absorbance in the energy range between ~300-650 nm, photoexcited carriers contribute little to the MB degradation. The photocatalytic inactivity of the bare PdO nanoflake sample is likely due to that intense surface carrier recombination occurs in PdO nanoflakes, thereby hindering the interfacial charge transfer reactions leading to the MB decomposition. Without the junction barrier as the one formed in the PdO/TiO₂ heterostructure, photogenerated carriers can quickly diffuse to the nanoflake surface because the PdO nanoflakes have a very small thickness in the

range of ~15-20 nm. In our previous study, TEM analyses showed that many nanosized PdO grains in square shape, which were rich in dislocations, distributed over the bowed PdO nanoflakes (figure 5-5). The surface defects can act as carrier recombination centers or traps, resulting in a substantial reduction in the photocatalytic activity of the PdO thin film. One other possible cause for the photocatalytic inactivity is the mismatch between the quasi-Fermi levels of photoexcited carriers in the PdO nanoflake and the redox potential of surface reactions leading to the MB decomposition. Verifying this possibility needs further study.

6.4 Photodegradation of MB in PdO/TiO₂ hetrostructures

Photodegradation of organic chemicals catalyzed by TiO₂ has been extensively studied, and the photocatalytic reaction mechanism of TiO₂ is usually used as a model mechanism to explain photocatalytic reactions of other oxide semiconductors. It is generally proposed that organics photodegradation catalyzed by oxide semiconductors in aqueous solution proceeds via a complex reaction mechanism, involving formation of different surface radicals and oxidation of the adsorbed organic compound [85-86]. Among various reaction intermediates, surface hydroxyl radicals (OH•), whose formation is primarily promoted by photogenerated carriers, play an important role in

initiating organics photodegradation. Moreover, holes diffusing to the surface can directly oxidize organic molecules, followed by a series of chain reactions leading to organics decomposition. We believe that the same reaction mechanism is also applicable to the MB photodegradation catalyzed by the PdO/TiO₂ heterostructure. We thus propose that the MB photodegradation catalyzed by the PdO/TiO₂ heterostructure proceeds via the following reaction steps:

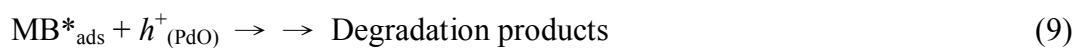
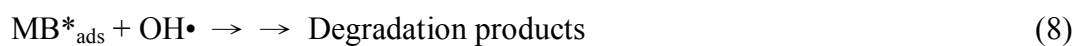
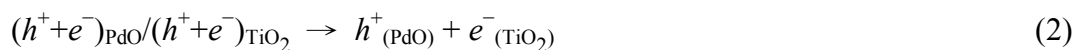
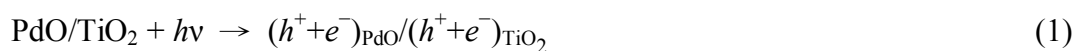


Figure 6-7 illustrates the sequential reaction steps for the MB photodecomposition. First, electron-hole pairs are photogenerated both in the PdO and the TiO₂ semiconductors upon UV-vis illumination (Eq. 1), followed by fast electron and hole transports to the TiO₂ and the PdO, respectively, due to the presence

of the PdO/TiO₂ heterojunction (Eq. 2). Holes diffusing to the PdO nanoflake surface can react with adsorbed H₂O molecules (and/or OH surface groups), producing surface bound OH• radicals (Eq. 3). Photogenerated electrons transporting to the P-25 TiO₂ nanoparticle can also initiate OH• radicals via the transient formation of hydroperoxide radicals (Eqs. 4-5), which is followed by disproportionation forming H₂O₂ and oxygen (Eq. 6). The H₂O₂ is then reduced by electrons, producing OH• radicals on the TiO₂ nanoparticle (Eq. 7). Attack of OH• radicals on MB molecules adsorbed on the PdO/TiO₂ heterostructure will start a series of chain reactions leading to the MB decomposition (Eq. 8). The asterisk symbol on the MB_{ads} represents the MB parent molecule and its photodecomposed fragments adsorbed on the heterostructure, and the double arrows in series denote the occurrence of the chain reactions which lead to the MB decomposition. In addition to MB oxidation by OH• radicals, direct oxidation of MB by hole carriers, which are strong oxidants, can take place on the PdO nanoflake (Eq. 9).

Although TiO₂ is inactive toward photocatalysis under visible light illumination due to the high bandgap energy in the UV light range, one might yet expect that the PdO/TiO₂ heterostructure could promote the MB photodegradation under visible light illumination when photoexcitation of PdO nanoflakes is taken into consideration. It is generally believed that photoresponse of TiO₂ can be extended to the visible light

region when it forms heterojunction with a narrow bandgap semiconductor [59-60].

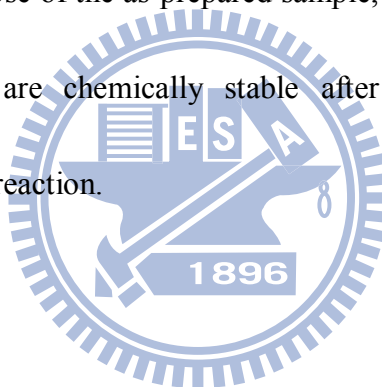
However, as shown in figure 6-6(c), the PdO/TiO₂ heterostructure did not exhibit perceivable photocatalytic activity toward MB degradation under visible light illumination. In a study of photoresponse of Si/TiO₂ core/shell nanowires, Yang et al. found that the composite did not produce photocurrent under visible light illumination. They ascribed the absence of photocurrent to that the charge separation shifted quasi-Fermi energies of carriers in Si, thereby the flat band condition was eventually reached and the charge separation was thus retarded [87].

The concept that charge separation alters the quasi-Fermi levels of nonequilibrium photogenerated carriers may be used to explain the absence of photocatalytic activity of the PdO/TiO₂ heterostructure during visible light illumination. To facilitate a photocatalytic reaction, the quasi-Fermi levels of holes and electrons must reach the potentials for the oxidation and reduction reactions, respectively, such as in the case of photoelectrolysis of water using semiconductors as the catalyst [88]. It is likely that, under visible light illumination, the quasi-Fermi levels of photogenerated carriers in the PdO and TiO₂ nanostructures do not match the redox potentials of the primary surface reactions initiating the MB decomposition. Therefore, interfacial charge transfer between carriers and active surface species is not allowed and carrier recombination in the PdO nanoflake becomes the dominant channel for

photogenerated carriers to return to the ground state. As a result, the PdO/TiO₂ heterostructure exhibits little photocatalytic activity toward the MB degradation in the visible light range.

High chemical stability and recyclability of photocatalysts are desirable for practical photocatalytic applications. The PdO/TiO₂ heterostructures can maintain a very stable photocatalytic activity toward MB degradation after many photocatalysis tests. Figure 6-8 shows the normalized MB concentration as a function of the UV-vis illumination time for three MB photodegradation tests, using the TiO₂-PdO-4 sample as the recycled photocatalyst. The sample received only DI water rinse for 2 min between two successive tests. Compared with the first photodegradation test (the first panel), the fifth and tenth tests show that a similar photocatalytic efficiency can be obtained for the recycled photocatalyst. The excellent recyclability is due to that the surface of the PdO nanoflake retains its chemical states after the MB photodegradation as suggested by XPS analyses. Figure 6-9 shows X-ray photoelectron spectra (XPS) of the PdO/TiO₂ heterostructure photocatalyst before and after 10 recycling tests of MB photocatalytic degradation. The C(1s) and Pd(3d) XPS spectra shown in figure 6-9(A) and (B), respectively, are acquired from the TiO₂-PdO-4 sample, and the Ti(2p) spectrum (C) is from the TiO₂-PdO-1 sample because the signal to noise ratio of the Ti(2p) peak of the sample is much better due to

less PdO nanoflakes covering the TiO₂ nanoparticles. The intensity of the C(1s) signal is small and shows little change after the recycling tests, indicating the C(1s) signal originated from adventitious contamination in ambient atmosphere. For the as-prepared PdO/TiO₂ heterostructure sample, the position of the Pd(3d_{5/2}) signal (~336.9 eV) and the Ti(2p_{3/2}) signal (~458.5 eV) corresponds to the chemical state of PdO and TiO₂, respectively. After the recycling test, the binding energy, the intensity and the peak shape of the Pd(3d_{5/2}) and the Ti(2p_{3/2}) signals do not show obvious difference from those of the as-prepared sample, indicating that both the PdO and TiO₂ nanostructures are chemically stable after many cycles of the MB photocatalytic degradation reaction.



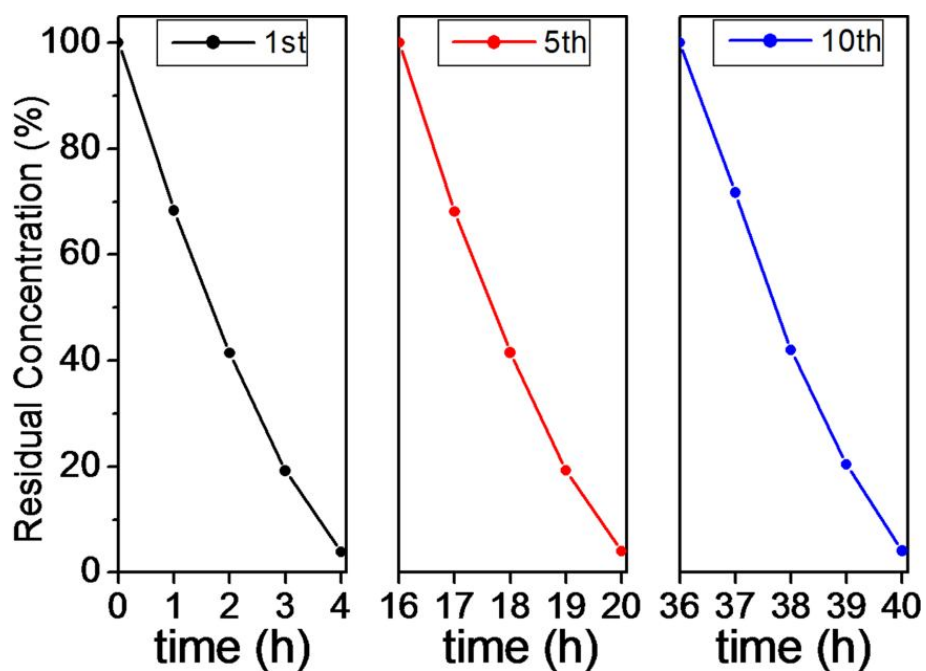


Figure 6-8 C/C_0 versus irradiation time plots of recycling test on PdO/TiO₂

heterostructure for MB photodegradation. RSD time of PdO = 4 min.

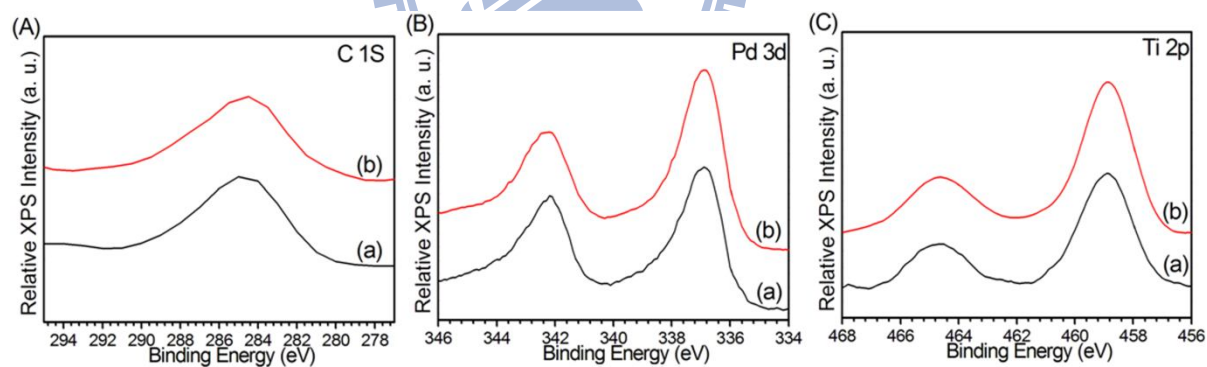


Figure 6-9 (A) C(1s), (B) Pd(3d) and (C) Ti(2p) XPS spectra of the PdO/TiO₂

photocatalyst: (a) before and (b) after MB photocatalytic degradation.

6.5 Summary

Ultrathin PdO nanoflakes were prepared by reactive sputter deposition to form a heterostructure with TiO₂ nanoparticles spin-coated on the SiO₂ substrate, and the photocatalytic performance of PdO/TiO₂ heterostructure toward MB decomposition was studied. The photocatalytic activity of TiO₂ toward MB decomposition under UV-vis light illumination is greatly enhanced by the heterostructure, and an enhancement as large as 200% was obtained for the PdO/TiO₂ heterostructure with 4 min PdO deposition under the present deposition condition. The enhancement of the photocatalytic activity is ascribed to that the fast photogenerated carrier separation, which results from the formation of the potential barrier at the heterojunction between the two semiconductor oxides, reduces the carrier recombination rate, thereby leading to an efficient interfacial charge transfer, which is a prerequisite step for initiating primary surface reactions for MB decomposition. We have proposed a photocatalytic reaction mechanism for the MB decomposition on the PdO/TiO₂ heterostructure. Under visible light illumination, the PdO/TiO₂ heterostructure exhibits little photocatalytic activity toward the MB decomposition although PdO can be photoexcited in the visible light range. We suggest that the photocatalytic inactivity is due to the mismatch between the quasi-Fermi levels of nonequilibrium photogenerated carriers in the heterostructure and redox potentials of primary surface

reactions leading to the MB decomposition. The PdO/TiO₂ heterostructure can retain its photocatalytic activity after many MB photocatalysis tests, showing its great potential for photocatalytic applications which require a long-term stability.



Chapter 7

Conclusions and Future Works

7.1 Conclusions

In this study, PdO nanflake thin films are deposited by reactive sputter deposition. Three kinds of nanostructures including Pd-PdO coreshell nanoflakes, single-crystalline PdO nanoflakes and PdO/TiO₂ heterostructure are prepared. Because PdO nanoflakes vertically standing on the substrate had a sharp top edge and a high aspect ratio in terms of the thickness and height, they are expected to have good electrical, optical and chemical properties including field emission, photoresponse and photocatalysis. The primary results obtained in this thesis are summarized as follows:

- (a) At temperatures at 200 °C and below, the PdO thin film grown on the Pt substrate had a flake-like morphology. TEM, XRD and XPS studies revealed that the nanoflake had a core-shell structure with a single Pd grain encapsulated by a crystalline PdO surface layer. The PdO layer was about 4-6 nm in thickness and epitaxially aligned with the Pd lattice.
- (b) Formation of the Pd-PdO nanoflakes resulted from the large interfacial stress due to the large lattice mismatch between the PdO surface layer and the Pt substrate.

The Pd grain growth in the nanoflake was facilitated by the close similarity in the lattice parameters of the Pt and Pd fcc crystal structures. Because of the sharp top edge and a high aspect ratio, the Pd-PdO nanoflake exhibited a field emission efficiency comparable to many 1-D nanoemitters. A β value of 791 was obtained for the nanoflake deposited at 200 °C.

- (c) PdO nanoflake grown on the SiO₂ surface at the room temperature and annealed at 400°C has a single crystalline structure according to TEM and XRD studies. The well-crystalline 400°C-annealed nanoflake thin film has a bandgap energy in the red-light range (~2.06 eV), and exhibits a very sensitive photoresponse upon the UV (365 nm) illumination.
- (d) The high photoresponse sensitivity of the 400°C-annealed nanoflake thin film is ascribed to a lower density of recombination centers and traps due to the excellent crystallinity of the nanoflakes and a high carrier extraction efficiency due to the low electrical resistivity. This study indicates that the high-temperature annealed PdO nanoflake thin film has desirable characteristics for applications demanding sensitive photoresponse, such as photodetectors and photoswitches.
- (e) Ultrathin PdO nanoflakes were prepared by reactive sputter deposition to form a heterostructure with TiO₂ nanoparticles spin-coated on the SiO₂ substrate, and the photocatalytic performance of PdO/TiO₂ heterostructure toward MB

decomposition under UV-vis light illumination is greatly enhanced by the heterostructure. An enhancement as large as 200% was obtained for the PdO/TiO₂ heterostructure with 4 min PdO deposition under the present deposition condition.

- (f) The enhancement of the photocatalytic activity is ascribed to that the fast photogenerated carrier separation, which results from the formation of the potential barrier at the heterojunction between the two semiconductor oxides, reduces the carrier recombination rate, thereby leading to an efficient interfacial charge transfer, which is a prerequisite step for initiating primary surface reactions for MB decomposition. The PdO/TiO₂ heterostructure can retain its photocatalytic activity after many MB photocatalysis tests, showing its great potential for photocatalytic applications which require a long-term stability

7.2 Future works

We have shown that the PdO nanoflake is an ideal material in electric and optic for field emission, photoresponse and photocatalysis applications. However, some subjects should be further studied

(a) A systematic study of the temperature dependence of the PdO growth in reactive sputter deposition should be preceded. In our preliminary study, PdO nanoroads instead of nanoflakes are grown at a higher substrate temperature $> 300\text{ }^{\circ}\text{C}$. The properties should be further studied.

(b) In our photoresponse measurement, PdO nanoflakes show a high sensitivity toward UV light. A rapid gas adsorption and desorption rate is the main factor inducing a high photoresponse. Gas sensor will be a good application for PdO nanoflakes. For CO gas sensor applications, CO adsorption on the PdO nanoflake thin film can be study by XPS and TDS. The CO adsorption study should be correlated with CO gas sensing characteristics of the PdO nanoflake thin film. Photo-assisted CO gas sensing on the PdO nanoflake thin film should also investigated.

(c) The photocatalytic activity of TiO_2 toward MB decomposition is greatly enhanced as large as 200% for the PdO/ TiO_2 heterostructure with 4 min PdO deposition under the present deposition condition. We believe the PdO/ TiO_2 heterostrucute

can also decompose other reagents or contaminants such as Acid Orange, Rhodamine B and E. coli efficiently. Some kinds of heterostructure such as PdO/ZnO and PdO/SnO₂ with Pd base to absorb visible light should be further studied.



Appendix

Cyclic voltammetry (CV) is a dynamic electrochemical method for measuring redox events. It can be used to study the electrochemical behavior of species diffusing to an electrode surface, interfacial phenomena at an electrode surface, and bulk properties of materials in or on electrodes. Cyclic voltammetry (CV) is one of the useful methods for estimating the energy level of organic compounds. The oxidation process corresponds to the removal of electrons from the highest occupied molecular orbital (HOMO), whereas the reduction cycle corresponds to the filling by electrons of the lowest unoccupied molecular orbital (LUMO). Therefore, the onset oxidation and reduction potentials are closely related to the energies of the HOMO and LUMO levels of a organic molecule and thus can provide important information regarding the magnitude of the energy gap. By this method, we can obtain the conduction band and valance band of PdO nanoflake thin films.

Electrochemical measurements were performed on a Voltammetric Analyzer (BAS, CV-50 W) in a three electrode cell with a working electrode of carbon clothes, a reference electrode (SCE) and a counter electrode (Pt gauze) in 0.1 M acetonitrile solution with (n-Bu)₄NClO₄ as supporting electrolyte PdO nanoflake thin films were then deposited on the precleaned carbon clothes. The scan potential was set as

from -2.0 V to 2.0V, and the scan rate was set at 20 mV/s. Figure A shows the cyclic voltammogram of the PdO nanoflake thin film. The onset potentials of oxidation and reduction are ~1.47 V and -0.78 V respectively. To obtain the LOMO and HUMO energy levels, the energy values can be calculated by using the ferrocence (FOC) value of -4.8 eV with respect to the vacuum level which is defined as zero in the follow equation [89-90]:

$$(E_{\text{onset(ox)}}) \text{ vs. FOC} = -4.8 - \text{HOMO}$$

$$(E_{\text{onset(red)}}) \text{ vs. FOC} = -4.8 - \text{LUMO}$$

Therefore, we obtain the HOMO (valance band) and LUMO (conduction band) energy levels as -6.27 eV and -4.02 eV with respect to the vacuum level. Compared to TiO₂, the CB of the PdO nanoflake thin film is 0.38 eV higher than that of TiO₂ [91]. This indicates that the photogenerated electrons in the PdO/TiO₂ heterostructure will transfer from the CB of PdO to that of TiO₂. On the other hand, the VB of the PdO nanoflake thin film is 1.13 eV higher than that of TiO₂, photogenerated holes will transfer from the CB of TiO₂ to that of PdO. Therefore, carrier recombination is greatly reduced. When the separated carriers diffuse to the surface of the heterostructure, they react with hydroxyl surface species, adsorbed water and MB molecules, inducing a series of reactions which lead to MB decomposition.

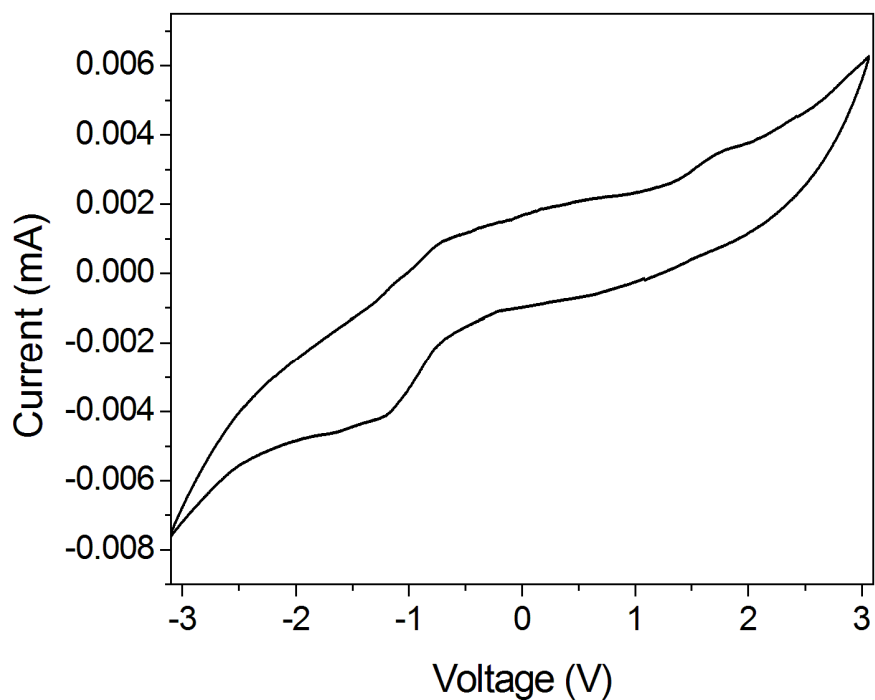


Figure A Cyclic voltammogram of the PdO nanoflake thin film in 0.1 M n-Bu₄NClO₄ with scan rate of 20 mv/s.

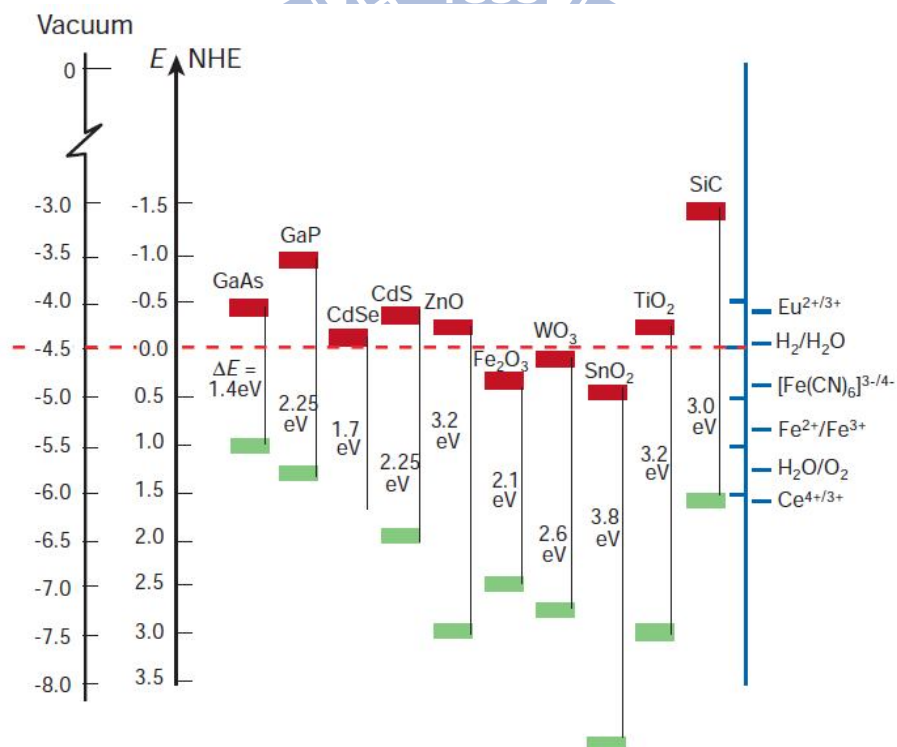
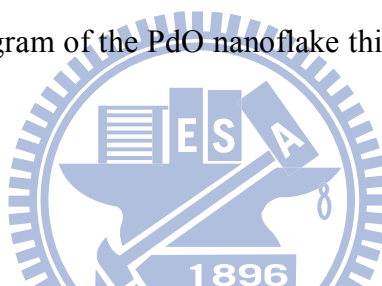


Figure B Energy for various semiconductor in aqueous electrolyte at pH= 1 [91].

References

- [1] Alivisatos, P.; Barbara, P. F.; Castleman, A. W.; Chang, J.; Dixon, D. A.; Klein, M. L.; McLendon, G. L.; Miller, J. S.; Ratner, M. A.; Rossky, P. J.; Stupp, S. I.; Thompson, M. E., From Molecules to Materials: Current Trends and Future Directions. *Advanced Materials* **1998**, *10* (16), 1297.
- [2] Preface to the Special Issue. *Chemistry of Materials* **1996**, *8* (8), 1569.
- [3] Ozin, G. A., Nanochemistry: Synthesis in diminishing dimensions. *Advanced Materials* **1992**, *4* (10), 612.
- [4] Klimov, V. I.; Mikhailovsky, A. A.; Xu, S.; Malko, A.; Hollingsworth, J. A.; Leatherdale, C. A.; Eisler, H.-J.; Bawendi, M. G., Optical Gain and Stimulated Emission in Nanocrystal Quantum Dots. *Science* **2000**, *290* (5490), 314.
- [5] Lin, Y.-T.; Chen, C.-Y.; Hsiung, C.-P.; Cheng, K.-W.; Gan, J.-Y., Growth of RuO₂ nanorods in reactive sputtering. *Applied Physics Letters* **2006**, *89* (6), 063123.
- [6] Wan, Q.; Li, Q. H.; Chen, Y. J.; Wang, T. H.; He, X. L.; Li, J. P.; Lin, C. L., Fabrication and ethanol sensing characteristics of ZnO nanowire gas sensors. *Applied Physics Letters* **2004**, *84* (18), 3654.
- [7] Law, J. B. K.; Thong, J. T. L., Simple fabrication of a ZnO nanowire photodetector with a fast photoresponse time. *Applied Physics Letters* **2006**, *88* (13), 133114.
- [8] Porter, H. L.; Cai, A. L.; Muth, J. F.; Narayan, J., Enhanced photoconductivity of ZnO films Co-doped with nitrogen and tellurium. *Applied Physics Letters* **2005**, *86* (21), 211918.
- [9] Sun, W.-T.; Yu, Y.; Pan, H.-Y.; Gao, X.-F.; Chen, Q.; Peng, L.-M., CdS Quantum Dots Sensitized TiO₂ Nanotube-Array Photoelectrodes. *Journal of the*

American Chemical Society **2008**, 130 (4), 1124.

[10] Gélin, P.; Primet, M., Complete oxidation of methane at low temperature over noble metal based catalysts: a review. *Applied Catalysis B: Environmental* **2002**, 39 (1), 1.

[11] Nosova, L. V.; Stenin, M. V.; Nogin, Y. N.; Ryndin, Y. A., EXAFS and XPS studies of the influence of metal particle size, nature of support and H₂ and CO adsorption on the structure and electronic properties of palladium. *Applied Surface Science* **1992**, 55 (1), 43.

[12] Dare-Edwards, M. P.; Goodenough, J. B.; Hamnett, A.; Katty, A., Evaluation of p-type PdO as a photocathode in water photoelectrolysis. *Materials Research Bulletin* **1984**, 19 (4), 435.

[13] Yamaguchi, E.; Sakai, K.; Nomura, I.; Ono, T.; Yamanobe, M.; Abe, N.; Hara, T.; Hatanaka, K.; Osada, Y.; Yamamoto, H.; Nakagiri, T., A 10-in. surface-conduction electron-emitter display. *Journal of the Society for Information Display* **1997**, 5 (4), 345.

[14] Arai, T.; Shima, T.; Nakano, T.; Tominaga, J., Thermally-induced optical property changes of sputtered PdO_x films. *Thin Solid Films* **2007**, 515 (11), 4774.

[15] Datye, A. K.; Bravo, J.; Nelson, T. R.; Atanasova, P.; Lyubovsky, M.; Pfefferle, L., Catalyst microstructure and methane oxidation reactivity during the Pd \leftrightarrow PdO transformation on alumina supports. *Applied Catalysis A: General* **2000**, 198 (1-2), 179.

[16] Gabasch, H.; Knop-Gericke, A.; Schlögl, R.; Borasio, M.; Weilach, C.; Rupprechter, G.; Penner, S.; Jenewein, B.; Hayek, K.; Klotzer, B., Comparison of the reactivity of different Pd-O species in CO oxidation. *Physical Chemistry Chemical Physics* **2007**, 9 (4), 533.

[17] Oh, S.-H.; Hoflund, G. B., Low-temperature catalytic carbon monoxide

oxidation over hydrous and anhydrous palladium oxide powders. *Journal of Catalysis* **2007**, *245* (1), 35.

[18] Sales, E. A.; Bugli, G.; Ensuque, A.; De Jesus Mendes, M.; Bozon-Verduraz, F., Palladium catalysts in the selective hydrogenation of hexa-1,5-diene and hexa-1,3-diene in the liquid phase. Effect of tin and silver addition. Part 1. Preparation and characterization: From the precursor species to the final phases. *Physical Chemistry Chemical Physics* **1999**, *1* (3), 491.

[19] McBride, J. R.; Hass, K. C.; Weber, W. H., Resonance-Raman and lattice-dynamics studies of single-crystal PdO. *Physical Review B* **1991**, *44* (10), 5016.

[20] Viswanathamurthi, P.; Bhattarai, N.; Kim, H. Y.; Cha, D. I.; Lee, D. R., Preparation and morphology of palladium oxide fibers via electrospinning. *Materials Letters* **2004**, *58* (26), 3368.

[21] Aggarwal, S.; Monga, A. P.; Perusse, S. R.; Ramesh, R.; Ballarotto, V.; Williams, E. D.; Chalamala, B. R.; Wei, Y.; Reuss, R. H., Spontaneous Ordering of Oxide Nanostructures. *Science* **2000**, *287* (5461), 2235.

[22] Wu, Z.; Sheng, Z.; Liu, Y.; Wang, H.; Tang, N.; Wang, J., Characterization and activity of Pd-modified TiO₂ catalysts for photocatalytic oxidation of NO in gas phase. *Journal of Hazardous Materials* **2009**, *164* (2-3), 542.

[23] Su, H.; Dong, Q.; Han, J.; Zhang, D.; Guo, Q., Biogenic Synthesis and Photocatalysis of Pd–PdO Nanoclusters Reinforced Hierarchical TiO₂ Films with Interwoven and Tubular Conformations. *Biomacromolecules* **2008**, *9* (2), 499.

[24] Erkan, A.; Bakir, U.; Karakas, G., Photocatalytic microbial inactivation over Pd doped SnO₂ and TiO₂ thin films. *Journal of Photochemistry and Photobiology A: Chemistry* **2006**, *184* (3), 313.

[25] Tsai, C.-H.; Pan, F.-M.; Chen, K.-J.; Wei, C.-Y.; Liu, M.; Mo, C.-N., Nanogap

formation by palladium hydrogenation for surface conduction electron emitters fabrication. *Applied Physics Letters* **2007**, *90* (16), 163115.

[26] Rogal, J.; Reuter, K.; Scheffler, M., Thermodynamic stability of PdO surfaces. *Physical Review B* **2004**, *69* (7), 075421.

[27] Andrade Sales, E.; Bugli, G.; Ensueque, A.; de Jesus Mendes, M.; x00e; rio; Bozon-Verduraz, o., *Physical Chemistry Chemical Physics* **1999**, *1* (3).

[28] Okamoto, H.; Asô, T., Formation of Thin Films of PdO and Their Electric Properties. *Japanese Journal of Applied Physics* **1967**, *6*, 779.

[29] Rey, E.; Kamal, M. R.; Miles, R. B.; Royce, B. S. H., The semiconductivity and stability of palladium oxide. *Journal of Materials Science* **1978**, *13* (4), 812.

[30] Nilsson, P. O., Optical properties of PdO in the range of 0.5-5.4 eV. *Journal of Physics C: Solid State Physics* **1979**, *12* (7), 1423.

[31] Rogers, D. B.; Shannon, R. D.; Gillson, J. L., Crystal growth and semiconductivity of palladium oxide. *Journal of Solid State Chemistry* **1971**, *3* (2), 314.

[32] Kim, J. G.; Kim, J. H.; Moon, H. S.; Chon, C. M.; Ahn, J. S., Removal capacity of water plant alum sludge for phosphorus in aqueous solutions. *Chemical Speciation and Bioavailability* **2003**, *14* (1-4), 67.

[33] Penner, S.; Wang, D.; Jenewein, B.; Gabasch, H.; Klotzer, B.; Knop-Gericke, A.; Schlogl, R.; Hayek, K., Growth and decomposition of aligned and ordered PdO nanoparticles. *The Journal of Chemical Physics* **2006**, *125* (9), 094703.

[34] Bonard, J.-M.; Salvétat, J.-P.; Stockli, T.; Heer, W. A. d.; Forro, L.; Chatelain, A., Field emission from single-wall carbon nanotube films. *Applied Physics Letters* **1998**, *73* (7), 918.

[35] Wandelt, K., Chapter 7: The Local Work Function of Thin Metal Films: Definition and Measurement. In *Studies in Surface Science and Catalysis*, Wissmann,

P., Ed. Elsevier: 1987; Vol. Volume 32, pp 280.

[36] Cheng, Y.; Zhou, O., Electron field emission from carbon nanotubes. *Comptes Rendus Physique* **2003**, 4 (9), 1021.

[37] Fowler, R. H.; Nordheim, L., Electron Emission in Intense Electric Fields. *Proceedings of the Royal Society of London. Series A, Containing Papers of a Mathematical and Physical Character* **1928**, 119 (781), 173.

[38] Baca-Arroyo, R.; Rodriguez, C. A. L.; Galvan-Arellano, M.; Romero-Paredes, G.; Pena-Sierra, R. In *Field Emission from Palladium Oxide Nanostructures Grown on Si Substrates at Atmospheric Pressure*, Electrical and Electronics Engineering, 2007. ICEEE 2007. 4th International Conference on, 2007; pp 345.

[39] Rose, A., *Concepts in Photoconductivity and Allied Problems*. Krieger Publishing Company: New York, 1978.

[40] Takahashi, Y.; Kanamori, M.; Kondoh, A.; Minoura, H.; Ohya, Y., Photoconductivity of Ultrathin Zinc Oxide Films. *Jpn. J. Appl. Phys.* **1994**, 33, 6611.

[41] Liu, Y.; Gorla, C.; Liang, S.; Emanetoglu, N.; Lu, Y.; Shen, H.; Wraback, M., Ultraviolet detectors based on epitaxial ZnO films grown by MOCVD. *Journal of Electronic Materials* **2000**, 29 (1), 69.

[42] Soci, C.; Zhang, A.; Xiang, B.; Dayeh, S. A.; Aplin, D. P. R.; Park, J.; Bao, X. Y.; Lo, Y. H.; Wang, D., ZnO Nanowire UV Photodetectors with High Internal Gain. *Nano Letters* **2007**, 7 (4), 1003.

[43] Collins, R. J.; Thomas, D. G., Photoconduction and Surface Effects with Zinc Oxide Crystals. *Physical Review* **1958**, 112 (2), 388.

[44] Sharma, P.; Sreenivas, K.; Rao, K. V., Analysis of ultraviolet photoconductivity in ZnO films prepared by unbalanced magnetron sputtering. *Journal of Applied Physics* **2003**, 93 (7), 3963.

[45] Studenikin, S. A.; Golego, N.; Cocivera, M., Carrier mobility and density

contributions to photoconductivity transients in polycrystalline ZnO films. *Journal of Applied Physics* **2000**, *87* (5), 2413.

[46] Li, Q. H.; Wan, Q.; Liang, Y. X.; Wang, T. H., Electronic transport through individual ZnO nanowires. *Applied Physics Letters* **2004**, *84* (22), 4556.

[47] Kind, H.; Yan, H.; Messer, B.; Law, M.; Yang, P., Nanowire Ultraviolet Photodetectors and Optical Switches. *Advanced Materials* **2002**, *14* (2), 158.

[48] Gao, S.-A.; Xian, A.-P.; Cao, L.-H.; Xie, R.-C.; Shang, J.-K., Photoresponse of PdO/TiO₂ film under visible light. *IEEE International Nanoelectronics Conference* **2008**, 782.

[49] Linsebigler, A. L.; Lu, G.; Yates, J. T., Photocatalysis on TiO₂ Surfaces: Principles, Mechanisms, and Selected Results. *Chemical Reviews* **1995**, *95* (3), 735.

[50] Han, X.; Kuang, Q.; Jin, M.; Xie, Z.; Zheng, L., Synthesis of Titania Nanosheets with a High Percentage of Exposed (001) Facets and Related Photocatalytic Properties. *Journal of the American Chemical Society* **2009**, *131* (9), 3152.

[51] Burda, C.; Lou, Y.; Chen, X.; Samia, A. C. S.; Stout, J.; Gole, J. L., Enhanced Nitrogen Doping in TiO₂ Nanoparticles. *Nano Letters* **2003**, *3* (8), 1049.

[52] Chen, C.; Bai, H.; Chang, C., Effect of Plasma Processing Gas Composition on the Nitrogen-Doping Status and Visible Light Photocatalysis of TiO₂. *The Journal of Physical Chemistry C* **2007**, *111* (42), 15228.

[53] Cowan, A. J.; Tang, J.; Leng, W.; Durrant, J. R.; Klug, D. R., Water Splitting by Nanocrystalline TiO₂ in a Complete Photoelectrochemical Cell Exhibits Efficiencies Limited by Charge Recombination. *The Journal of Physical Chemistry C* **2010**, *114* (9), 4208.

[54] Huang, H.; Li, D.; Lin, Q.; Shao, Y.; Chen, W.; Hu, Y.; Chen, Y.; Fu, X., Efficient Photocatalytic Activity of PZT/TiO₂ Heterojunction under Visible Light

Irradiation. *The Journal of Physical Chemistry C* **2009**, *113* (32), 14264.

[55] Wang, X.; Yu, J. C.; Yip, H. Y.; Wu, L.; Wong, P. K.; Lai, S. Y., A Mesoporous Pt/TiO₂ Nanoarchitecture with Catalytic and Photocatalytic Functions. *Chemistry - A European Journal* **2005**, *11* (10), 2997.

[56] Sato, S.; White, J. M., Photodecomposition of water over Pt/TiO₂ catalysts. *Chemical Physics Letters* **1980**, *72* (1), 83.

[57] Buso, D.; Pacifico, J.; Martucci, A.; Mulvaney, P., Gold-Nanoparticle-Doped TiO₂ Semiconductor Thin Films: Optical Characterization. *Advanced Functional Materials* **2007**, *17* (3), 347.

[58] Wu, T.-S.; Wang, K.-X.; Li, G.-D.; Sun, S.-Y.; Sun, J.; Chen, J.-S., Montmorillonite-Supported Ag/TiO₂ Nanoparticles: An Efficient Visible-Light Bacteria Photodegradation Material. *ACS Applied Materials & Interfaces* **2010**, *2* (2), 544.

[59] Banerjee, S.; Mohapatra, S. K.; Das, P. P.; Misra, M., Synthesis of Coupled Semiconductor by Filling 1D TiO₂ Nanotubes with CdS. *Chemistry of Materials* **2008**, *20* (21), 6784.

[60] Huang, L.; Peng, F.; Wang, H.; Yu, H.; Li, Z., Preparation and characterization of Cu₂O/TiO₂ nano-nano heterostructure photocatalysts. *Catalysis Communications* **2009**, *10* (14), 1839.

[61] Zhang, J.; Zhu, H.; Zheng, S.; Pan, F.; Wang, T., TiO₂ Film/Cu₂O Microgrid Heterojunction with Photocatalytic Activity under Solar Light Irradiation. *ACS Applied Materials & Interfaces* **2009**, *1* (10), 2111.

[62] Tung, W. S.; Daoud, W. A., New Approach Toward Nanosized Ferrous Ferric Oxide and Fe₃O₄-doped Titanium Dioxide Photocatalysts. *ACS Applied Materials & Interfaces* **2009**, *1* (11), 2453.

[63] Zhou, W.; Liu, H.; Wang, J.; Liu, D.; Du, G.; Cui, J., Ag₂O/TiO₂ Nanobelts

Heterostructure with Enhanced Ultraviolet and Visible Photocatalytic Activity. *ACS Applied Materials & Interfaces* **2010**, null.

[64] Yang, L.; Luo, S.; Liu, R.; Cai, Q.; Xiao, Y.; Liu, S.; Su, F.; Wen, L., Fabrication of CdSe Nanoparticles Sensitized Long TiO₂ Nanotube Arrays for Photocatalytic Degradation of Anthracene-9-carboxylic Acid under Green Monochromatic Light. *The Journal of Physical Chemistry C* **2010**, *114* (11), 4783.

[65] Huang, C.-J.; Pan, F.-M.; Tzeng, T.-C.; Li, C.; Sheu, J.-T., Growth and Field Emission of Reactive Sputtered Pd--PdO Core--Shell Nanoflakes on Platinum. *Journal of The Electrochemical Society* **2009**, *156* (2), J28.

[66] Fowler, R. H.; Nordheim, L., Electron Emission in Intense Electric Fields. *Proceedings of the Royal Society of London. Series A* **1928**, *119* (781), 173.

[67] Yu, T.; Zhu, Y. W.; Xu, X. J.; Shen, Z. X.; Chen, P.; Lim, C.-T.; Thong, J. T.-L.; Sow, C.-H., Controlled Growth and Field-Emission Properties of Cobalt Oxide Nanowalls. *Advanced Materials* **2005**, *17* (13), 1595.

[68] Smith, R. C.; Cox, D. C.; Silva, S. R. P., Electron field emission from a single carbon nanotube: Effects of anode location. *Applied Physics Letters* **2005**, *87* (10), 103112.

[69] Chen, T.-M.; Pan, F.-M.; Hung, J.-Y.; Chang, L.; Wu, S.-C.; Chen, C.-F., Amorphous Carbon Coated Silicon Nanotips Fabricated by MPCVD Using Anodic Aluminum Oxide as the Template. *Journal of The Electrochemical Society* **2007**, *154* (4), D215.

[70] Kubelka, P.; Munk, F., *Z. Tech. Phys.* **1931**, *12*, 9.

[71] Tauc, J.; Grigorovici, R.; Vancu, A., Optical Properties and Electronic Structure of Amorphous Germanium. *physica status solidi (b)* **1966**, *15* (2), 627.

[72] Nelson, J., *The Physics of Solar Cells*. 1 ed.; Imperial College Press: London, 2003.

- [73] Mor, G. K.; Varghese, O. K.; Paulose, M.; Shankar, K.; Grimes, C. A., A review on highly ordered, vertically oriented TiO₂ nanotube arrays: Fabrication, material properties, and solar energy applications. *Solar Energy Materials and Solar Cells* **2006**, *90* (14), 2011.
- [74] Sberveglieri, G.; Coccoli, G.; Benussi, P.; Groppelli, S.; Nelli, P., Electrical studies on oxygen ionosorption at ambient pressure on SnO₂(In) thin films. *Applied Surface Science* **1989**, *40* (1-2), 169.
- [75] Gurlo, A., Interplay between O₂ and SnO₂: Oxygen Ionosorption and Spectroscopic Evidence for Adsorbed Oxygen. *ChemPhysChem* **2006**, *7* (10), 2041.
- [76] Keem, K.; Kim, H.; Kim, G.-T.; Lee, J. S.; Min, B.; Cho, K.; Sung, M.-Y.; Kim, S., Photocurrent in ZnO nanowires grown from Au electrodes. *Applied Physics Letters* **2004**, *84* (22), 4376.
- [77] Fierro, J. L. G.; De La Banda, J. F. G., Chemisorption of Probe Molecules on Metal Oxides. *Catalysis Reviews: Science and Engineering* **1986**, *28* (2), 265
- [78] Kawabe, T.; Shimomura, S.; Karasuda, T.; Tabata, K.; Suzuki, E.; Yamaguchi, Y., Photoemission study of dissociatively adsorbed methane on a pre-oxidized SnO₂ thin film. *Surface Science* **2000**, *448* (2-3), 101.
- [79] Oh, S.-H.; Hoflund, G. B., Chemical State Study of Palladium Powder and Ceria-Supported Palladium during Low-Temperature CO Oxidation. *The Journal of Physical Chemistry A* **2006**, *110* (24), 7609.
- [80] Peuckert, M., XPS study on surface and bulk palladium oxide, its thermal stability, and a comparison with other noble metal oxides. *The Journal of Physical Chemistry* **1985**, *89* (12), 2481.
- [81] Hoffmann, M. R.; Martin, S. T.; Choi, W.; Bahnemann, D. W., Environmental Applications of Semiconductor Photocatalysis. *Chemical Reviews* **1995**, *95* (1), 69.
- [82] Chen, H.; Chen, S.; Quan, X.; Yu, H.; Zhao, H.; Zhang, Y., Fabrication of

TiO₂-Pt Coaxial Nanotube Array Schottky Structures for Enhanced Photocatalytic Degradation of Phenol in Aqueous Solution. *The Journal of Physical Chemistry C* **2008**, *112* (25), 9285.

[83] Mikhailova, M. P.; Titkov, A. N., Type II heterojunctions in the GaInAsSb/GaSb system. *Semiconductor Science and Technology* **1994**, *9* (7), 1279.

[84] Yang, H. Y.; Yu, S. F.; Lau, S. P.; Zhang, X.; Sun, D. D.; Jun, G., Direct Growth of ZnO Nanocrystals onto the Surface of Porous TiO₂ Nanotube Arrays for Highly Efficient and Recyclable Photocatalysts. *Small* **2009**, *5* (20), 2260.

[85] Houas, A.; Lachheb, H.; Ksibi, M.; Elaloui, E.; Guillard, C.; Herrmann, J.-M., Photocatalytic degradation pathway of methylene blue in water. *Applied Catalysis B: Environmental* **2001**, *31* (2), 145.

[86] Gnaser, H.; Savina, M. R.; Calaway, W. F.; Tripa, C. E.; Veryovkin, I. V.; Pellin, M. J., Photocatalytic degradation of methylene blue on nanocrystalline TiO₂: Surface mass spectrometry of reaction intermediates. *International Journal of Mass Spectrometry* **2005**, *245* (1-3), 61.

[87] Hwang, Y. J.; Boukai, A.; Yang, P., High Density n-Si/n-TiO₂ Core/Shell Nanowire Arrays with Enhanced Photoactivity. *Nano Letters* **2008**, *9* (1), 410.

[88] Sato, N., *Electrochemistry at Metal and Semiconductor Electrodes*. Elsevier: Amsterdam, 1998; p 6.

[89] Pommerehne, J.; Vestweber, H.; Guss, W.; Mahrt, R. F.; Bäessler, H.; Porsch, M.; Daub, J., Efficient two layer leds on a polymer blend basis. *Advanced Materials* **1995**, *7* (6), 551.

[90] Liu, Y.; Liu, M. S.; Li, X.-c.; Jen, A. K. Y., Synthesis and Characterization of a Novel Light-Emitting Polymer Containing Highly Efficient Hole-Transporting Aromatic Diamine. *Chemistry of Materials* **1998**, *10* (11), 3301.

[91] Gratzel, M., Photoelectrochemical cells. *Nature* **2001**, *414* (6861), 338.